BIOMEDICINE

Bioresorbable shape-adaptive structures for ultrasonic monitoring of deep-tissue homeostasis

Jiaqi Liu[1]†, Naijia Liu[1]†, Yameng Xu[2,3]†, Mingzheng Wu[1]†, Haohui Zhang[4]†, Yue Wang[1,5], Ying Yan[3], Angela Hill[6], Ruihao Song[1,7], Zijie Xu[1,8], Minsu Park[9], Yunyun Wu[1], Joanna L. Ciatti[1,8], Jianyu Gu[1], Haiwen Luan[1], Yamin Zhang[1], Tianyu Yang[1], Hak-Young Ahn[1], Shupeng Li[10], Wilson Z. Ray[3], Colin K. Franz[11,12,13], Matthew R. MacEwan[3], Yonggang Huang[1,4,8,10], Chet W. Hammill[6]*, Heling Wang[14,15]*, John A. Rogers[1,5,8,10,16]*

Monitoring homeostasis is an essential aspect of obtaining pathophysiological insights for treating patients. Accurate, timely assessments of homeostatic dysregulation in deep tissues typically require expensive imaging techniques or invasive biopsies. We introduce a bioresorbable shape-adaptive materials structure that enables real-time monitoring of deep-tissue homeostasis using conventional ultrasound instruments. Collections of small bioresorbable metal disks distributed within thin, pH-responsive hydrogels, deployed by surgical implantation or syringe injection, allow ultrasound-based measurements of spatiotemporal changes in pH for early assessments of anastomotic leaks after gastrointestinal surgeries, and their bioresorption after a recovery period eliminates the need for surgical extraction. Demonstrations in small and large animal models illustrate capabilities in monitoring leakage from the small intestine, the stomach, and the pancreas.

Disruption of homeostasis represents a core feature of disease pathogenesis. Monitoring homeostasis at relevant anatomical sites thus provides essential physiological and pathological information crucial to early diagnosis before the onset of externally observable symptoms. Recent work has demonstrated the potential for use of bioelectronic devices in continuous, noninvasive detection of changes in parameters related to homeostasis, including blood pressure and flow (*1*, *2*), temperature (*1*), extracellular fluid pH (*3*), blood glucose (*4*, *5*), tissue oximetry (*6*), and cerebral interstitial fluid (*7*). Measurement modalities rely on optical (*7*–*10*), thermal (*11*–*13*), or radiofrequency (*2*, *14*–*16*) signals of physiological processes. Attenuation in biological tissues limits the use of these mechanisms to shallow depths, sometimes up to the centimeter scale (*17*–*22*), which is insufficient for assessments of deep tissues. Approaches to monitoring homeostasis in deep tissues such as computed tomography (CT), x-ray imaging, or biopsies are often costly, invasive, and incompatible with continuous detection. In this context, advanced ultrasound imaging methods are of growing interest given their ease of use, wide availability, absence of radiation exposure, and capacity to probe to substantial depths (10 cm or more) (*23*) at high spatial resolution (a few hundred micrometers) (*24*). Recent advances in functional ultrasound imaging indicate possibilities for monitoring physiological (*25*, *26*) and microbiological dynamics (*27*, *28*) in complex environments.

Materials and structural designs

Millimeter-scale bioresorbable materials structures introduced here enable real-time spatiotemporal measurements of perturbations of chemical or physical homeostatic parameters in shallow or deep tissue locations by conventional ultrasound imaging, offering specific clinically relevant uses in temporary patient monitoring (see supplementary text in the supplementary materials for a detailed discussion about monitoring homeostatic dysregulation). These bioresorbable, thin, and flexible implants incorporate symmetrically distributed collections of structures that generate strong contrast in ultrasound images embedded in a soft, shape-adaptive matrix material (Fig. 1A), referred to hereafter as a bioresorbable, shape-adaptive, ultrasound-readable materials structure (BioSUM). A circular ring feature serves as an anchor for suturing the device to adjacent tissues. The matrix (Fig. 1A, green color) undergoes well-defined dimensional changes upon interactions with the surrounding biofluid environment by amounts that depend on a local parameter of interest. These transformations change the spacings between the ultrasonic indicators by magnitudes that can be quantitatively determined by imaging. The indicators consist of small disks of bioresorbable metals (e.g., Mg, Zn, Fe, W, or Mo) selected to maximize the acoustic impedance mismatch with the surroundings to ensure strong contrast in ultrasound images. The envisioned clinical use case is in postsurgical monitoring of patient status throughout a recovery period, after which resorption into the body by means of hydrolysis and natural metabolic reactions naturally eliminates the device, thereby bypassing the need for surgical extraction procedures (Fig. 1, B to D).

Homeostatic pH regulation is crucial for maintaining proper cellular and physiological functions. Perturbations may result from endogenous metabolic crises (e.g., acidosis or alkalosis) or exogenous events (e.g., surgical interventions or trauma). For example, leakage of gastrointestinal (GI) fluids secondary to anastomosis surgeries may cause considerable alterations in local pH homeostasis, with the potential to propagate throughout the peritoneal cavity, leading to organ dysfunctions and failures (*29*). Accurate monitoring of the pH in tissues surrounding the anastomotic site thus offers an opportunity for early detection of leakage with high sensitivity and specificity, to allow for therapeutic interventions that can reduce the morbidity and mortality of postoperative complications in GI surgeries [which range from 5 to 25%, depending on the sites of anastomosis (*29*)]. The absence of standard clinical approaches for assessments and the vague nature of patient symptoms in many cases pose additional challenges to early and accurate detection of anastomotic leakage (see supplementary text for details about the severity of these complications). In our proposed scheme, suturing one or more BioSUMs near the location of the anastomosis as the final step of the surgical procedure provides the basis for frequent monitoring through ultrasound imaging during a recovery period (see supplementary text and fig. S1 for an alternative approach to fixation that uses bioresorbable adhesives). The small dimensions of the devices, their thin geometries, and their soft, flexible mechanical properties provide an additional deployment option by way of syringe injection (Fig. 1E, fig. S2, and movie S1) to facilitate implantation

[1]Querrey Simpson Institute for Bioelectronics, Northwestern University, Evanston, IL 60208, USA. [2]The Institute of Materials Science and Engineering, Washington University in St. Louis, St. Louis, MO 63130, USA. [3]Department of Neurosurgery, Washington University School of Medicine, St. Louis, MO 63110, USA. [4]Department of Civil and Environmental Engineering, Northwestern University, Evanston, IL 60208, USA. [5]Department of Biomedical Engineering, Northwestern University, Evanston, IL 60208, USA. [6]Department of Surgery, Washington University School of Medicine, St. Louis, MO 63110, USA. [7]Department of Chemical and Biological Engineering, Northwestern University, Evanston, IL 60208, USA. [8]Department of Materials Science and Engineering, Northwestern University, Evanston, IL 60208, USA. [9]Department of Polymer Science and Engineering, Dankook University, Yongin 16890, Republic of Korea. [10]Department of Mechanical Engineering, Northwestern University, Evanston, IL 60208, USA. [11]Regenerative Neurorehabilitation Laboratory, Shirley Ryan AbilityLab, Chicago, IL 60611, USA. [12]Department of Physical Medicine and Rehabilitation, Feinberg School of Medicine, Northwestern University, Chicago, IL 60611, USA. [13]The Ken and Ruth Davee Department of Neurology, Feinberg School of Medicine, Northwestern University, Chicago, IL 60611, USA. [14]Laboratory of Flexible Electronics Technology, Tsinghua University, Beijing 100084, China. [15]Institute of Flexible Electronics Technology of THU Zhejiang, Jiaxing 314000, China. [16]Department of Neurological Surgery, Feinberg School of Medicine, Northwestern University, Chicago, IL 60611, USA.
*Corresponding author. Email: hammill@gmail.com (C.W.H.); wanghl2006@tsinghua.edu.cn (H.W.); jrogers@northwestern.edu (J.A.R.)
†These authors contributed equally to this work.

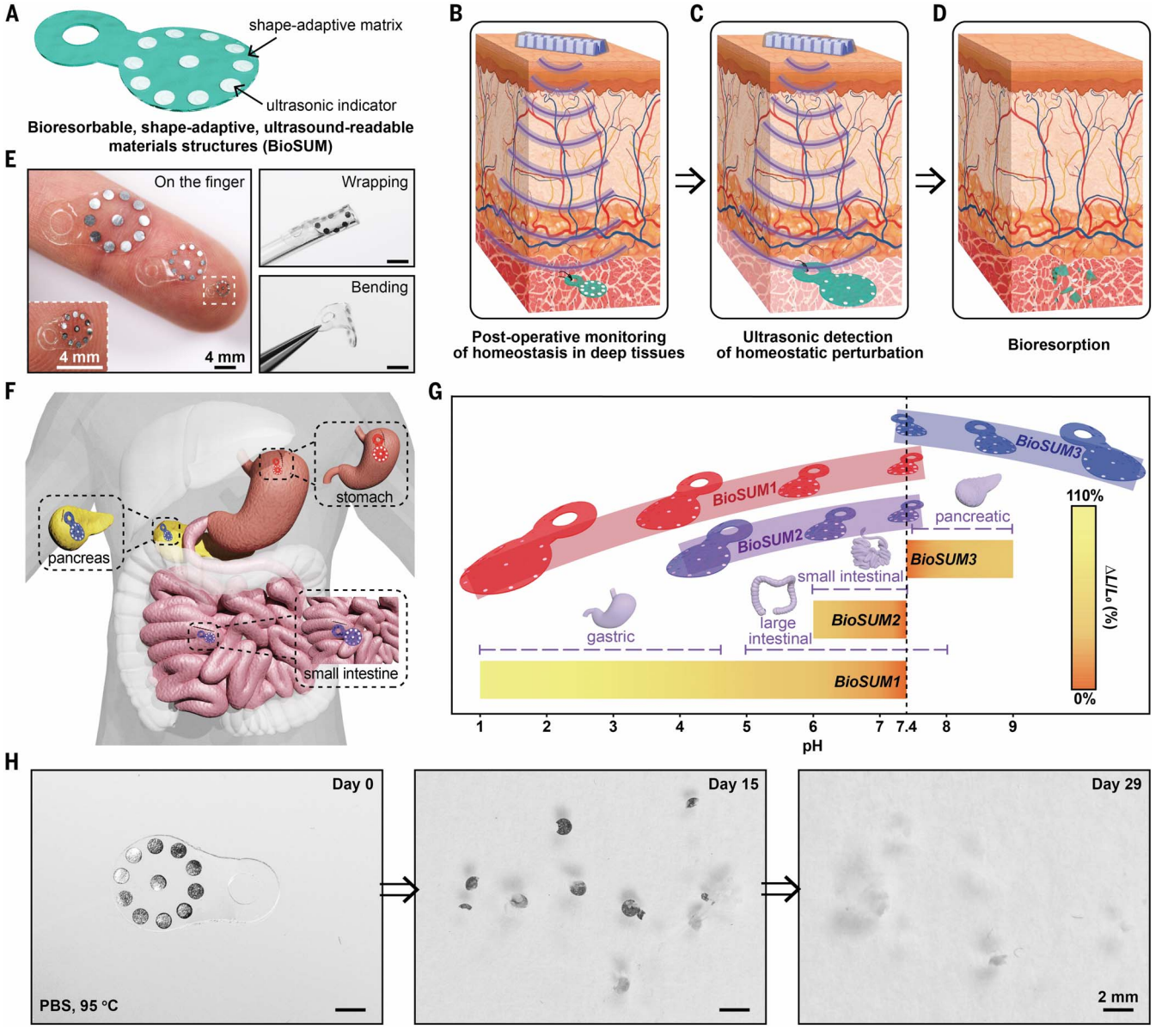

Fig. 1. Bioresorbable shape-adaptive ultrasound-readable materials structures (BioSUMs) for real-time monitoring of homeostasis in deep tissues. (**A**) Schematic illustration of our device, which includes a sparse collection of metal disks embedded in a thin hydrogel. (**B**) The BioSUM enables ultrasonic monitoring of homeostasis in deep tissues. (**C**) Ultrasonic signals from a BioSUM indicate homeostatic perturbations. (**D**) Subsequent bioresorption of the BioSUM eliminates the need for surgical extraction. (**E**) Miniaturized designs allow for implantation by laparoscopic surgery. Images of three BioSUMs of different dimensions (12, 7, and 3 mm in diameter) on the finger (left), wrapped around a plastic tube with an outer diameter of 3.175 mm (top right), and in a bent state (bottom right). (**F**) Schematic illustration of a BioSUM for detecting postsurgical leakage from the stomach, small intestine, and pancreas. (**G**) pH-responsive ranges for BioSUM1, BioSUM2, and BioSUM3, and the corresponding pH values of representative digestive juices. (**H**) Images of the accelerated dissolution of a BioSUM2 in PBS (pH 7.4) solution at 95°C.

during laparoscopic surgeries (movie S2). Their bioresorbable construction eliminates the need for surgical extraction subsequent to a desired timeframe for operation. The examples presented here illustrate capabilities in monitoring gastric, small intestinal, and pancreatic leakage as three representative cases (Fig. 1F).

These illustrations rely on hydrogels as pH-responsive matrix materials, tailored to operate across relevant ranges of pH values. Specifically, the gastric environment can present pH values as low as 1.0, thereby requiring hydrogels that swell in these acidic conditions while offering stable chemical and mechanical properties in these aggressive environments (BioSUM1). Monitoring for small intestinal leaks, by contrast, relies on hydrogels that operate at values of pH (~6.8) that are only slightly lower than normal physiological levels (~7.4) (BioSUM2). The pancreas presents alkaline conditions, thus requiring hydrogels that are responsive to pH values larger than 7.4 (BioSUM3). Figure 1G summarizes the relevant pH ranges for these three classes of hydrogels and their corresponding organ interfaces. Each is also designed to be fully bioresorbable (Fig. 1H and figs. S3 to S7; see supplementary text for the detailed mechanism). Choosing bioresorbable metals (*30*) and hydrogel materials (*31*–*34*) that undergo dissolution reactions and hydrolytic chain scissions in biofluids leads to

conversion into benign products over well-defined timescales. Figure 1H illustrates the accelerated dissolution pathway of BioSUM2 in phosphate-buffered saline (PBS; pH 7.4) at 95°C. The device largely dissolves within 15 days, and the residual materials disappear entirely after 29 days. At body temperature, the latter timescale corresponds to 174, 160, and 241 days for BioSUM1, BioSUM2, and BioSUM3, respectively.

pH-responsive behavior

The pH responses of the hydrogels originate from their chemical compositions. Materials for gastric and small intestinal leaks involve poly [2-(dimethylamino)ethyl methacrylate-co-2-(diisopropylamino)ethyl methacrylate] [p(DMAEMA-DPAEMA)] with polyethylene glycol diacrylate (PEGDA; number-average molecular weight M_n = 250) as a cross-linker (*34*, *35*) (Fig. 2, A and B). DMAEMA and DPAEMA contain tertiary amine moieties that undergo protonation and subsequent changes in osmotic pressure as the pH decreases. The hydrogel chemistry that responds in alkaline conditions relies on poly (acrylic acid–butyl acrylate) [p(AAc-BA)] with PEGDA as a cross-linker (Fig. 2, A and C). Elevation of pH results in protonation of the carboxyl moieties in AAc and a corresponding conformational change of the hydrogel network due to hydrophilicity. Specifically, the addition of hydrophobic BA hinders the protonation of carboxyl groups around the original pK_a (where K_a is the acid dissociation constant) of the AAc moiety (~4.25) and shifts the swelling transition to values larger than the physiological pH of 7.4 (*36*) (see supplementary text, figs. S8 to S11, and tables S2 to S5 for details about materials designs). Finite element analysis (FEA) that includes the effects of coupled diffusion and deformation (*37*, *38*) can capture the swelling kinetics in these polyelectrolyte hydrogels. Protonation of pH-responsive moieties enables the diffusion of buffer solutions into the cross-linked networks and successive expansion of elastomeric chains. The diffusivity (in the range of 10^{-8} to 10^{-12} m^2/s) (*37*, *38*) and the thicknesses of the hydrogels largely determine the swelling kinetics. The swelling ratio correlates to the inverse square of thickness, $\sim\tau/h^2$, where τ is time and h is thickness. Physical entanglement and grafted side chains in the hydrogel networks contribute to considerable swelling ratios at the equilibrium state (see supplementary text, figs. S12 to S14, and table S1 for more details about the swelling of hydrogels). FEA results predict the thickness-dependent swelling behavior of BioSUM1 for 10 min at different pH values, in terms of the percentage change in length ($\Delta L/L_0$%) (fig. S15). To balance the need for both fast response time and small dimensions, the circular parts of the devices reported here have thicknesses of 300 μm and diameters of 7 mm, with a symmetrically distributed collection of thin, circular disks of Zn (1 mm diameter and 25 μm thickness) located at the midpoint of the thickness of the hydrogel (fig. S16A). The disks induce no measurable mechanical constraints on the swelling of the hydrogel matrix (fig. S17). Further miniaturized devices (4 mm diameter and 200 μm thickness), with expected enhancements in response times (figs. S16B and S18) facilitate use in small animal models.

Figure 2, D and E, presents experimental measurements and FEA results for the time-resolved swelling behavior of BioSUM1 in a citrate buffer solution at pH 4.5. Increasing the molar ratio of DPAEMA improves the mechanical robustness to ensure stable behavior in strongly acidic gastric fluids (figs. S9 and S19 to S21 and tables S2 to S4). This increase also, however, reduces the degree of swelling near physiological pH. Experimental measurements along with FEA modeling of the swelling ratios ($\Delta L/L_0$%) for BioSUM1 and BioSUM2 are presented in Fig. 2, F to K. For example, BioSUM1 swells by 65% in pH 4.0 citrate buffer solution within 30 min, and BioSUM2 swells by 12% in pH 7.2 in the same timeframe. When in direct contact with simulated gastric fluid (SGF; pH ~1.2), BioSUM1 swells by 10% in less than 1 min and reaches >35% in 30 min (Fig. 2H). BioSUM2 can respond to 1 ml of simulated intestinal fluid (SIF; pH ~6.8) applied directly onto the device by swelling >10% within 10 min and >15% in 30 min (Fig. 2K). Figure 2, L and M, presents the response of BioSUM3 to alkaline conditions. BioSUM3 swells by 35% in pH 9 within 30 min (Fig. 2L), to an equilibrium swelling ratio of ~40% (Fig. 2M). BioSUM3 swells by 10% within 1 min after contact with 1 ml of simulated pancreatic juice (SPJ; pH ~8.2), and it reaches 30% in 30 min (Fig. 2N). FEA modeling accurately predicts the swelling kinetics for all cases (Fig. 2, F, I, and L).

Multiple devices at strategic anatomical locations relative to a surgical site provided the basis for spatiotemporal monitoring of the convective spread of SGF (Fig. 2, O and P, and figs. S22 and S23). Benchtop demonstrations involved the introduction of SGF on one end of a slab of agarose gel. Seven sensors distributed along a straight line in a thin layer of PBS solution on this gel allowed measurements of the swelling ratios at corresponding locations, to a distance of 30 cm from the origin at a spacing of 5 cm. Figure 2P shows the time-resolved responses of BioSUM1 at different locations, indicating expected performance and a spatial resolution comparable to the sizes and spacings of the devices.

Sensing by ultrasound imaging in deep tissues

Ultrasound B-mode imaging serves as a mechanism for quantitatively evaluating the pH-dependent geometry of these responsive hydrogels when implanted at deep tissue locations. The disks of Zn, an established bioresorbable metal that reacts with water to yield the benign end product $Zn(OH)_2$ (*30*), act as ultrasonic indicators. The acoustic impedance mismatch between these Zn structures and the surrounding hydrogel matrix and adjacent soft tissues enhances their visibility in B-mode images. The reflection coefficient is approximately proportional to $(Z_1 - Z_2)^2/(Z_1 + Z_2)^2$ for structure thickness greater than ~20 μm for normal incidence specular reflections (*39*), where Z_1 and Z_2 are the impedances for the Zn and the hydrogel, respectively (see supplementary text and figs. S11 and S24 for details about reflections for thicknesses of <20 μm). For the systems reported here, the reflection coefficients at the interface between the Zn structures and the hydrogel are >80%. By contrast, coefficients between typical surrounding soft tissues and the hydrogel are <0.5%. The symmetric, circular distribution of these disks (Fig. 3, A to C) allows ultrasonic visualization in a manner that is independent of the orientation. During an ultrasound scan, acoustic waves generated by the transducer penetrate through tissues and reflect from these disks to form a cross-sectional image of their spacings. For the specific geometry presented here, the array of disks appears as three equally distributed bright segments in the image, clearly differentiated from background features associated with tissue structures. The distance between these hyperechoic components may shift in ultrasound images, depending on the specific cross-sectional position and orientation of the acoustic waves with respect to the device (Fig. 3A). The cross-sectional position across the diameter of the device represents the largest separation distance between bright segments in B-mode imaging, which defines the actual changes in dimension. An example of this process conducted in a rat model with a device on the surface of the stomach is shown in Fig. 3D. The left image denotes signals of BioSUM on the perimeter, and the right image shows signals from three disks along the diameter.

The symmetric design of the disks and the mechanically flexible nature of the BioSUM enable detection in nonplanar configurations (figs. S25 to S27). For example, when the BioSUM is not parallel to the transducer, it appears tilted in the B-mode image yet still reflects signals from the three disks along the diameter (Fig. 3C). The natural curvature of the targeted organs may lead to such tilted orientations (Fig. 3E) but without an effect on the measured distances between the disks, as in the right image of Fig. 3D. For additional details, see the supplementary text and figs. S28 and S29.

The signal-to-noise ratio (SNR) and the lateral resolution in B-mode images quantify the signal quality, yet both properties diminish with depth owing to the attenuation of ultrasonic waves as they propagate through the tissues. The lateral resolution (in terms of absolute length) is proportional to $\lambda F/L$ (*40*), where λ is the ultrasound wavelength, F is the focal depth, and

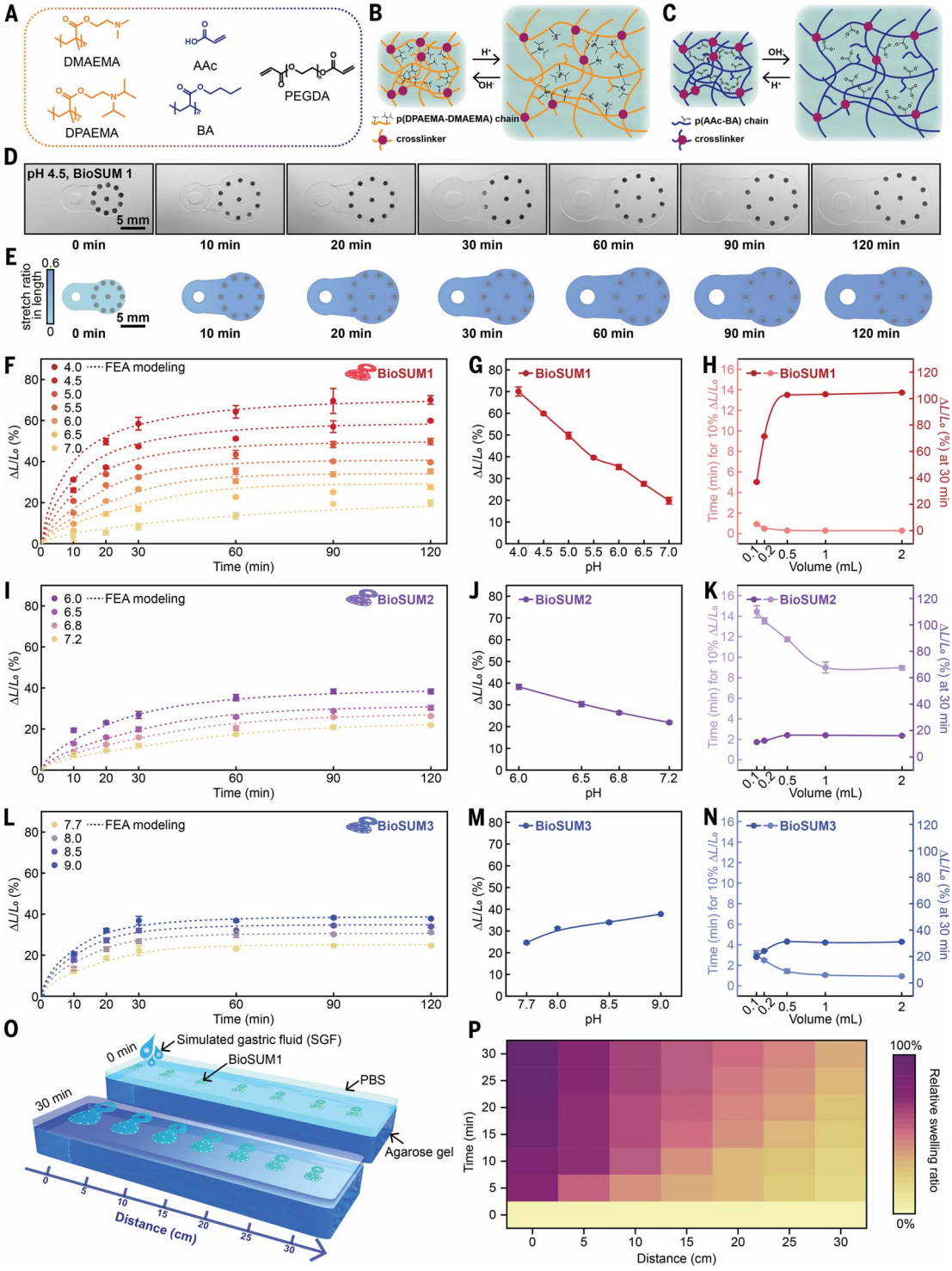

Fig. 2. pH-responsive behaviors of shape-adaptive materials structures. (**A**) Chemical structures of the monomers, oligomers, and cross-linker in the pH-responsive hydrogels used in the BioSUM system. (**B**) Schematic illustration of the mechanism for pH-responsive hydrogels in BioSUM1 and BioSUM2. (**C**) Schematic illustration of the mechanism for the pH-responsive hydrogel in BioSUM3. (**D**) Time-dependent response of a BioSUM1 when immersed in a solution with pH 4.5. (**E**) FEA modeling results of the case shown in (D). (**F**, **I**, and **L**) Ultrasonic measurement of time-dependent responses of BioSUM1, BioSUM2, and BioSUM3, respectively, to immersion in solutions with different pH values. $\Delta L/L_0$ (%) denotes the swelling ratio. (**G**, **J**, and **M**) Response of BioSUM1, BioSUM2, and BioSUM3, respectively, to immersion in solutions with different pH values at the equilibrium state. (**H**, **K**, and **N**) Optical measurement of sensitivity of a BioSUM to the introduction of different amounts of simulated GI fluids, including the response time for reaching 10% $\Delta L/L_0$ and $\Delta L/L_0$% at 30 min. (H) Response of a BioSUM1 to simulated gastric fluid. (K) Response of a BioSUM2 to simulated small intestinal fluid. (N) Response of a BioSUM3 to simulated pancreatic juice. (**O**) Schematic illustration of the setup for spatiotemporal mapping of pH with BioSUM1s. (**P**) Spatiotemporal characteristics, determined through optical methods, of BioSUM1s in response to the introduction of simulated gastric fluid at one end of the system. BioSUMs are fully swollen in PBS (pH 7.4) for 24 hours before the measurements presented here. Error bars in (F) to (N) represent ±SD.

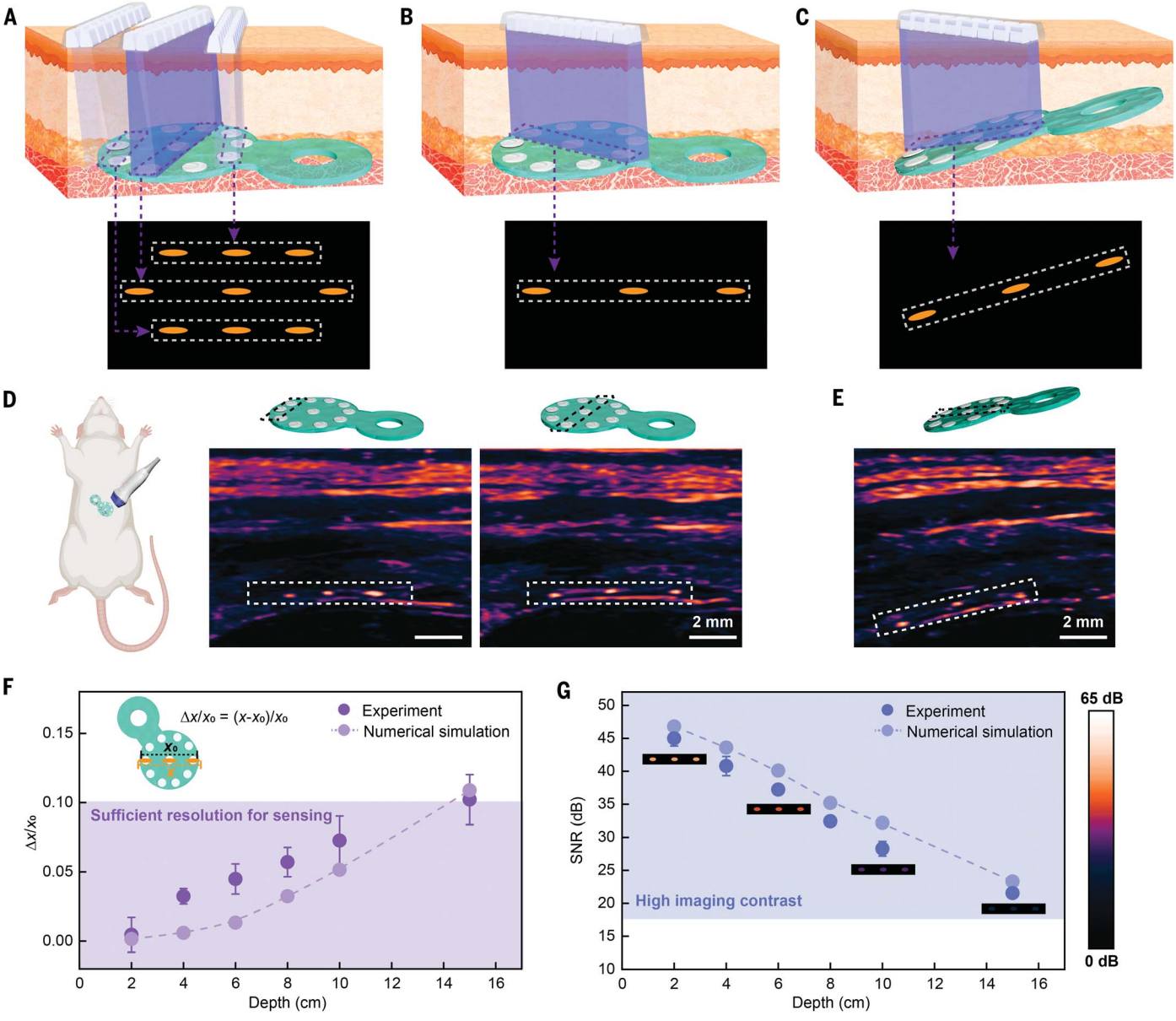

Fig. 3. Sensing by ultrasound imaging in deep tissues. (**A**) Schematic illustration of the cross-sectional position of acoustic waves relative to a BioSUM in different cases, and the corresponding signals in the ultrasound B-mode image. (**B**) The symmetric design enables ultrasonic visualization independent of the orientation of the transducer. (**C**) Schematic illustration of a BioSUM in a tilted case, and the corresponding signals in the ultrasound B-mode image. (**D**) Ultrasound B-mode images of a BioSUM on the stomach in a rat model demonstrating the cross-sectional position of acoustic waves in different cases, correlated to the schematic illustration in (A). (**E**) Ultrasound B-mode image of a BioSUM in a tilted case on the stomach in a rat model, corresponding to the schematic illustration in (C). (**F**) Experimental and numerical simulation results for the measurement accuracy of a BioSUM at different depths. $\Delta x/x_0$ is the deviation of measured length divided by the actual length. (**G**) Experimental and numerical simulation results for the signal-to-noise ratio at different depths. Inset images are schematic illustrations of the image contrast in decibels. Error bars in (F) and (G) represent ±SD.

L is the aperture length. With a fixed transducer (i.e., fixed aperture length) and scanning frequency (i.e., ultrasound wavelength), the resolution decreases with depth. Scattering from heterogeneous tissues causes attenuation that deteriorates the SNR as the depth increases. Experimental and numerical investigations (Fig. 3, F and G, and figs. S11 and S30 to S34) quantify the depth dependence of the signal quality using ultrasonic waves with frequencies of 5 MHz. The experimental and numerical simulation results show similar trends over depth. The slightly lower signal quality from experiments may be attributed to effects of inhomogeneities in the soft tissues. The deviation of the measured separation between Zn disks divided by the actual separation, $\Delta x/x_0$, serves as a relevant metric. Numerical simulation and experimental results for images captured underneath a pork phantom in Fig. 3F show that $\Delta x/x_0$ increases with depth but remains <0.1 for depths up to 15 cm. This result indicates that dimensional changes of 10% or more can be accurately detected at depths of 15 cm, consistent with the swelling behaviors of the devices reported here. For SNR defined as the average contrast of three bright segments relative to the background, the results indicate that the SNR remains >18 dB for depths of up to 15 cm (Fig. 3G), which is necessary for clear visualization

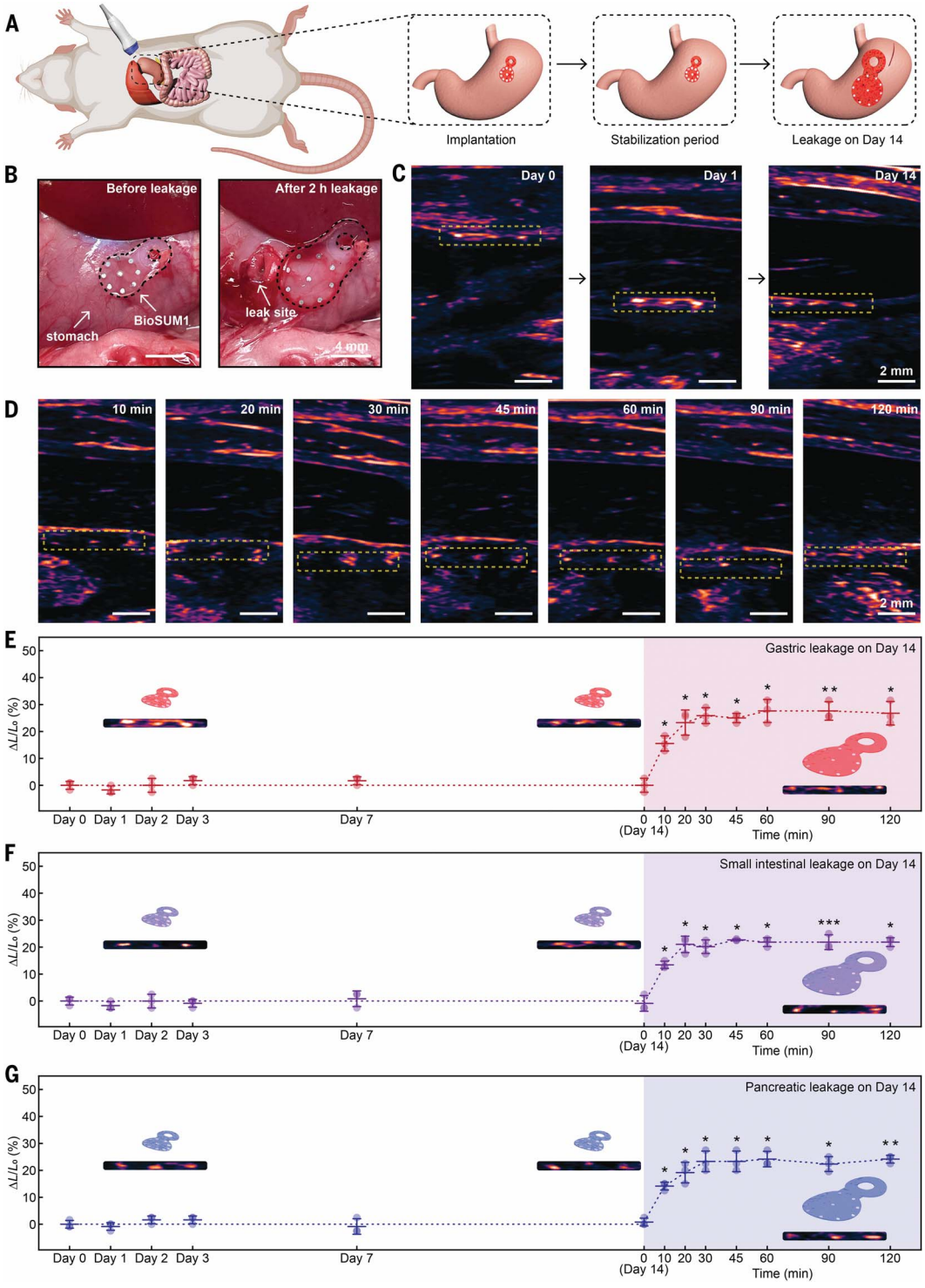

Fig. 4. Longitudinal monitoring of pH homeostasis of the rat gastrointestinal system. (**A**) Schematic illustration of the implantation and sensing procedure for a BioSUM1 on the stomach of a rat. [Created with Biorender.com] (**B**) Images showing the expansion of a BioSUM1 2 hours after creating a single gastrotomy. (**C**) Ultrasound images of a BioSUM1 on the stomach over a 14-day stabilization period without induced gastric leakage. The depth of the array of Zn disks changes between day 0 and day 1 because of postoperative relocation of organs. (**D**) Longitudinal ultrasound images of BioSUM1 on the stomach after acute gastrotomy. (**E**) Summary data showing the swelling ratios of a BioSUM1 during the stabilization period and after acute gastrotomy. $n = 3$ biologically independent animals. Repeated measures (RM) one-way analysis of variance (ANOVA), $P = 0.0008$, Holm-Sidak's multiple comparison test versus day 14 (0 min): 10 min, $P = 0.0208$; 20 min, $P = 0.0208$; 30 min, $P = 0.0198$; 45 min, $P = 0.0207$; 60 min, $P = 0.0208$; 90 min, $P = 0.0092$; and 120 min, $P = 0.0207$. Inset ultrasound images representing day 1, day 14, and 120 min were extracted from (C) and (D). (**F**) Same as (E), but for a BioSUM2 and enterotomy. RM one-way ANOVA, $P = 0.0009$, Holm-Sidak's multiple comparison test versus day 14 (0 min): 10 min, $P = 0.0254$; 20 min, $P = 0.0254$; 30 min, $P = 0.0141$; 45 min, $P = 0.0254$; 60 min, $P = 0.0254$; 90 min, $P = 0.0005$; and 120 min, $P = 0.0254$. Inset ultrasound images representing day 1, day 14, and 120 min were extracted from fig. S43. (**G**) Same as (E), but for a BioSUM3 and pancreatic leakage. RM one-way ANOVA, $P = 0.0021$, Holm-Sidak's multiple comparison test versus day 14 (0 min): 10 min, $P = 0.0231$; 20 min, $P = 0.0359$; 30 min, $P = 0.0359$; 45 min, $P = 0.0359$; 60 min, $P = 0.0348$; 90 min, $P = 0.0325$; and 120 min, $P = 0.0089$. Dots represent individual animals. Line represents B-spline. Error bars represent ±SD. $^*P < 0.05$, $^{**}P < 0.01$, $^{***}P < 0.001$. Inset ultrasound images representing day 1, day 14, and 120 min were extracted from fig. S44. BioSUMs were fully swollen in PBS (pH 7.4) for 24 hours before implantation, in all cases.

in medical imaging (*23*). The SNR and $\Delta x/x_0$ deteriorate as the diameter of the Zn disks decreases (figs. S11 and S30), as a limiting consideration in miniaturizing these structures. Simulation results indicate that to achieve $\Delta x/x_0 \sim 0.1$ and SNR ~ 18 dB, the hydrogel and disks must have diameters of 3 and 0.5 mm, respectively (fig. S35).

Monitoring pH homeostasis in animal models

Longitudinal measurements using rat models validate the feasibility of ultrasonic detection of GI leakage in a manner that is compatible with various ultrasound imaging systems (figs. S36 and S37). Our studies involved imaging after implantation on the stomach and for a subsequent 14 days to confirm the geometric and operational stability in this physiological

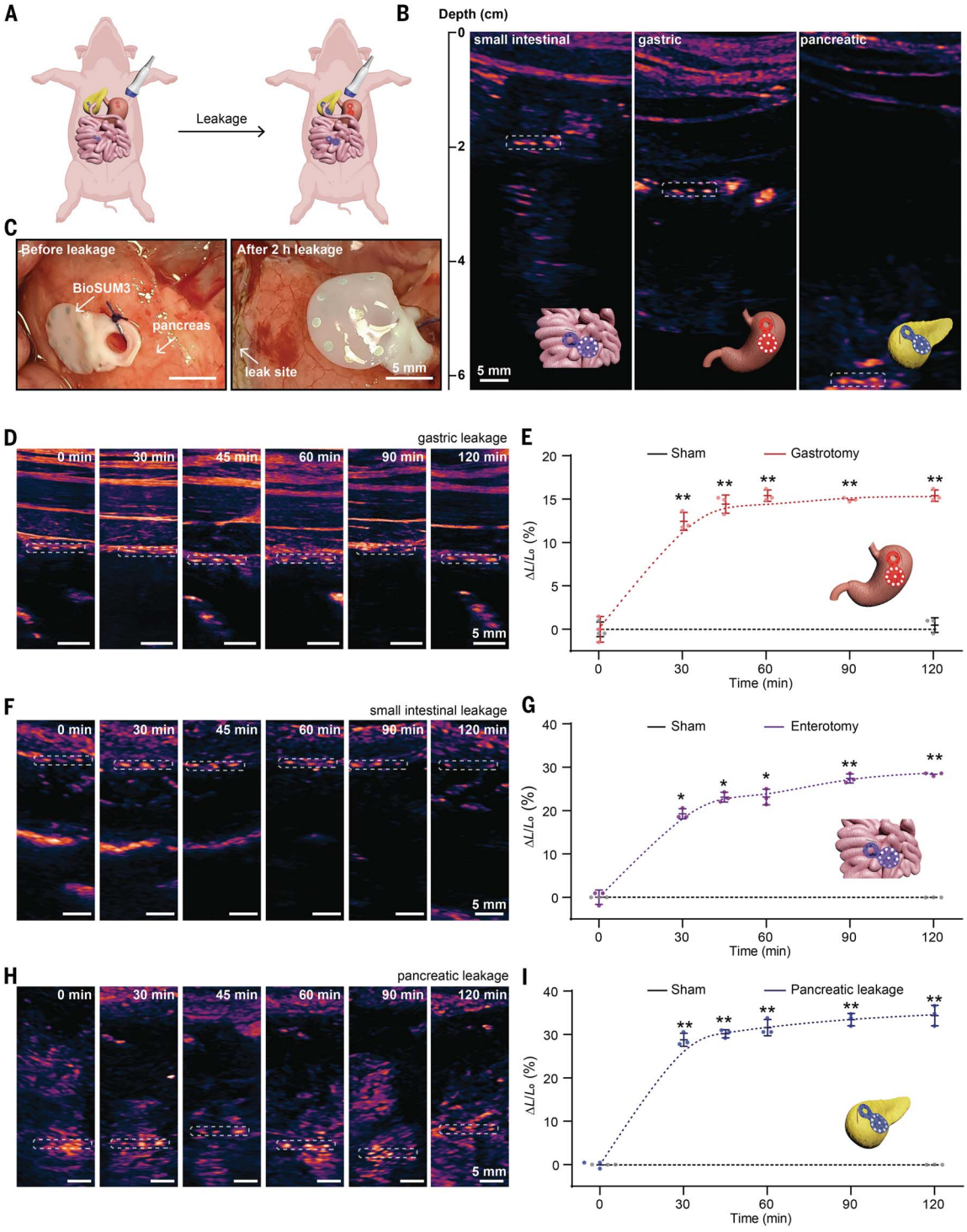

Fig. 5. Deep-tissue detection of gastrointestinal leaks in porcine models. (**A**) Schematic illustration of the experimental procedures. [Created with Biorender.com] (**B**) Ultrasound images of BioSUMs on the small intestine (left, BioSUM2), stomach (middle, BioSUM1), and pancreas (right, BioSUM3) in a pig. (**C**) Images showing the expansion of a BioSUM3 after pancreatic leakage. (**D**) Longitudinal ultrasound images of a BioSUM1 after acute gastrotomy. (**E**) Summary data showing the swelling ratio of a BioSUM1 with or without acute gastrotomy. $n = 3$ independent samples per group. Two-way ANOVA, Holm-Sidak's multiple comparison with gastrotomy $T = 0$ min: gastrotomy, 30 min, $P = 0.0055$; 45 min, $P = 0.0024$; 60 min, $P = 0.0015$; 90 min, $P = 0.0019$; and 120 min, $P = 0.0024$; sham, 30 min, $P = 0.8568$. (**F**) Same as (D), but for a BioSUM2 and enterotomy. (**G**) Same as (E), but for a BioSUM2 and enterotomy. $n = 3$ independent samples per group. Two-way ANOVA, Holm-Sidak's multiple comparison with enterotomy $T = 0$ min: enterotomy, 30 min, $P = 0.0351$; 45 min, $P = 0.0120$; 60 min, $P = 0.0120$; 90 min, $P = 0.0028$; and 120 min, $P = 0.0049$; sham, 30 min, $P = 0.9970$. (**H**) Same as (D), but for a BioSUM3 and pancreatic leakage. Dots represent individual samples. Line represents B-spline. Error bars represent ±SD. $^{*}P < 0.05$, $^{**}P < 0.01$. (**I**) Same as (E), but for a BioSUM3 and pancreatic leakage. $n = 3$ independent samples per group. Two-way ANOVA, Holm-Sidak's multiple comparison with pancreatic leakage $T = 0$ min: pancreatic leakage, 30 min, $P = 0.0045$; 45 min, $P = 0.0045$; 60 min, $P = 0.0045$; 90 min, $P = 0.0026$; and 120 min, $P = 0.0045$; sham, 30 min, $P = 0.9988$. BioSUMs were fully swollen in PBS (pH 7.4) for 24 hours before all the implantation procedures.

environment. Creating a 3-mm gastrotomy (incision in the stomach) on day 14 led to leakage, monitored immediately after closing the surgical site by imaging for a subsequent 2 hours (Fig. 4A and fig. S38). Visual inspection afterward confirmed the geometric changes (Fig. 4B). The results suggested minimal fluctuations in dimensions on postoperative days 1 through 14 (see supplementary text and fig. S39 for discussion on mechanical deformations), consistent with an absence of movement of the device and with a local pH stably maintained by homeostatic regulation (Fig. 4C and fig. S40). After the creation of a gastrotomy on postoperative day 14, the BioSUM1 expanded gradually during the 2-hour period, as evidenced by the increased distance between the Zn disks in B-mode images (Fig. 4D). The swelling was evident 10 min after the gastrotomy (Fig. 4E and fig. S41), even for the modest volume (<1 ml) of gastric fluid released in these experiments (*41*). In addition, the expanded dimensions of the device after swelling remained stable after 2 hours. Further in vivo experiments confirmed this behavior for at least 6 hours after leakage terminated (fig. S42). Specifically, 2 hours after leakage ceased and the surgical site was closed, the rats moved freely for 6 hours. Ultrasonic evaluation after this period indicated that the dimensions were unchanged. In clinical practice, this behavior may prevent false-negative readouts that could otherwise arise as a result of delayed examinations. Similar procedures validated capabilities for ultrasound imaging of changes in pH associated with small intestinal and pancreatic leaks using the alternative hydrogel chemistries described previously (Fig. 4, F and G, and figs. S43 to S47). Real-time, dynamic changes in the pH of the local environment associated with leaks in the rat model obtained from benchtop studies of swelling behaviors are illustrated in fig. S48.

Tests on porcine models confirmed operation at scales comparable to the adult human GI tract (Fig. 5A). The results in Fig. 5B successfully demonstrate ultrasonic detection of BioSUMs on GI organs, imaged transabdominally through multiple layers of tissue with heterogeneous acoustic properties. Across this range of depths, the Zn disk array appeared as a distinct feature distinguishable from the background. Inducing GI leakage adjacent to the devices enabled monitoring of changes in a subsequent 2-hour period. Visual inspection confirmed these dimensional changes 2 hours after the creation of a pancreatic leak (Fig. 5C). The first ultrasonic scan, performed 30 min after creation of the GI leak, revealed significant dimensional changes in all three types of BioSUMs. The average swelling ratio was >10% at 30 min after the creation of the leak (Fig. 5, D to I). Histological analysis showed no remarkable inflammation, fibrosis, or necrosis compared with a sham group (figs. S49 and S50). Evaluations of blood chemistry indicated results within normal ranges (fig. S51, A and B), and element analysis showed no significant accumulation of Zn in the heart, liver, spleen, lung, kidney, or blood, in comparison with the sham group (fig. S51C). In vitro cytocompatibility of BioSUMs revealed a negligible effect on cell viability and no significant cell death in close proximity to the devices (figs. S52 and S53).

Conclusions

We introduce bioresorbable shape-adaptive structures that enable rapid, noninvasive measurements of homeostasis in deep tissues by conventional ultrasound imaging techniques. The swelling of thin films of a responsive hydrogel matrix induced by homeostatic perturbations leads to changes in separations between sparse collections of bioresorbable metal elements functioning as indicators whose positions can be determined accurately by ultrasound. The large mismatch between the acoustic impedance of these elements and the surrounding materials produces high contrast in ultrasound images, thereby allowing for accurate measurements of their separations, and thus local physical or chemical characteristics of the surrounding tissues in shallow or deep locations. An envisioned clinical scenario is in real-time detection of anastomotic leakage through changes in pH during a period of recovery after a GI surgery, to allow for early intervention. The devices survive for a relevant timeframe and then naturally bioresorb, eliminating the need for secondary surgical extraction procedures. In vivo demonstrations of this concept in small and large animals validate materials designs tailored for use in gastric, small intestinal, and pancreatic leakage.

REFERENCES AND NOTES

1. K. Kwon *et al*., *Nat. Biomed. Eng.* **7**, 1215–1228 (2023).
2. C. M. Boutry *et al*., *Nat. Biomed. Eng.* **3**, 47–57 (2019).
3. M. Corsi *et al*., *Adv. Sci.* **9**, e2202062 (2022).
4. L. Lipani *et al*., *Nat. Nanotechnol.* **13**, 504–511 (2018).
5. Y. Chen *et al*., *Sci. Adv.* **3**, e1701629 (2017).
6. H. Zhang *et al*., *Sci. Adv.* **5**, eaaw0873 (2019).
7. J. Shin *et al*., *Sci. Adv.* **5**, eaaw1899 (2019).
8. L. Lu *et al*., *Proc. Natl. Acad. Sci. U.S.A.* **115**, E1374–E1383 (2018).
9. W. Bai *et al*., *Nat. Biomed. Eng.* **3**, 644–654 (2019).
10. J. Kim *et al*., *Sci. Adv.* **2**, e1600418 (2016).
11. K. Kwon *et al*., *Nat. Electron.* **4**, 302–312 (2021).
12. R. C. Webb *et al*., *Sci. Adv.* **1**, e1500701 (2015).
13. K. Kwon *et al*., *Proc. Natl. Acad. Sci. U.S.A.* **118**, e2020398118 (2021).
14. S.-W. Hwang *et al*., *Science* **337**, 1640–1644 (2012).
15. Y. S. Oh *et al*., *Nat. Commun.* **12**, 5008 (2021).
16. D. R. Agrawal *et al*., *Nat. Biomed. Eng.* **1**, 0043 (2017).
17. V. B. Koman *et al*., *Nat. Nanotechnol.* **17**, 643–652 (2022).
18. S. Iwano *et al*., *Science* **359**, 935–939 (2018).
19. S. Sonmezoglu, J. R. Fineman, E. Maltepe, M. M. Maharbiz, *Nat. Biotechnol.* **39**, 855–864 (2021).
20. S. Sharma *et al*., *Nat. Electron.* **6**, 242–256 (2023).
21. A. Hai, V. C. Spanoudaki, B. B. Bartelle, A. Jasanoff, *Nat. Biomed. Eng.* **3**, 69–78 (2019).
22. V. Kalidasan *et al*., *Nat. Biomed. Eng.* **5**, 1217–1227 (2021).
23. C. Wang *et al*., *Nat. Biomed. Eng.* **5**, 749–758 (2021).
24. D. Maresca *et al*., *Annu. Rev. Chem. Biomol. Eng.* **9**, 229–252 (2018).
25. E. Macé *et al*., *Nat. Methods* **8**, 662–664 (2011).
26. A. Dizeux *et al*., *Nat. Commun.* **10**, 1400 (2019).
27. R. W. Bourdeau *et al*., *Nature* **553**, 86–90 (2018).
28. A. Farhadi, G. H. Ho, D. P. Sawyer, R. W. Bourdeau, M. G. Shapiro, *Science* **365**, 1469–1475 (2019).
29. E. Girard *et al*., *J. Visc. Surg.* **151**, 441–450 (2014).
30. L. Yin *et al*., *Adv. Funct. Mater.* **24**, 645–658 (2014).
31. A. Lendlein, A. M. Schmidt, R. Langer, *Proc. Natl. Acad. Sci. U.S.A.* **98**, 842–847 (2001).
32. S. S. Halacheva *et al*., *Biomacromolecules* **15**, 1814–1827 (2014).
33. M. Changez, V. Koul, B. Krishna, A. K. Dinda, V. Choudhary, *Biomaterials* **25**, 139–146 (2004).
34. M. J. Bruining *et al*., *Biomaterials* **21**, 595–604 (2000).
35. N. Deirram, C. Zhang, S. S. Kermaniyan, A. P. R. Johnston, G. K. Such, *Macromol. Rapid Commun.* **40**, e1800917 (2019).
36. O. E. Philippova, D. Hourdet, R. Audebert, A. R. Khokhlov, *Macromolecules* **30**, 8278–8285 (1997).
37. H. Zhang, M. Dehghany, Y. Hu, *J. Appl. Mech.* **87**, 061010 (2020).
38. W. Hong, X. Zhao, J. Zhou, Z. Suo, *J. Mech. Phys. Solids* **56**, 1779–1793 (2008).
39. N. M. Tole, *Basic Physics of Ultrasonographic Imaging* (World Health Organization, 2005).
40. J. T. Ylitalo, H. Ermert, *IEEE Trans. Ultrason. Ferroelectr. Freq. Control* **41**, 333–339 (1994).
41. E. L. McConnell, A. W. Basit, S. Murdan, *J. Pharm. Pharmacol.* **60**, 63–70 (2008).

ACKNOWLEDGMENTS

We thank S. Li, S. Papastefan, C. Redden, and J. B. Walters for preliminary efforts in testing. We thank Y. Gao and B. Jin for helpful discussions. Histology services were provided by the Northwestern University Research Histology and Phenotyping Laboratory, which is supported by NCI P30-CA060553 awarded to the Robert H. Lurie Comprehensive Cancer Center. Metal analysis was performed at the Northwestern University Quantitative Bio-element Imaging Center. In vitro cytocompatibility was supported by the Developmental Therapeutics Core at Northwestern University and the Robert H. Lurie Comprehensive Cancer Center support grant (NCI CA060553). We thank the Veterinary Diagnostic Laboratory at the University of Illinois Urbana-Champaign for conducting blood tests. This work made use of the MatCI Facility supported by the MRSEC program of the National Science Foundation (DMR-1720139) at the Materials Research Center of Northwestern University. The schematic illustrations of the rat in Fig. 4A and the pig in Fig. 5A were created with BioRender.com. **Funding:** This work was funded by the Querrey-Simpson Institute for Bioelectronics (J.L., N.L., M.W., Y.Wa., R.S., Z.X., M.P., Y.Wu, J.L.C., J.G., H.L., Y.Z., T.Y., H.-Y.A., and J.A.R.); the NSF Graduate Research Fellowship (grant DGE-2234667) (J.L.C.); the Washington University School of Medicine Surgical Oncology Basic Science and Translational Research Training Program grant T32CA009621 from the National Cancer Institute (NCI) (A.H.); the Belle Carnell Regenerative Neurorehabilitation Fund (C.K.F.); the Leadership in Entrepreneurial Acceleration Program (LEAP) at Washington University in St. Louis, Missouri (Y.X., Y.Y., W.Z.R., and M.R.M.); the National Natural Science Foundation of China (grant 12272352) (H.W.); and the Emerson Collective Cancer Research Fund (C.W.H.). **Author contributions:** Conceptualization: J.L., N.L., C.W.H., and J.A.R. Methodology: J.L., N.L., Y.X., M.W., Y.Y., C.W.H., and J.A.R. Theoretical simulations: H.Z., S.L., Y.H., and H.W. Investigation: J.L., N.L., Y.X., M.W., Y.Y., A.H., R.S., Z.X., M.P., Y.Wu, J.L.C., J.G., H.L., Y.Z., T.Y., H.-Y.A., W.Z.R., C.K.F., M.R.M., and C.W.H. Software: Y.Wa. Data analysis: J.L., N.L., Y.X., and M.W. Visualization: J.L., N.L., Y.X., and M.W. Supervision: C.W.H., H.W., and J.A.R. Writing – original draft: J.L., N.L., Y.X., M.W., H.Z., H.W., and J.A.R. Writing – review & editing: J.L., N.L., Y.X., M.W., H.Z., Y.H., C.W.H., H.W., and J.A.R. **Competing interests:** The authors declare that they have no competing interests. **Data and materials availability:** All data are available in the manuscript or the supplementary materials.

SUPPLEMENTARY MATERIALS

science.org/doi/10.1126/science.adk9880
Materials and Methods
Supplementary Text
Figs. S1 to S53
Tables S1 to S5
References (*42*–*76*)
MDAR Reproducibility Checklist
Movies S1 and S2

Submitted 21 September 2023; accepted 12 January 2024
10.1126/science.adk9880

Science
AAAS

Supplementary Materials for

Bioresorbable shape-adaptive structures for ultrasonic monitoring of deep-tissue homeostasis

Jiaqi Liu *et al*.

Corresponding authors: Chet W. Hammill, hammill@gmail.com; Heling Wang, wanghl2006@tsinghua.edu.cn; John A. Rogers, jrogers@northwestern.edu

Science **383**, 1096 (2024)
DOI: 10.1126/science.adk9880

The PDF file includes:

Other Supplementary Material for this manuscript includes the following:

Materials and Methods

Synthesis of bioresorbable, pH-responsive hydrogels

The synthesis of BioSUM1 started with the chain extension reaction of a mixture of 2-(dimethylamino)ethyl methacrylate monomer (DMAEMA, Sigma Aldrich) and 2-(diisopropylamino)ethyl methacrylate monomer (DPAEMA, Sigma Aldrich) (DMAEMA: DPAEMA = 7:3 in weight ratio). Adding 2 wt% 2-hydroxy-2-methylpropiophenone photoinitiator (Darocur 1173, Sigma Aldrich) followed by UV irradiation (365 nm, 500 mW/cm^2) for 8 min yielded DPAEMA-DMAEMA oligomers. Subsequent addition of 3.85 wt% poly(ethylene glycol) diacrylate (PEGDA, M_n 250, Sigma Aldrich) with respect to the monomer mixture and 0.5 wt% 2,2-dimethoxy-2-phenylacetophenone photoinitiator (DMPA, Sigma Aldrich) formed a precursor to the hydrogel. UV exposure for 8 min under a nitrogen atmosphere yielded a crosslinked hydrogel network.

Synthesis of BioSUM2 started with the chain extension reaction of a mixture of DMAEMA and DPAEMA (DMAEMA: DPAEMA = 9:1 in weight ratio). Adding 2 wt% Darocur 1173 followed by UV irradiation (365 nm, 500 mW/cm^2) for 8.5 min yielded DPAEMA-DMAEMA oligomers. Subsequent addition of 2.9 wt% PEGDA M_n 250 and 0.5 wt% DMPA photoinitiator formed a precursor to the hydrogel. UV exposure for 10 min under a nitrogen atmosphere yielded a crosslinked hydrogel network.

Synthesis of BioSUM3 started with the chain extension reaction of butyl acrylate monomer (BA, Sigma Aldrich). Adding 0.5 wt% Darocur 1173 photoinitiator followed by UV irradiation (365 nm, 500 mW/cm^2) for 160 s yielded the BA oligomer. Subsequent addition of 21.8 wt% of the pH-responsive monomer acrylic acid (AAc, Sigma Aldrich), 1 wt% PEGDA M_n 250 and 0.5 wt% DMPA photoinitiator formed a precursor to the hydrogel. UV exposure for 10 min under a nitrogen atmosphere yielded a crosslinked hydrogel network.

Fabrication of bioresorbable, shape-adaptive ultrasound-readable materials structures (BioSUMs)

Fabrication of BioSUMs for the porcine model began with blade coating of hydrogel precursor and partial curing into a 150 μm thick film (100 μm thick for the rat model) by UV exposure under a nitrogen atmosphere on a glass slide treated with 0.2 vol% trichloro(octadecyl)silane (Sigma Aldrich) hexane solution to ensure easy detachment after fabrication. Laser cutting (LPKF Protolaser R) of Zn foils (25 μm thick, Goodfellow, USA) into 1 mm in diameter (500 μm in diameter for the rat model) disks formed ultrasonic indicators. Assembling the Zn disks into the designated symmetric pattern onto the partially cured hydrogel film and subsequently blade coating an additional 150 μm thick hydrogel layer (100 μm thick for the rat model) enclosed the disks in the middle. Punching the hydrogel into desired disks using a hollow hole punch with preset diameter defined the sensing part of the BioSUM1 and BioSUM2. Forming an additional coating of ~10 μm p(DPAEMA-DMAEMA) hydrogel layer onto BioSUM3 completed the sensing part of BioSUM3. The diameter of the sensing part for BioSUM1 was 7 mm (4 mm for the rat model), and that for BioSUM2 and BioSUM3 was 6 mm (3.5 mm for the rat model). Punching a hydrogel film of 500 μm thickness (250 μm thick for the rat model) into a 5 mm diameter disk with a 2 mm diameter hole (3 mm diameter disk with 1 mm diameter hole for the rat model) formed the suture ring. Assembly of the sensing part and the suture ring using an additional layer of hydrogel precursor followed by UV irradiation under a nitrogen atmosphere completed the fabrication.

Acquisition of ultrasound B-mode images

A medical ultrasound instrument (GE LOGIQ P9, GE Healthcare) paired with a transducer (C1-5 broad-spectrum convex array transducer, 5 MHz frequency, GE Healthcare, unless otherwise stated) yielded images for the in vitro and in vivo tests. Applying ultrasound gel (MediChoice ultrasound gel, MAC Medical Supply Co, USA) at the interface, manually adjusting the gain, dynamic range, time gain compensation (TGC), and setting the focal zone at the depth of the BioSUM enabled capture of high-quality B-mode images. The measurement function of the instrument yielded the distance between the left and right bright segments corresponding to the Zn disks in the BioSUM. The maximum rate of decrease in the image contrast at these segments, as judged by the operator and validated by an automated image analysis algorithm (MATLAB coding), defined the positions of their edges. Post-processing of images involved coloring the grayscale images to yield the final B-mode images by the Lookup Table in ImageJ. The ultrasonic detection of BioSUMs in an alternative imaging system adopted the ultrasound instrument (Canon Xario 200) paired with a 18L7 transducer.

Finite Element Analysis (FEA) of hydrogel swelling

The commercial software COMSOL 6.0 was used to perform the coupled mechanical-transport FEA to establish the swelling ratio as a function of time. One-quarter of the device was modeled due to its symmetry. Second-order elements were implemented for displacements, while first-order elements were employed for the chemical potential of water. Initially, equilibrium swelling ratios were computed through steady state simulations to get the Flory-Huggins parameters at different pH levels (as detailed in the supplementary text). Subsequently, time-dependent simulations were applied to compute the swelling ratio curves at different pH levels across the three types of hydrogels after fully swollen in pH 7.4, thereby facilitating the determination of diffusivity constants.

Ultrasonic determination of the swelling behaviors

The system described above yielded data on the time-resolved swelling of BioSUM upon exposure to changes in pH. Immersion in phosphate buffered saline (PBS, pH 7.4, Sigma Aldrich) for 24 h prior to the tests stabilized the dimensions of the BioSUM. Immersion in pH buffer solutions for designated time intervals and followed by placement between two pork phantoms (pork loin chops) with different thicknesses (2-cm thick top layer for the rat model and 6-cm for the porcine model) to simulate the in vivo detection environment. Manually moving the ultrasound transducer across the top surface, adjusting the angles and targeting signals from the three dots along the diameter yielded images for analysis. Measuring the distances as described above allowed determination of the swelling ratio in length ($\Delta L/L_0$%). Each data point in the plot corresponds to measurements from 3 samples.

Direct measurements of the sensitivity

As described above, immersion in PBS (pH 7.4) for 24 h preceded the introduction of designated amounts (0.1 mL, 0.2 mL, 0.5 mL, 1 mL, and 2 mL) of simulated gastric fluid (pH 1.2, Ricca Chemical Company), simulated intestinal fluid (pH 6.8, Ricca Chemical Company), and simulated pancreatic juice (pH 8.2, Biochemazone) directly onto BioSUM1, BioSUM2, and BioSUM3 in evaluations of their sensitivity. Optical measurement of the distances between disks on opposite ends at 1, 3, 5, 10, 15, 20, 25 and 30 min, and converting the results into swelling ratios in length ($\Delta L/L_0$%) defined the sensitivity. Linear fitting of $\Delta L/L_0$% determined the response

time to reach a swelling ratio of 10%. Each data point in the plot corresponds to measurements from 3 samples.

Demonstrations of spatio-temporal sensing

The experiments involved introducing 250 mL PBS (thickness = 1.25 cm) into a tank (40 cm in length, 5 cm in width) with a substrate of 1% (w/v) agarose gel. Placing 7 BioSUM1s (pre-soaked in PBS for 24 h prior to the tests) along a line with a separation distance of 5 cm and then introducing 15 mL simulated gastric fluid (SGF) at one side led to a spatiotemporally varying pH, dictated by convection. This set up aims to resemble the in vivo situations that involve small leaks (~3 mL) by scaling the total amount of fluid, as the normal fluid amount in the peritoneal cavity is between 50 and 75 mL (*42*). Optically recording the swelling ratio of each BioSUM1 at time intervals of 5 min for up to 30 min produced a set of values relative to those of the BioSUM1 located at 0 cm at 30 min. Each data point in the plot corresponds to 3 independent measurements.

Tests of biodegradation

Immersion of BioSUM into PBS (pH 7.4) at 37 °C and 95 °C tested the biodegradation. The PBS solution was changed every two days.

Gravimetric analysis served to quantify the biodegradation of hydrogel films without Zn disks. Soaking pre-weighed hydrogel samples in PBS (pH 7.4) at 37 °C, 75 °C and 95 °C, washing the samples with deionized water to remove residual salts, and drying in a vacuum oven on designated days enabled measurements of dry weights. The ratio of the dry weight to the initial weight defined the percentage of the remaining hydrogels. The PBS solution was changed every two days.

Characterization of mechanical properties

Dynamic mechanical analysis (DMA, RSA-G2 Solids Analyzer, TA Instruments) defined the stress-strain relationships in uniaxial tension tests with a constant moving speed of 5 mm/min. Measurements included hydrogel films without Zn disks (5 mm in width, 10 mm in length, 300 μm in thickness, pre-swollen in the PBS solution or simulated fluids for 24 h). Mechanical properties from each BioSUM were measured 3 times.

The measurement of wear rates used sandpaper of 400 grit (Gator & Co) to press onto the hydrogel material. Moving the paper back and forth for a total of 100 cycles wore the hydrogel. The weight of the hydrogel was measured every 10 cycles.

Numerical simulation of ultrasound B-mode imaging

The wave propagation and ultrasound B-mode imaging were simulated by MATLAB ultrasound toolbox MUST (*43–45*). The model consisted of the transducer, the tissue and the sensor (**fig. S32A**). The transducer consisted of 192 elements (length = 0.17 mm for each element) that can induce and receive pressure waves independently. The pitch, i.e. distance between adjacent elements, was 0.2 mm such that the total length of the transducer was L_T = 38.37 mm. The transducer was placed at the top of the tissue to induce acoustic waves. The tissue length, width and thickness were much larger than the transducer. The acoustic wave velocity and density of tissue were c_{Tissue} = 1540 m/s (*39*) and ρ_{Tissue} = 1 g/cm^3, respectively, such that the acoustic impedance was $z_{Tissue} = c_{Tissue}\rho_{Tissue}$ = 1.54 MPa·s/m. The device consisted of N disk-shaped metal disks of diameter D_{Metal}, thickness h_{Metal} and acoustic impedance z_{Metal}, with one metal disk at the center and the rest uniformly patterned on the perimeter. The diameter of the device, defined as

the distance between the edges of metal disks at opposite ends (**fig. S32B**), was much smaller than the transducer length L_T and width W_T. The hydrogel that enclosed the metal disks in the experiment was considered as the same material as the tissue, because its acoustic wave velocity and density are very close to those of the tissue (*39*). The device was embedded in the tissue at a depth of H. In the simulation, the pressure received by the transducer elements was calculated by the functions in the toolbox based on the reflection coefficient $r = \left| \frac{z_{\text{Metal}} - z_{\text{Tissue}}}{z_{\text{Metal}} + z_{\text{Tissue}}} \right|$ at the tissue/metal interface. The background noise was simulated by randomly placing noise particles with reflection 1.0 and volume density 18.0/cm^3 (number of particles per unit volume, fitted based on experimental results of the signal-to-noise ratio). The baseline values of the above parameters were D_{Metal} = 1 mm, h_{Metal} = 25 μm, H = 10 cm, acoustics wave velocity and density of metal (Zn) c_{Metal} = 2780 m/s and ρ_{Metal} = 7.14 g/cm^3 ($z_{\text{Metal}} = c_{\text{Metal}}\rho_{\text{Metal}}$ = 19.8 MPa·s/m), respectively.

Characterization of measurement accuracy

Characterization of measurement accuracy used BioSUM placed between two pieces of pork phantoms with various thicknesses of the top layer (2 cm, 4 cm, 6 cm, 8 cm, 10 cm and 15 cm). Placing the ultrasound transducer on the top surface captured BioSUM in ultrasound B-mode and yielded images of 3 equally distributed bright segments with the maximum distance in between. MATLAB (coding available from the authors upon request) extracted the pixel intensity plot of BioSUM, defined the edge of BioSUM as the maximum slope in the intensity plot and calculated the pixel distance in between (**fig. S34A**). Further conversion into the distance in the centimeter scale based on the depth scale bar of images provided the measurement length of BioSUM underneath different depths of the pork phantom. Deviation of measurement length divided by the ground truth length of BioSUM quantified the measurement accuracy. The measurement from 3 samples formed one data point in the plot.

Characterization of signal-to-noise ratio (SNR)

Similar to the characterization of measurement accuracy, the characterization of signal-to-noise ratio (SNR) began with placing BioSUM between two pieces of pork phantoms with the thickness of the top layer varying from 2 cm to 15 cm. Obtaining 3 equally distributed bright segments with the maximum distance in between represented signals of BioSUM in ultrasound B-mode. A rectangle of 0.2 cm × 0.4 cm, including the bright segment, defined the regions of interest (ROIs) of signals from BioSUM, and a rectangle of 3 cm long × 1 cm high around the same depth of BioSUM defined the ROI of the background. Performing linear regression based on the dynamic range of individual image converted pixel intensity into decibel (dB) units. Extracting the average grayscale values from signals with background subtraction and further conversion into contrast in dB unit quantified SNR values at different depths (**fig. S34B**). The measurement from 3 samples formed one data point in the plot.

Implantation in rodent models

The experimental procedures with rat models followed approvals from the Institutional Animal Care and Use Committees at Washington University in St. Louis (protocol #22-0022). Adult male Lewis rats (8-10 weeks old) were purchased from Charles River Laboratories, Wilmington, MA. All rats were provided with food (PicoLab rodent diet 20, Purina Mills Nutrition International, St. Louis, MO) and water *ad libitum*. The surgical procedure started with sterilization using betadine and isopropanol solutions, and anesthesia with inhaled isoflurane vapor (4% for

induction and 2% for maintenance) during the implantation surgery. Placing the rats in the supine position and performing laparotomy with a 3-cm midline incision on the abdomen exposed related organs. Gently exposing the stomach with atraumatic forceps allowed for implantation of BioSUM1 (pre-soaked in PBS at a pH of 7.4 for 24 h prior) by securing it with sutures via the ring. Similarly, exposing the intestine gently by holding it with atraumatic forceps facilitated the implantation of BioSUM2 (pre-soaked in PBS at a pH of 7.4 for 24 h prior). Exposing the pancreas enabled implantation of BioSUM3 (pre-soaked in PBS at a pH of 7.4 for 24 h prior), which included procedures of exteriorizing the duodenum and spleen by holding the stomach with atraumatic forceps, mobilizing the stomach and spleen through omentectomy, mobilizing the area between the colon and pancreas, and exposing the portal vein.

Ultrasound images of BioSUM captured using a 15 MHz transducer (ML6-15 broad-spectrum linear matrix array transducer, 15 MHz frequency, GE Healthcare) immediately after implantation and abdominal closure defined the results for Day 0. Similar measurements on Day 1, Day 2, Day 3, Day 7, and Day 14, each collected while the rats were under anesthesia, defined a stabilization period with no expected changes in pH. Postoperatively, all rats were monitored for signs of infection and distress daily, and no laparotomy was performed during the 14-day period. Disruption of gastrointestinal organs on Day 14 simulated anastomotic leakage. 3-mm gastrotomy on the front wall of the stomach and enterotomy on the wall of the small intestine initiated gastric and intestinal leakage, respectively, in separate experiments. Resection of the tail of the pancreas initiated pancreatic leakage. The rats were euthanized with pentobarbital (150 mg/kg) after monitoring the leakage by ultrasound for 2 h.

Implantation in porcine models

The experimental procedures with porcine models followed approvals from the Institutional Animal Care and Use Committees at Northwestern University and Washington University in St. Louis (protocol #23-0028). The studies involved using both sexes of domestic swine (Sus domesticus) weighing 100-110 lbs. Anesthesia procedures included sedating the animals, placing them in a dorsal recumbent position, followed by intramuscular administration of telazol (4 mg/kg), ketamine (2 mg/kg), and xylazine (2 mg/kg). Using supplemental oxygen with isoflurane (inhalation at 1-5%) maintained anesthesia, while monitoring body temperature rectally and peripherally, and monitoring oxygen saturation and heart rate via a pulse oximeter. Laparotomy began with placing animals in a supine position. Placing BioSUM1 on the stomach body, BioSUM2 on small intestines, and BioSUM3 on the pancreas, (each pre-soaked in PBS at a pH of 7.4 for 24 h prior). Ultrasound imaging of the initial dimensions occurred after abdominal closure. Reopening the abdomen and disrupting the respective organs initiated fluid leakage. Creation of a gastrotomy on the front gastric wall adjacent to BioSUM1 (distance between BioSUM1 and incision varied between 2 cm and 5 cm) stimulated gastric leakage. Similarly, a 1-cm enterotomy near BioSUM2 on the small intestine (distance between BioSUM2 and incision varied between 2 cm and 5 cm) simulated intestinal leakage. Resection of the pancreas tail adjacent to BioSUM3 (distance between BioSUM3 and incision varied between 2 cm and 5 cm) initiated pancreatic leakage. Closing the abdominal wall immediately after creating these gastrointestinal leaks allowed ultrasound imaging to monitor dimensional changes of BioSUMs for 2 h. Sham experiments involved placing BioSUMs on the designated organs without subsequent disruption, with similar imaging procedures. The BioSUMs were subsequently collected to evaluate their integrity, and the animals were euthanized with pentobarbital (150 mg/kg).

In vitro tests of cytocompatibility

In vitro cytocompatibility tests involved L929 (a mouse fibroblast cell line representing connective mouse tissue) for the cell culture, CellTiter-Glo® Luminescent Cell Viability Assay (Promega, G7571) as the cell viability assay, both the Live/Dead cytotoxicity kit (Invitrogen, L3224) with BioTek Lionheart system for imaging, and Microplate reader Synergy H1 as the plate reader. BioSUM1, BioSUM2, and BioSUM3 were 2 mm in diameter and 200 μm thick with a 500 μm diameter, 25 μm thick Zn disk in the center, the dimensions of which proportionally decreased from the original values. Cytotoxic concentration of dimethyl sulfoxide (DMSO) served as positive control. Biocompatible crosslinked polyethylene glycol diacrylate (PEGDA, M_n 250) (*46*) served as negative control. Introducing 1 wt% biocompatible photoinitiator Irgacure 2959 (*47*) and subsequent UV exposure (365 nm, 500 mW/cm^2) for 4 min under a nitrogen atmosphere yielded the crosslinked PEGDA M_n 250. L929 cells were seeded in 24-well plates at a density of 10,000 cells per well. Treatment of three types of BioSUMs prior to transfer to 24-well plates included soaking in PBS (pH 7.4) for 24 h, sterilization in 75 % ethanol for 1 h, soaking in culture media for 24 h and sterilization by UV exposure for 1 h. BioSUMs were directly incubated with cells. Three individual samples were removed on designated days (day 1, day 4, and day 7) for imaging and cell viability assay.

Evaluation of biocompatibility

All procedures were approved by the Institutional Animal Care and Use Committee of Washington University in St. Louis protocol (protocol #22-0022). Adult male Lewis rats (8-10 weeks old) were purchased from Charles River Laboratories, Wilmington, MA. The implantation procedures of BioSUM were the same as described above. Daily monitoring of the rats confirmed their healthy conditions and stress levels. Euthanizing four rats at 2-, and 4-weeks post-implantation enabled explantation of organs, including the stomach, pancreas, and intestine, for histological evaluations. Organs were stored in 10% neutral buffered formalin in 50-ml centrifuge tubes. Staff at the Mouse Histology and Phenotyping Laboratory at Northwestern University conducted paraffin embedding, sectioning (section thickness = 4 μm, 1-2 tissue cuts on each slide), and hematoxylin and eosin (H&E) staining based on standard protocols. Explantation of heart, lung, kidney, spleen, and extraction of blood from the heart with 26-g syringes at 2-, and 4-weeks post-implantation enabled elemental analysis by staff at the Quantitative Bio-element Imaging Center (QBIC) at Northwestern University. Organs and blood for elemental analysis were stored in pre-weighed 50-ml centrifuge tubes at -20 °C. Subsequent dissolution of tissues by addition of 1.5 mL nitric acid and 0.35 mL hydrogen peroxide and dilution to 10 wt% allowed for ICP-MS analysis of Zn concentrations. Blood chemistry tests used blood samples collected from the heart with 26-g syringes at 2-, and 4-weeks post-implantation. Samples were collected in serum separator tubes and spun to separate serum from clotted red cells. The serum layers were transferred to another empty tube and kept at -20 °C. Staff at the Veterinary Diagnostic Laboratory at the University of Illinois Urbana-Champaign conducted tests on these blood samples.

Statistical analysis

Required sample sizes were estimated based on previous publications and experience. The numbers of replicates are reported, and several internal replications are present in the studies. No data were excluded after analysis. Animals were randomly assigned to treatment groups. Group statistical analyses were performed using GraphPad Prism software (GraphPad, LaJolla, CA) and Origin (OriginLab, Northampton, MA). For N sizes, the number of trials and the number of animals are provided. All data are expressed as mean ± SD or individual plots. For multiple group

comparisons, one-way or two-way analysis of variance (ANOVA) tests were used for normally distributed data, followed by post hoc analyses reported in Figure legends. $p < 0.05$ was considered statistically significant.

Supplementary Text

Monitoring homeostatic dysregulation

BioSUMs enable detection of unpredictable leakage and assessment of different cases of homeostatic dysregulation in deep tissues. The technique relies on converting dimensional changes of a shape-adaptive matrix material into ultrasound-readable signals. Designs of BioSUMs reported here allow for the monitoring of pH changes associated with anastomotic leakage following GI surgeries, pleural effusion (*48*), ascites (*49*) and complex infections. Other materials and ultrasonic indicators create opportunities for monitoring other forms of homeostatic dysregulation. An example in the context of detecting brain hemorrhage may incorporate a hemostatic agent (*50*) inside the matrix material. Specific binding with red blood cells and absorption of blood will result in expansion as the basis for ultrasound detection. Alternatively, thermoresponsive materials such as those that incorporate polyethylene glycol grafted into a chitosan hydrogel (*51*) may enable sensing of changes in temperature. These examples suggest broad applicability of the BioSUM concept in the assessment of diverse forms of homeostatic dysregulation in deep tissues.

Integration of BioSUMs onto tissue surfaces with bioresorbable adhesives

Bioresorbable adhesive (*52*) can be used to integrate BioSUM onto tissue surfaces as an alternative approach to anchoring the device for postoperative monitoring. The integration starts with coating the tissue surfaces with a primer layer consisting of chitosan, sulfated N-hydroxysuccinimide (Sulfo-NHS) and (1-ethyl-3-(3-dimethylaminopropyl) carbodiimide (EDC), followed by applying the two-component bioresorbable adhesive onto the device and tissue surfaces. The two-component adhesive is a viscous liquid solution of a photocurable covalent network of polyethylene glycol-lactide acid diacrylate (PEG-LA-DA) and an ionic network of sodium alginate. Exposure to UV light (365 nm, 20 mW/cm^2) for 3 min completes the integration of the device onto tissue surfaces with robust chemical bonding (**fig. S1**).

The photo-triggered liquid-solid transformation of the bioresorbable adhesive enables the formation of bonding without applying external forces, thereby facilitating the integration procedure, and minimizing the potential damage to the tissues. The primary amine groups in chitosan form chemical bonds with negatively charged carboxylic acid groups on tissue surfaces and the sodium alginate in the adhesive. The Sulfo-NHS and EDC promote robust bonding between the adhesive and the BioSUM. All components in the adhesive undergo controllable bioresorption via natural processes. The timeframe is tunable from 20 days to several months in PBS (pH = 7.4) at 37 °C depending on the molecular weight of lactide (LA) content, to align timescales that satisfy clinical requirements.

The severity of anastomotic leakage and detection of leakage via BioSUMs

Anastomotic leakage is a major cause of morbidity and mortality in postoperative complications that often occur during the 2 week period after surgeries (*53*). The incidence rate

ranges from 5% to 25% depending on the sites of anastomosis (*29*), posing a significant risk to patients undergoing GI surgeries. Early symptoms such as stomach pain, fever, and nausea are often indistinguishable from causes for other diseases. As such, identification of anastomotic leakage in many cases occurs too late to prevent symptoms from being severely septic and life-threatening.

In addition, no standard approaches for diagnosis currently exist in clinical practice. Clinical assessments rely on a variety of methods and criteria (*53*, *54*), including external symptoms, contrast-enhanced computed tomography (CT), laboratory biomarkers such as C-reactive protein and amylase, and endoscopy. These approaches are either high in cost, invasive, or they pose substantial risks of radiation exposure. Therefore, a remaining challenge lies in detecting anastomotic leakage accurately to enable early therapeutic interventions.

In this context, implantation of BioSUMs near the anastomosis during the surgery enables post-surgical monitoring and detection of potential anastomotic leakage in a timely and reliable manner. If no leakage occurs postoperatively, the dimensions of BioSUMs will show minimal fluctuations with a stable distance between Zn disks in ultrasound B-mode images. When leakage occurs, expansion of the BioSUMs will increase the distance between Zn disks in B-mode images as an indication of leakage. The dimensions of the BioSUMs reflect the local pH values associated with the leak, serving as a potential indicator for leakage severity. After the diagnosis, the BioSUMs resorb into the body via natural processes and metabolic reactions, eliminating the need for extra surgical interventions.

Bioresorption of the hydrogel materials used in BioSUMs

Bioresorption of the hydrogel materials used in BioSUMs is mainly attributed to hydrolytic chain scission reactions via a synergistic effect of the hydrolyzable ester linkages (*55*) and the cationic or anionic nature of the pH-responsive blocks (*34*) (**fig. S7**). These hydrolyzable ester linkages from the PEGDA component form crosslinked hydrogel networks the enable hydrolysis of the backbone structures for all three BioSUMs (*55–57*). In addition, the ester linkages associated with the methacrylate of the pH-responsive blocks become susceptible to hydrolysis due to the process of protonation of tertiary amine and carboxyl functional groups that increases the hydrophilicity of polymer chains (*34*). Previous studies provide additional details about the mechanisms associated with hydrogel materials used in BioSUM1 and BioSUM2 (*35*, *58*, *59*), and hydrogel materials in BioSUM3 (*32*, *33*, *60*, *61*). These hydrolytic reactions lead to oligo(ethylene glycol), acrylic acid oligomers, and small molecular acids, which undergo further conversion into biocompatible and absorbable products (*31*, *35*) with the assistance of enzymes (*32*, *62*) and metabolic reactions (*63*).

Materials designs for BioSUMs

pH-Responsive hydrogel materials for BioSUM1 and BioSUM2 involve p(DMAEMA-DPAEMA) copolymers with ratios of 7:3 and 9:1 between DMAEMA and DPAEMA, respectively, designed to maximize their responses in relevant pH ranges while maintaining stable mechanical properties (**figs. S8-S9, tables. S2-S4**). Protonation of tertiary amine moieties in both DMAEMA and DPAEMA leads to a conformation change of the hydrogels from hydrophobic to hydrophilic as the pH decreases. DMAEMA exhibits a higher pKa value (~8.4) compared to DPAEMA (~6.3) (*35*, *64*). Therefore, a higher ratio of DMAEMA in the copolymer enables a larger swelling ratio for BioSUM2 near the physiological pH of 7.4, appropriate for the relevant

range of pH values in the small intestinal environment (pH ~6.8). A higher ratio of DPAEMA in the copolymer results in a larger Young's modulus and elongation at break in BioSUM1 (**table S4**), allowing stable operation in the strongly acidic environment.

The hydrogel material used in BioSUM3 contains pH-responsive monomer AAc and crosslinker PEGDA. The introduction of hydrophobic BA shifts the pKa value beyond the physiological pH of 7.4 (*36*). Similar to the designs for BioSUM1 and BioSUM2, tuning the AAc ratio and the degree of crosslinking aim to balance between the response of BioSUM3 in alkaline conditions and its mechanical properties (**figs. S9-S10, tables. S2, S3, S5**).

Selecting bioresorbable metals (Mg, Fe, Zn, Mo, W) as ultrasonic indicators takes into consideration their degradation rates (*30*) and acoustic impedance mismatch with the surrounding hydrogel and soft tissues. Numerical simulation results in **fig. S11** indicate similar SNR values for each of these metals. A comparison between their degradation rates in physiological conditions leads to the choice of Zn as ultrasonic indicators due to its capability to dissolve in several months.

The theoretical model and finite element analysis approach for the swelling of hydrogels

Chain extensions of pH-responsive monomers DMAEMA and DPAEMA for BioSUM1 and BioSUM2, and hydrophobic BA monomer for BioSUM3 into oligomers prior to crosslinking form grafted side chains in the hydrogel networks (*65*, *66*). These side chains together with physical entanglements attributed to the low crosslinking density provide BioSUM with considerable equilibrium swelling ratios within a timeframe of 2 h.

In the theoretical model, the force balance equation and mass conservation of the water govern the evolution of the gel (*37*, *38*, *67*). The force balance equation is

$$\mathrm{div}\,\boldsymbol{\sigma} = 0 \tag{1}$$

where $\boldsymbol{\sigma}$ is the Cauchy stress of the gel's network and it is expressed as

$$\boldsymbol{\sigma} = \frac{NkT}{J}(\mathbf{F}\mathbf{F}^T - \mathbf{I}) - \Pi\mathbf{I} \tag{2}$$

where $\mathbf{I}$ is the second-order identity tensor, $\mathbf{F}$ is the deformation gradient with respect to the dry polymer state, $J = \det\mathbf{F}$ is the volume swelling ratio of the gel, Π is the osmotic pressure, N is the number of chains per reference volume in the network, k is the Boltzmann constant and T is the absolute temperature.

The mass conservation equation of the water is

$$\frac{dC_m}{dt} + J\mathrm{div}\mathbf{j}_m = 0 \tag{3}$$

where C_m is the number of water molecules per volume of dry polymer and $\mathbf{j}_m$ is the flux of the water,

$$\mathbf{j}_m = -\frac{D}{kT}\frac{C_m}{J}\mathrm{grad}\mu_m \tag{4}$$

where D is the diffusivity, and μ_m is the chemical potential of the water, which is expressed as

$$\mu_m = kT\left(\ln\frac{J-1}{J} + \frac{1}{J} + \frac{\chi}{J^2}\right) + \Pi\nu \tag{5}$$

where χ is the Flory-Huggins parameters and ν is the volume of one water molecule. The parameter χ characterizes the hydrophilicity of the polymer network, thus governing the swelling ratio of the gel. Consequently, immersion of the gel in solutions with different pH values leads to variations in the quantity of fixed charges present within the network, yielding different χ values and resulting in different equilibrium swelling ratios.

A second-order continuous step function of the swelling ratio *J* models the diffusivity. This representation, implemented within COMSOL 6.0, effectively captures the phenomenon wherein diffusivity remains limited when the swelling ratio is small. Four parameters, namely D_l, D_h, J_{mid}, and J_{range}, collectively determine the relationship of *D* with *J* (**fig. S12**).

The incompressible condition postulates that both the polymer molecules and the water molecules are incompressible. Thus, any alteration in the volume of the gel is solely ascribed to the change in the water concentration:

$$J = 1 + \nu C_m \tag{6}$$

COMSOL 6.0 defines the finite element model and **fig. S13** demonstrates the set up. The geometry implemented in the model replicates the experimental setup, with one-quarter of the device modeled to account for inherent symmetry. In the first step, we fit χ at different pH levels by gel's equilibrium swelling ratio as measured by experiments (**fig. S14**). The results are within a reasonable range (*38*, *68*) and are close to the available literature values (*69*). *Nv* values of the sample are obtained from the experimental recipe; they are 0.055, 0.039 and 0.0068 for BioSUM1, BioSUM2, and BioSUM3, respectively. In the second step, the gel undergoes swelling from its initial state. Experimental results determine the initial swelling ratio. At time $t = 0$, the chemical potential, μ_m, at the external surface is set as 0, thereby facilitating the swelling process. Fitting the swelling curves across all pH conditions involves the proper selection of diffusivity constants. **Table S1** presents the fitted parameters. Proper diffusivity constants are selected to fit the swelling curve across all pH conditions. The fitted parameters are listed in **table S1** and they are close to literature values (*70*).

The theoretical model for the effect of metal thickness on the reflection of acoustic waves

A theoretical model in one-dimension was derived to study the effect of metal thickness on the reflection at the metal/tissue interface. A metal layer of thickness h_{Metal} was embedded in infinitely large tissues (**fig. S14**). In the one-dimensional case, the acoustic wave velocity in tissue c_{Tissue} is related to the modulus of tissue E_{Tissue} and density ρ_{Tissue} via $c_{\text{Tissue}} = \sqrt{\frac{E_{\text{Tissue}}}{\rho_{\text{Tissue}}}}$. Similarly, the acoustic wave velocity in metal is $c_{\text{Metal}} = \sqrt{\frac{E_{\text{Metal}}}{\rho_{\text{Metal}}}}$, with E_{Metal} and density ρ_{Metal} representing the modulus of metal and the density of metal, respectively. For a harmonic wave with frequency *f* (angular frequency $\omega = 2\pi f$), waves in the tissue above the metal ($z < 0$, **fig. S14A**) are the sum of the incident wave (U_{I}) and the reflected wave (U_{R}), such that the displacement can be expressed in complex form as

$$u_1 = U_{\text{I}} + U_{\text{R}} = A_{\text{I}} \exp\left[i\left(\omega t + k_{\text{Tissue}} z\right)\right] + A_{\text{R}} \exp\left[i\left(\omega t - k_{\text{Tissue}} z\right)\right], \tag{7}$$

where $k_{\text{Tissue}} = \frac{\omega}{c_{\text{Tissue}}}$ is the wavenumber, and i is the symbol for the complex number. The wave in the metal was the sum of the transmitted wave (U_{T}) at the metal/tissue interface at $z = 0$ and the reflected wave (U_{TR}) at the metal/tissue interface at $z = h_{\text{Metal}}$, such that the displacement in the metal is

$$u_2 = U_{\text{T}} + U_{\text{TR}} = A_{\text{T}} \exp\left[i\left(\omega t + k_{\text{Metal}} z\right)\right] + A_{\text{TR}} \exp\left[i\left(\omega t - k_{\text{Metal}} z\right)\right]. \quad (8)$$

The wave in the tissue below the metal is the transmitted wave (U_{TT}) at the metal/tissue interface at $z = h_{\text{Metal}}$, such that the displacement in the tissue below metal is

$$u_3 = U_{\text{TT}} = A_{\text{TT}} \exp\left[i\left(\omega t + k_{\text{Tissue}} z\right)\right]. \quad (9)$$

The continuity of displacements and stresses at the metal/tissue interfaces requires that

$$u_1 = u_2 \text{ and } E_{\text{Tissue}} \frac{\partial u_1}{\partial z} = E_{\text{Metal}} \frac{\partial u_2}{\partial z} \text{ at } z{=}0, \quad (10)$$

and

$$u_2 = u_3 \text{ and } E_{\text{Metal}} \frac{\partial u_2}{\partial z} = E_{\text{Tissue}} \frac{\partial u_3}{\partial z} \text{ at } z{=}z_{\text{Metal}}. \quad (11)$$

The ratio of the amplitude of the reflected wave over that of the incident wave at the metal/tissue interface at $z = 0$ can be solved as

$$\left|\frac{A_{\text{R}}}{A_{\text{I}}}\right| = \frac{2A_{\text{R}}\left(z_{\text{Metal}}^2 - z_{\text{Tissue}}^2\right)\sin\left(\frac{2\pi h_{\text{Metal}}}{\lambda_{\text{Metal}}}\right)}{\sqrt{\left(z_{\text{Metal}} - z_{\text{Tissue}}\right)^4 + \left(z_{\text{Metal}} + z_{\text{Tissue}}\right)^4 - 2\left(z_{\text{metal}}^2 - z_{\text{Tissue}}^2\right)^2 \cos\left(\frac{4\pi h_{\text{Metal}}}{\lambda_{\text{Metal}}}\right)}}, \quad (12)$$

where z_{Metal} and z_{Tissue} are the acoustic impedance of metal and tissue, respectively, and $\lambda_{\text{Metal}} = \frac{c_{\text{Metal}}}{f}$ is the wavelength in metal. Equation 12 suggests that when the metal thickness h_{Metal} is much smaller than the wavelength in metal λ_{Metal}, the amplitude of the reflected wave increases with $h_{\text{Metal}}/\lambda_{\text{Metal}}$. For the metal used in the current work (Zn) and a typical frequency of $f = 5$ MHz, $\lambda_{\text{Metal}} \approx 560$ μm, and the relationship of $\left|\frac{A_{\text{R}}}{A_{\text{I}}}\right|$ vs. $\frac{h_{\text{Metal}}}{\lambda_{\text{Metal}}}$ is shown in **fig. S14B**. The increase of $\left|\frac{A_{\text{R}}}{A_{\text{I}}}\right|$ almost saturates at $h_{\text{Metal}}/\lambda_{\text{Metal}} = 0.05$, which justifies the use of 25 μm thick Zn disks in this work.

Expansion of a BioSUM and ultrasound measurement in a curvilinear tissue environment

When a BioSUM is in the curvilinear tissue environment, the expansion is isotropic with minimal deviation of measurements between each pair of Zn disks (**fig. S28A-C**). FEA modeling results (**fig. S28D-F**) demonstrate less than 2% deviation between measurements at different circular angles under various swelling ratios. In the modeling, the device was placed on a rigid cylinder with a diameter of 2.5 cm to simulate the curvilinear condition, comparable to that associated with the average diameter of the small intestine (*71*).

In the case where the BioSUM lies on a curved surface of the GI organs, the signal from three dots along the diameter appears bent in the ultrasound B-mode image, with an actual length of the arc x_0 (**fig. S29A**). The sum of two straight lines from the left to the middle x_1 and the middle to the right x_2 form the measurement length x in ultrasonic measurement (**fig. S29B**). Considering the maximum deviation of ultrasonic measurement $\Delta x/x_0$ ~0.1 at the depth of 15 cm (**fig. S29C**),

$$\frac{x}{x_0} = \frac{x_2}{\frac{x_0}{2}} = \frac{2r\sin\frac{\theta}{2}}{r\theta} = \frac{\sin\frac{\theta}{2}}{\frac{\theta}{2}} = 0.9 \quad (13)$$

$$\theta \approx 90° \quad (14)$$

This result indicates that a bending curvature less than that of a semi-sphere is sufficient to provide an ultrasonic measurement with deviation smaller than 0.1, which is the case for GI organs (*72*, *73*).

Discussion on mechanical deformations

In clinical scenarios, BioSUM deployed in the GI tract may exhibit artifacts due to mechanical deformations of the stomach due to processes of consuming and digesting food. The presence of interstitial fluid between the device and the underlying tissue, and a single anchoring site (**fig. S39A**) lead to minimal effects of these processes on the dimensions of the device. Experimental and FEA modeling results (**fig. S39B**) show negligible changes of the measured distances between pairs of Zn disks. The experiments (**fig. S39C**) involve PBS solution between the device and an elastomeric substrate, to simulate the interstitial fluid and the adjacent soft tissue. Stretching the elastomeric substrate to ~60% mimics the mechanical deformation of the stomach before and after consuming food. Measurements of the distances between pairs of Zn disks before and after stretching the elastomer yield results in **fig. S39B**. FEA modeling approximates the shape of the stomach as a sphere, and takes the volume of the stomach in the fasting state, and fed state as 200 mL and 800 mL, with a continuous isotropic expansion over a period of 3 h (*74–76*). The expansion of the sphere imposes a tensile force on the device via shear through a thin layer of fluid. The results show that the shear pressure applied to the bottom surface of the device is 1.16×10^{-5} Pa. The resulting changes of displacement U of the device appear negligible (**fig. S39D**).

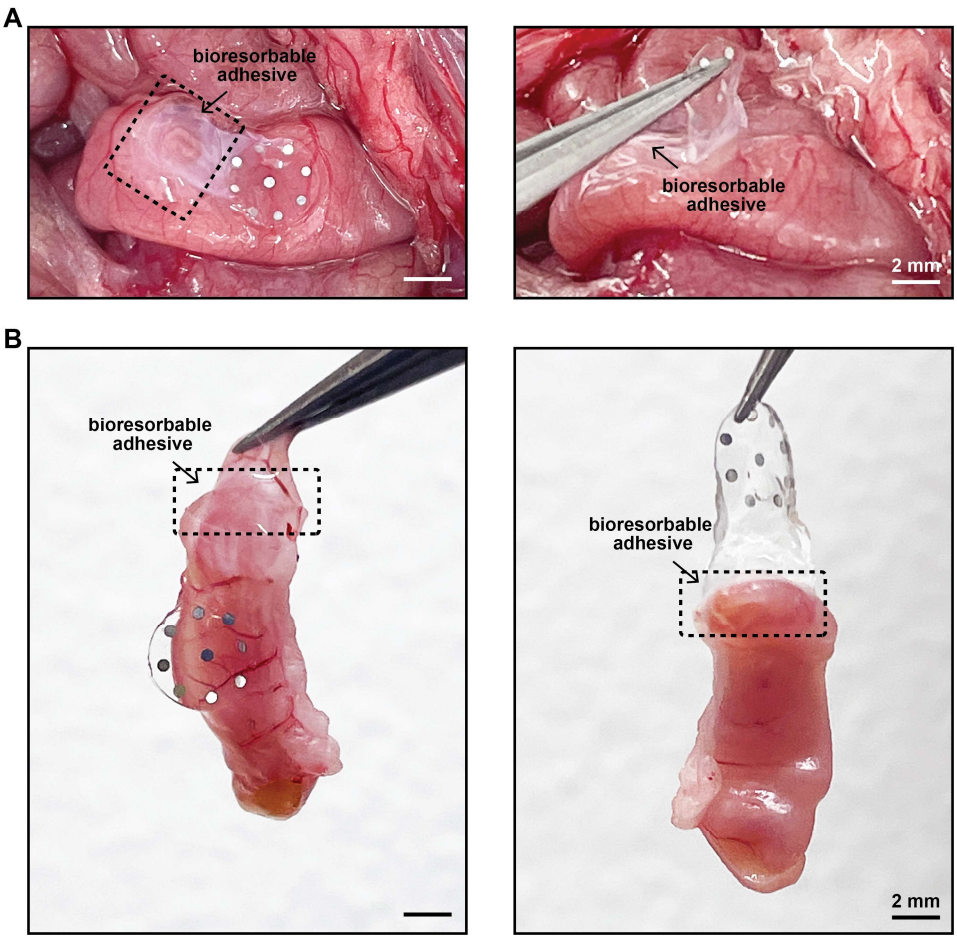

Fig. S1. Fixation and integration of a BioSUM onto the surfaces of soft living tissues using a bioresorbable adhesive. (**A**) Images of a BioSUM implanted in a rat model to demonstrate the adhesion between the device and the tissue. (**B**) Images of a BioSUM on explanted tissue to indicate the strength of the adhesion.

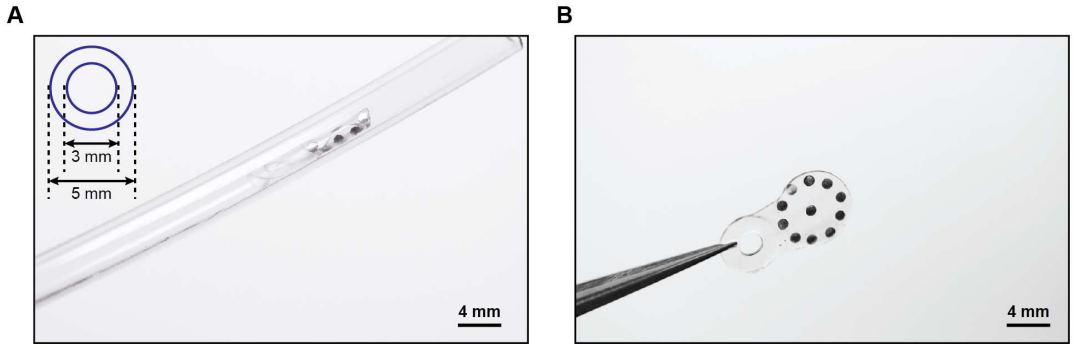

Fig. S2. Images of BioSUM that highlight the miniaturized and flexible designs, to facilitate implantation during laparoscopic surgeries. (**A**) One BioSUM rolled in a plastic tube with I.D. = 3 mm, O.D. = 5 mm. (**B**) Image of a BioSUM after rolled in the plastic tube.

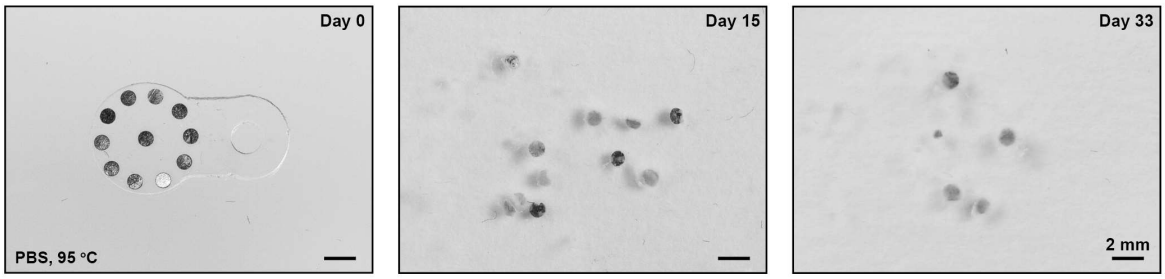

Fig. S3. Images of the accelerated dissolution of BioSUM1 in PBS (pH 7.4) solution at 95 °C.

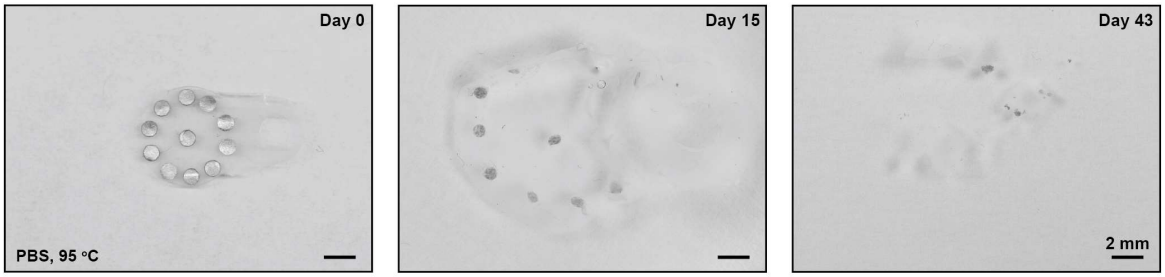

Fig. S4. Images of the accelerated dissolution of BioSUM3 in PBS (pH 7.4) solution at 95 °C.

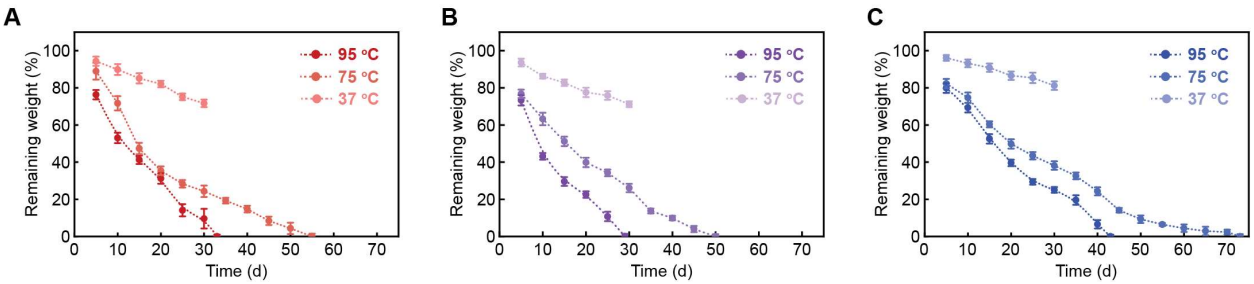

Fig. S5. Characterization of the kinetics of biodegradation through measurements of the weight of hydrogels without Zn disks as a function of time of immersion in PBS (pH = 7.4) at 37 °C, 75 °C, and 95 °C. (**A**) BioSUM1. (**B**) BioSUM2. (**C**) BioSUM3.

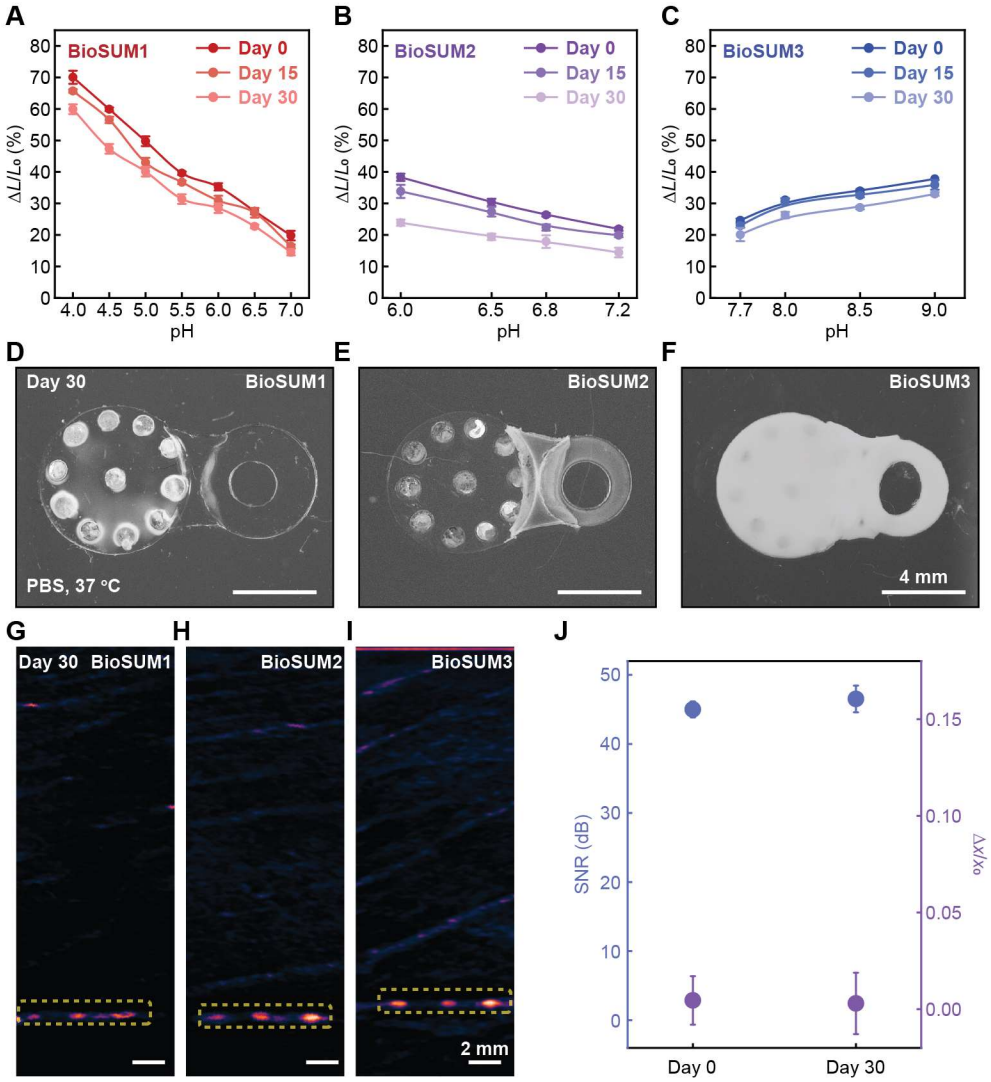

Fig. S6. pH-responsive behaviors and ultrasonic detection of BioSUMs after degradation in physiological conditions at 37 °C in PBS. (**A-C**) pH-responses at the equilibrium state after degradation for 15 days and 30 days. (**A**) BioSUM1. (**B**) BioSUM2. (**C**) BioSUM3. (**D-F**) Images of devices in PBS (pH 7.4) solution at 37 °C after 30 days. (**D**) BioSUM1. (**E**) BioSUM2. (**F**) BioSUM3. (**G-I**) Ultrasound B-mode images of devices between two pork phantoms at 2 cm depth after degradation for 30 days. (**G**) BioSUM1. (**H**) BioSUM2. (**I**) BioSUM3. (**J**) Comparison of the signal quality before and after degradation in PBS at 37 °C for 30 days. $\Delta x/x_0$ is the deviation of measured length divided by the actual length.

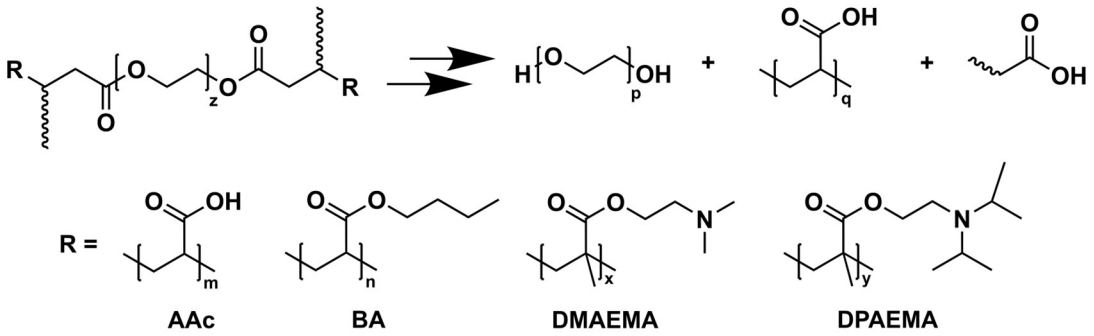

Fig. S7. Simplified schematic illustration of the bioresorption of hydrogel materials used in BioSUMs.

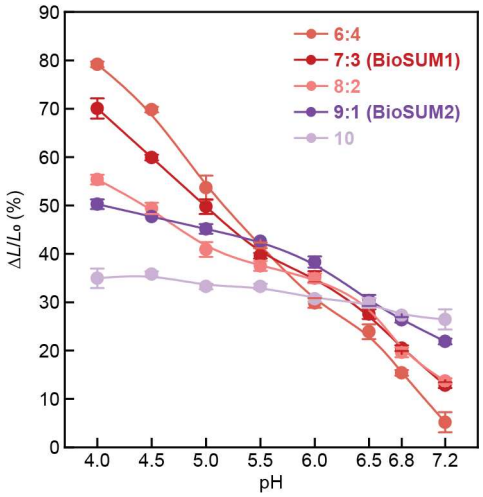

Fig. S8. Materials designs for BioSUM1 and BioSUM2. Equilibrium swelling ratios of hydrogel materials with different DMAEMA and DPAEMA ratios at relevant pH values. $\Delta L/L_0$ (%) denotes the swelling ratio.

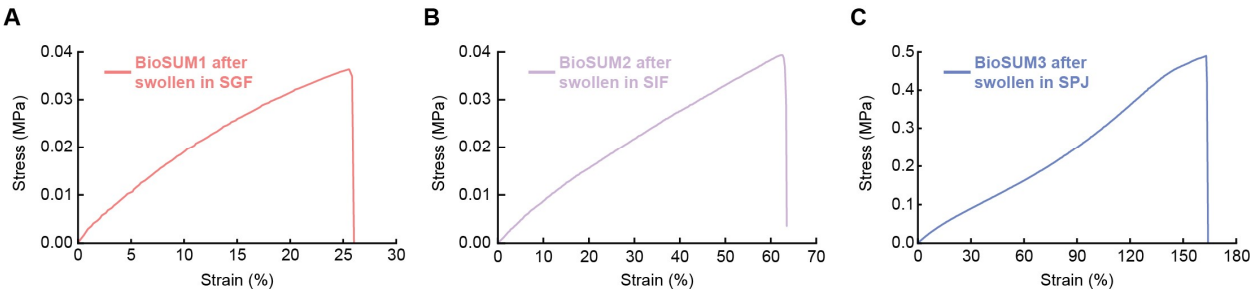

Fig. S9. Stress-strain curves of pH-responsive BioSUM materials after fully swollen in simulated fluids. (**A**) BioSUM1 after swollen in SGF (pH = 1.2). (**B**) BioSUM2 after swollen in SIF (pH = 6.8). (**C**) BioSUM3 after swollen in SPJ (pH = 8.2).

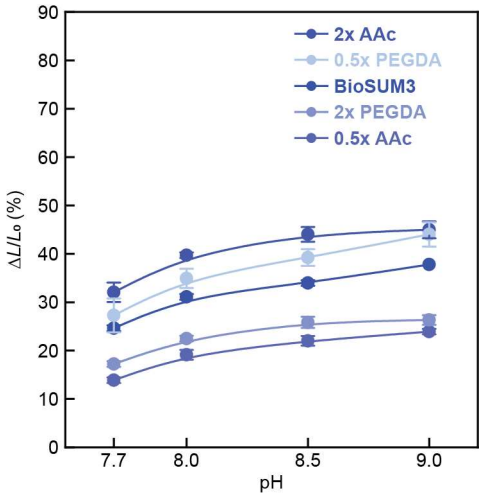

Fig. S10. Materials designs for BioSUM3. Equilibrium swelling ratios of hydrogel materials with different AAc ratios and degrees of crosslinking (PEGDA ratios) compared to BioSUM3 at relevant pH values. $\Delta L/L_0$ (%) denotes the swelling ratio.

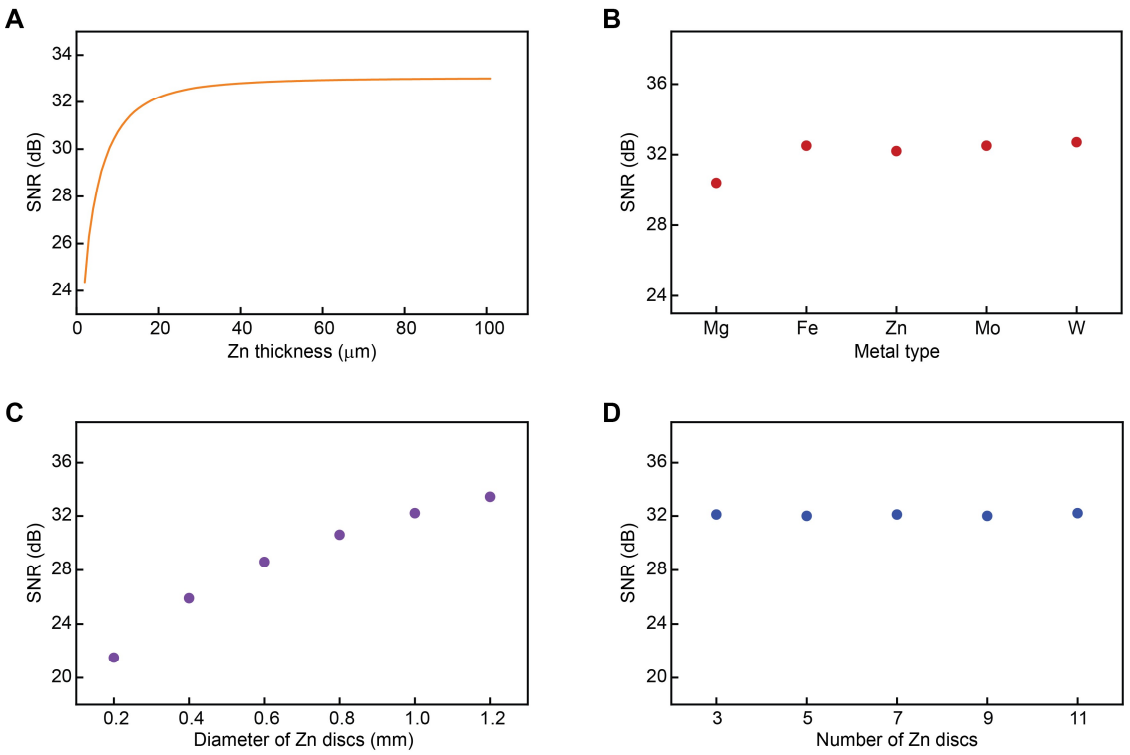

Fig. S11. Numerical simulation results for the effects of different parameters on SNR values at 10 cm depth at a frequency of 5 MHz. (**A**) Effect of Zn thickness. (**B**) Effect of metal type. (**C**) Effect of the diameter of Zn disks. (**D**) Effect of the number of Zn disks (including Zn disk at the center).

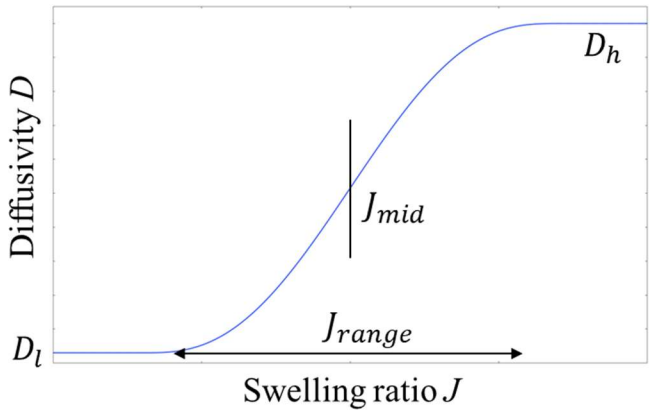

Fig. S12. Diffusivity (*D*) as a function of swelling ratio (*J*). A second-order continuous step function of swelling ratio J models the diffusivity D. Four parameters, D_l, D_h, J_{mid}, and J_{range}, determine the function.

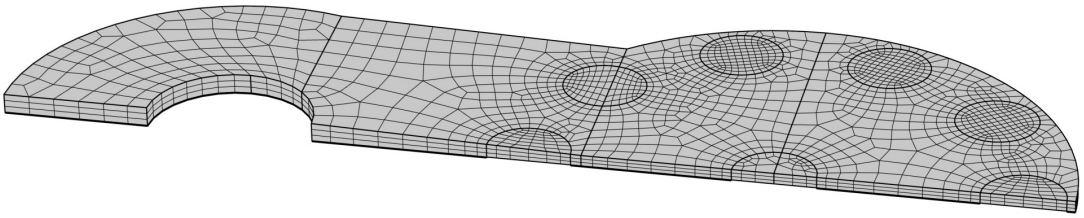

Fig. S13. The geometry configuration of the model. The front and bottom planes are symmetric planes.

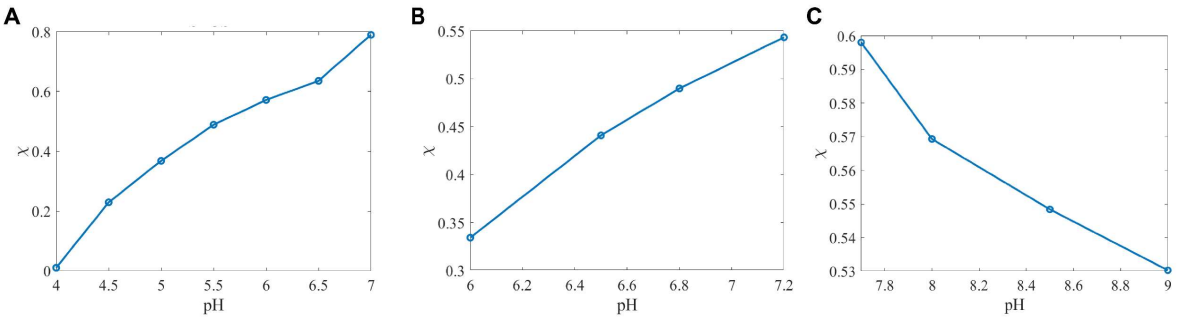

Fig. S14. The fitted χ values at different pH values for three types of hydrogels. (**A**) BioSUM1. (**B**) BioSUM2. (**C**) BioSUM3.

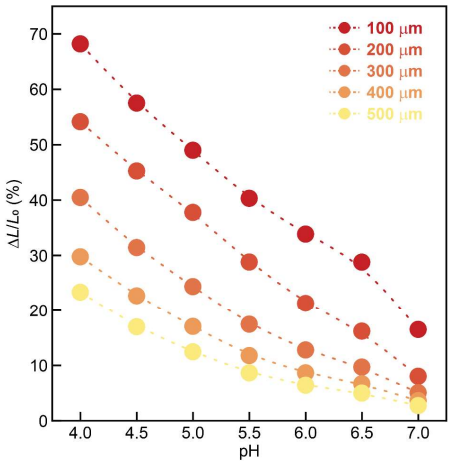

Fig. S15. FEA results for thickness-dependent swelling ratios of BioSUM1 at different pH values after 10 min. $\Delta L/L_0$ % denotes the percentage change in length.

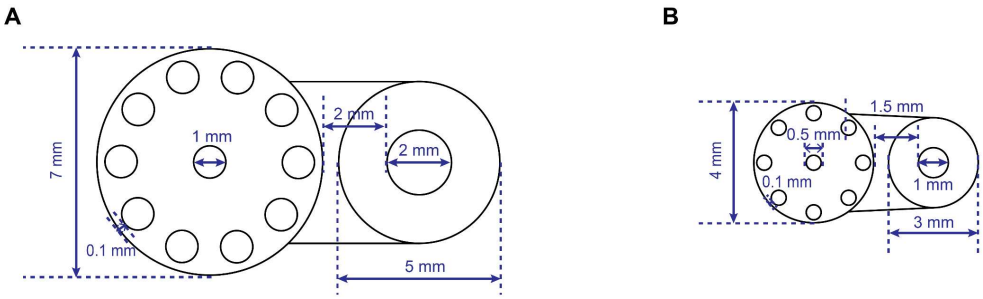

Fig. S16. Designs of BioSUMs. (**A**) Design for the large animal model. (**B**) Design for the small animal model.

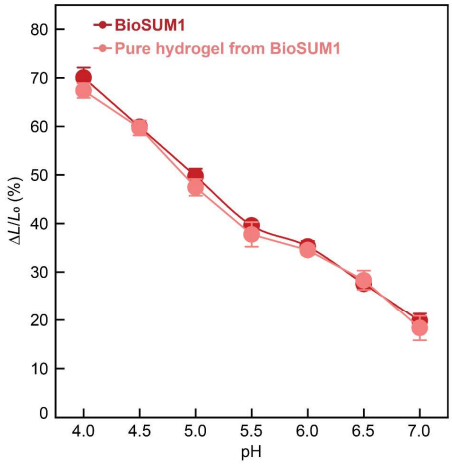

Fig. S17. Comparison between the pH response of BioSUM1 and the hydrogel for BioSUM1 without the Zn disks, evaluated at the equilibrium states.

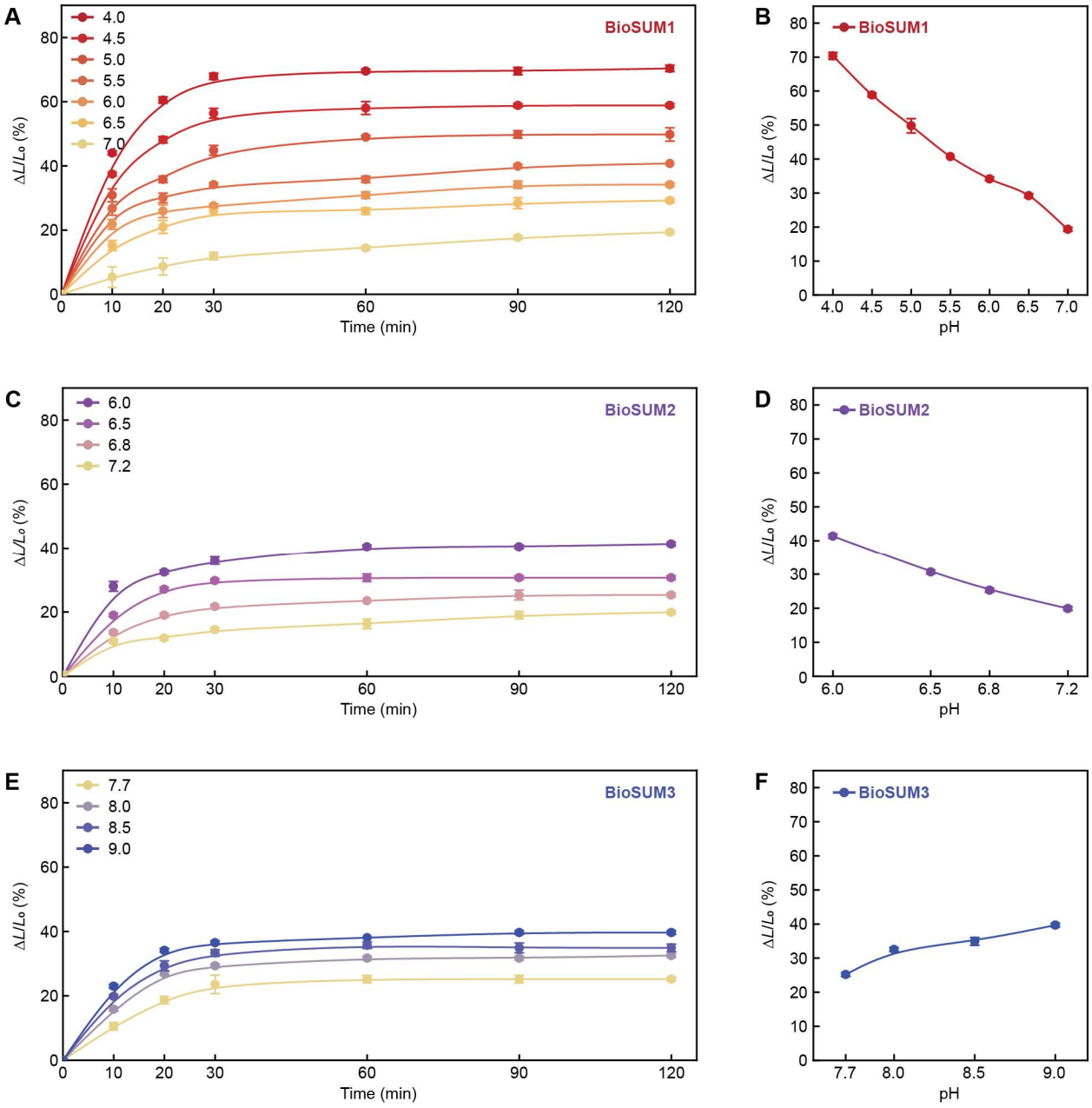

Fig. S18. pH-responsive behavior of BioSUMs designed for a rat model. (**A, C, E**) Time-resolved responses of BioSUM to different pH values. $\Delta L/L_0$ (%) denotes the swelling ratio in length. (**A**) Response of BioSUM1. (**C**) Response of BioSUM2. (**E**) Response of BioSUM3. (**B, D, F**) Response of BioSUM to different pH values at the equilibrium state. (**B**) Response of BioSUM1. (**D**) Response of BioSUM2. (**F**) Response of BioSUM3.

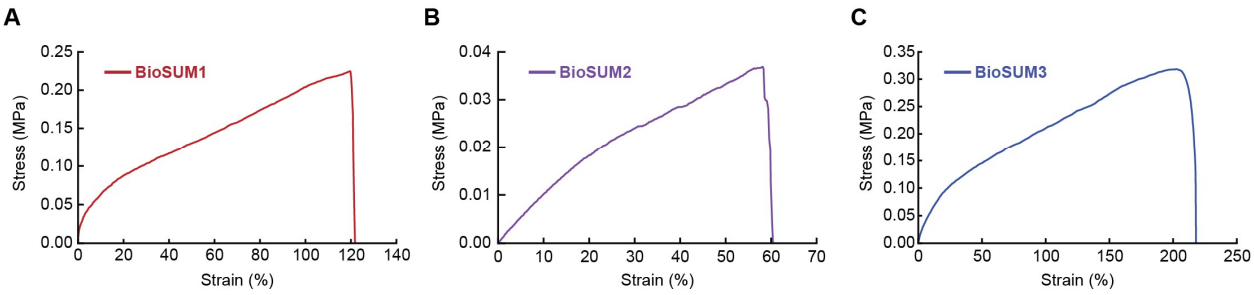

Fig. S19. Stress-strain curves of pH-responsive hydrogels in BioSUMs after fully swollen in PBS (pH 7.4) solution. (**A**) BioSUM1. (**B**) BioSUM2. (**C**) BioSUM3.

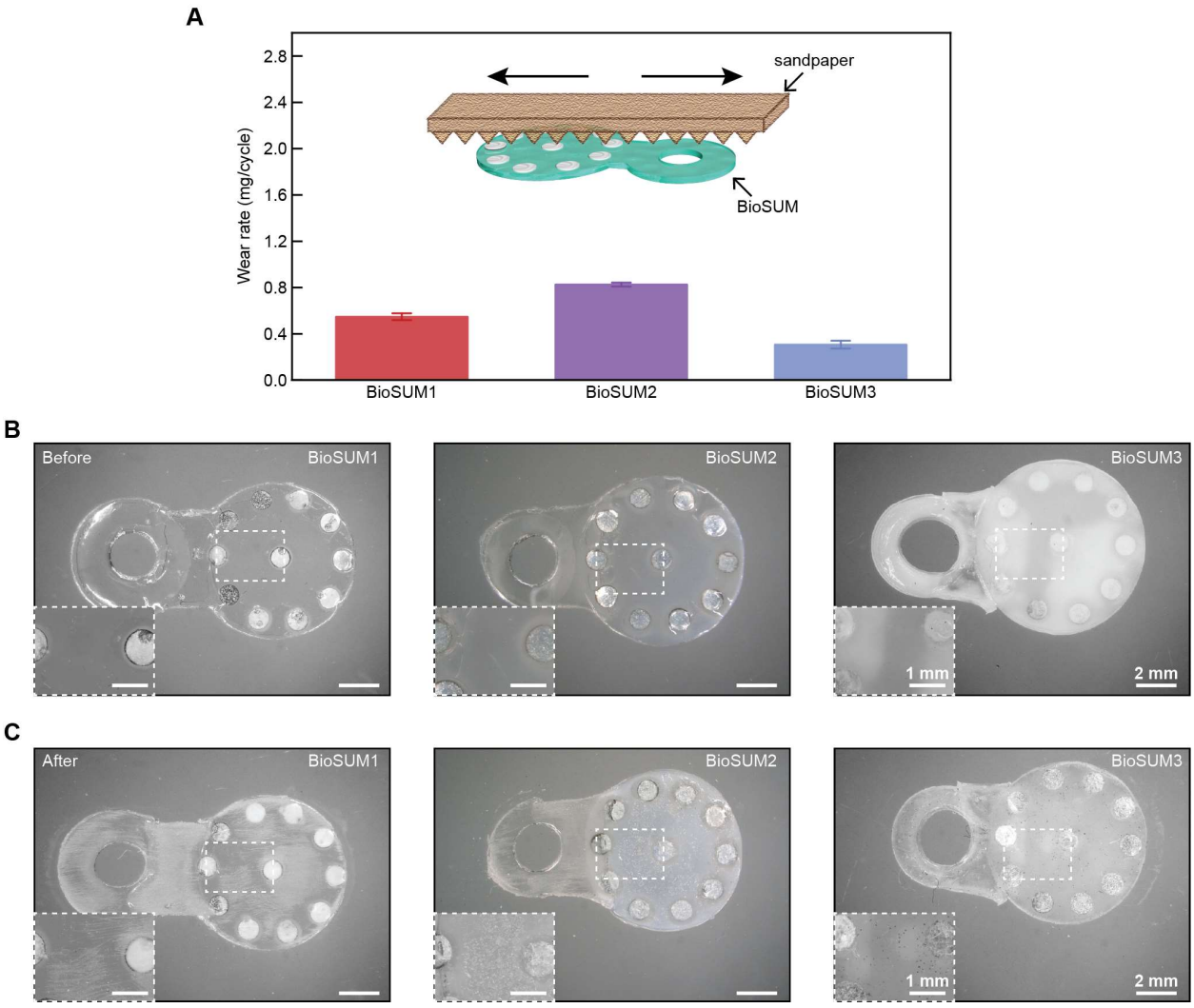

Fig. S20. Wear rates of the hydrogel materials used in BioSUMs. (**A**) Wear rates of the hydrogel materials in BioSUM1, BioSUM2, and BioSUM3. Error bars represent ±SD. (**B**) Images of BioSUMs before the measurement of wear rates. (**C**) Images of BioSUMs after 100 cycles of the wear test.

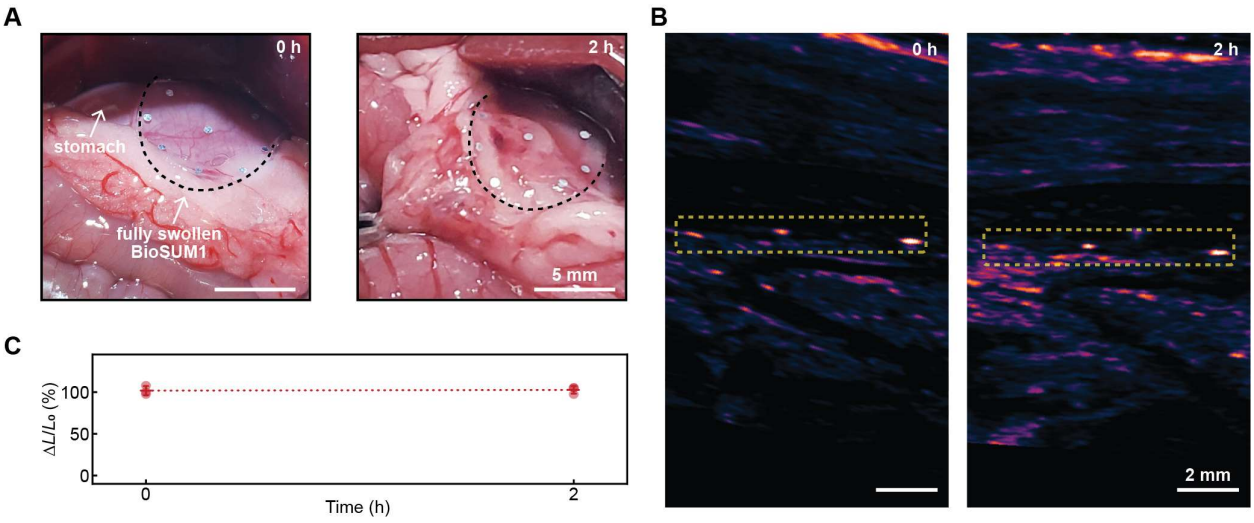

Fig. S21. The performance of BioSUM1 after fully swollen in simulated gastric fluid in a rat model. (**A**) Images of a fully swollen BioSUM1 at the initial stage and after 2 h. (**B**) Ultrasound images of a fully swollen BioSUM1 at the initial stage and after 2 h. (**C**) Summary data showing ultrasonic measurements of swelling ratios at the initial stage and after 2 h. n = 3 biologically independent animals.

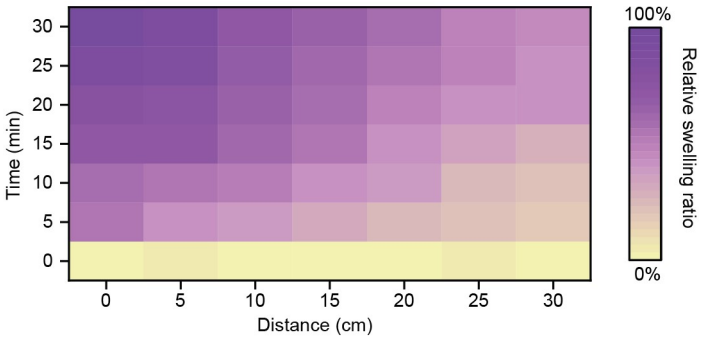

Fig. S22. Spatio-temporal characteristics of BioSUM2 in response to the introduction of simulated intestinal fluid (SIF) at one end of the system.

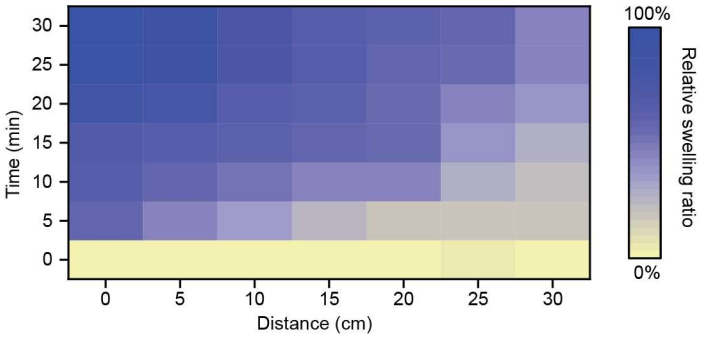

Fig. S23. Spatio-temporal characteristics of BioSUM3 in response to the introduction of simulated pancreatic juice (SPJ) at one end of the system.

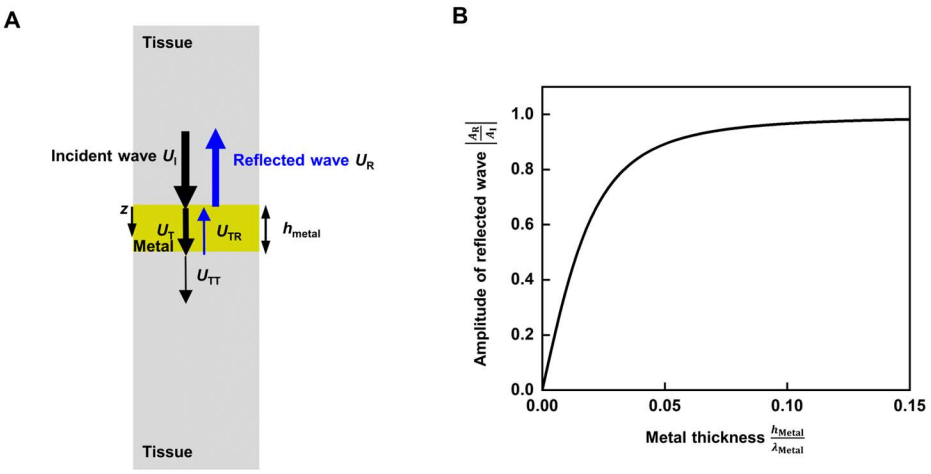

Fig. S24. A theoretical model in one-dimension that illustrates the reflection of acoustic waves at the metal/tissue interface. (**A**) Schematic illustration of the model. (**B**) The relationship between the amplitude of the reflected wave vs. the thickness of the metal.

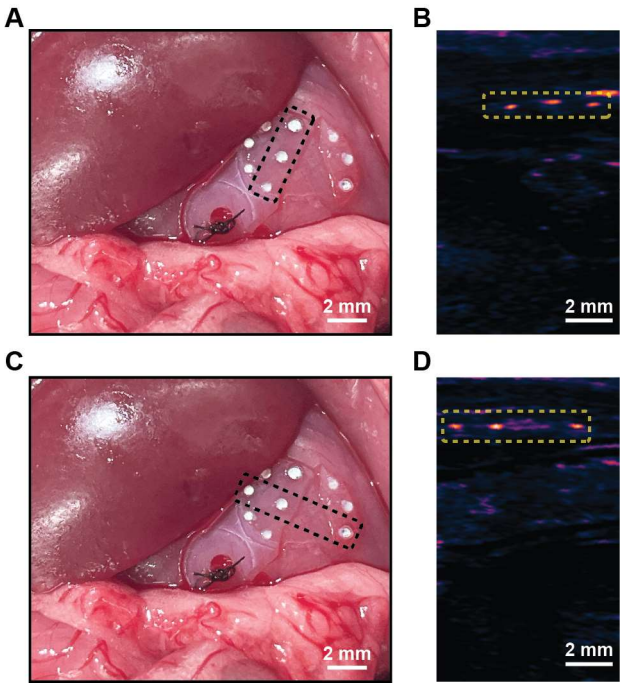

Fig. S25. BioSUM with a manually introduced tear implanted in a rat model. (**A**) Image of a BioSUM1 with a tear. The dashed box indicates the cross-sectional position of acoustic waves used to produce the image in (B). (**B**) Ultrasound image of a BioSUM1 with a tear, where the acoustic waves intersect a diameter of the device without the tear. (**C**) Image of the same BioSUM1 shown in (A). The dashed box indicates the cross-sectional position of acoustic waves used to produce the image in (D). (**D**) Ultrasound image of a BioSUM1 with a tear, where the acoustic waves intersect a diameter of the device with the tear.

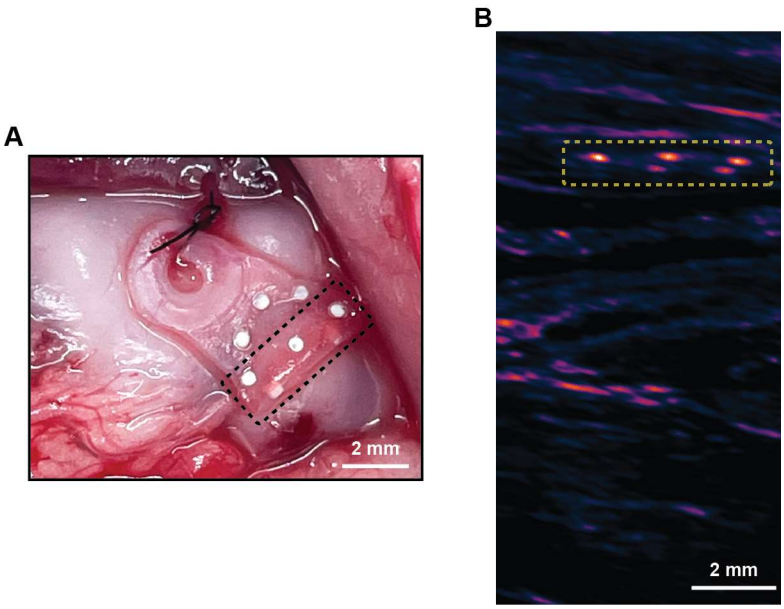

Fig. S26. A folded BioSUM1 in a rat model. (**A**) Image of a folded BioSUM1 on the stomach. The dashed box indicates the cross-sectional position of acoustic waves in (B). (**B**) Ultrasound image of a folded BioSUM1 indicating the signal of five bright segments, different from the normal pattern.

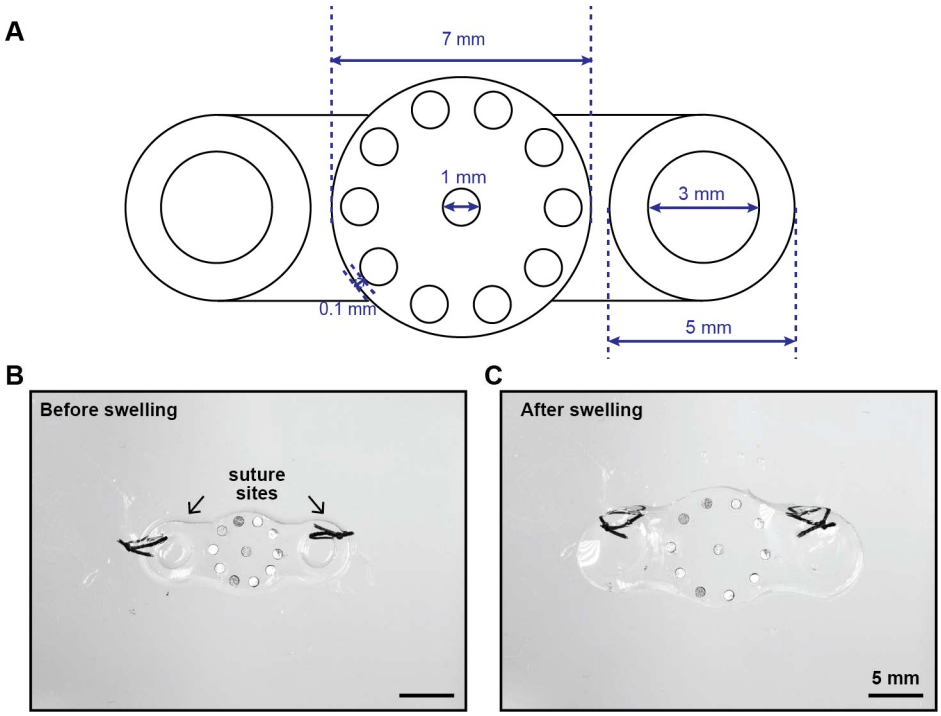

Fig. S27. Alternative design of BioSUMs with two suture rings on opposite sides. (**A**) Alternative design with two suture rings for enhanced mechanical fixation to tissues in the dynamic GI tract. (**B, C**) Images of a BioSUM1 on an elastomeric substrate with two loose sutures through the suture sites. (**B**) Image of a BioSUM1 before swelling. (**C**) Image of a BioSUM1 after free swelling to approximately 40% without constraint due to the existence of a gap between the suture and the ring.

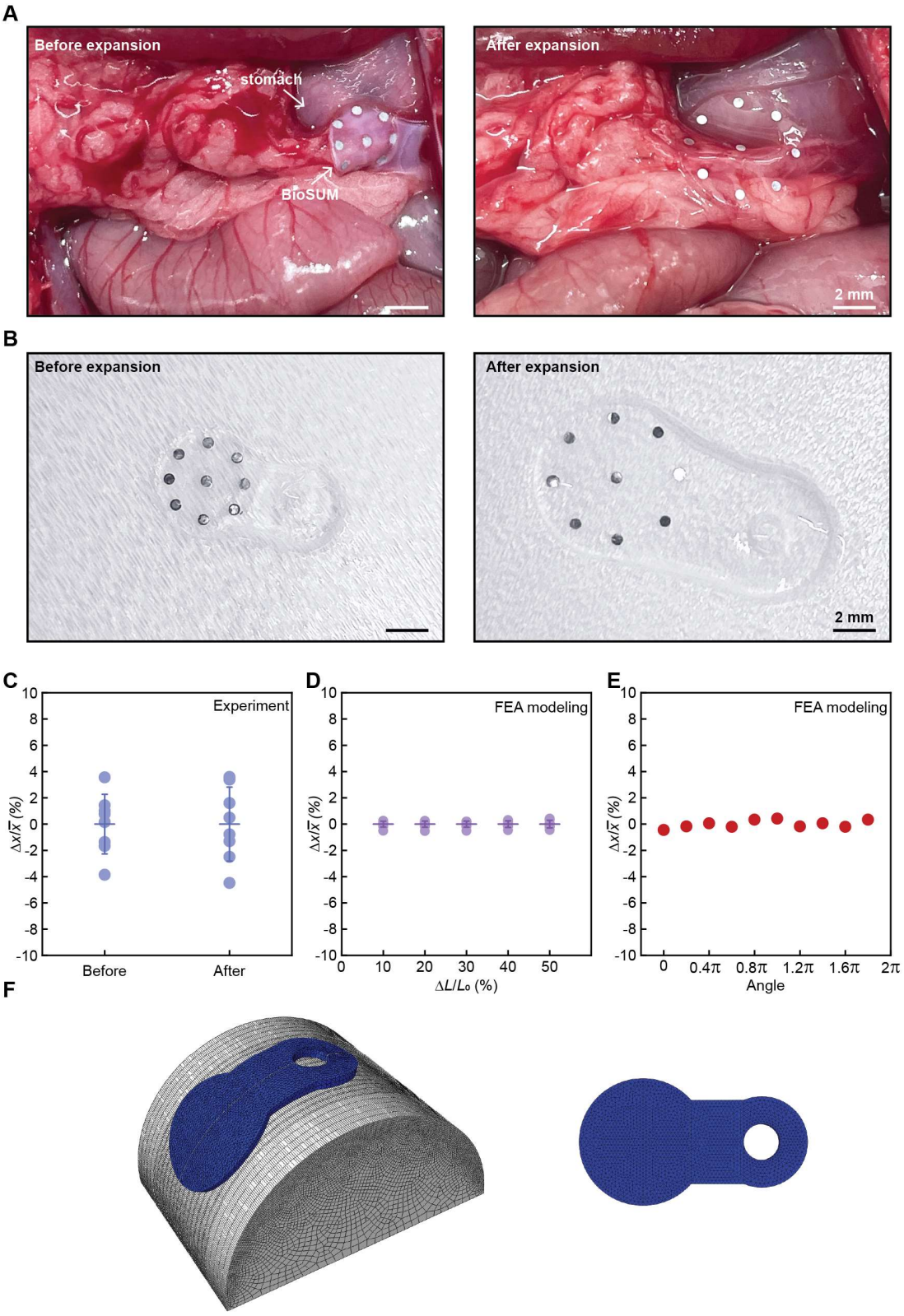

Fig. S28. The expansion of a BioSUM in a curvilinear tissue environment. (**A**) Images of BioSUM1 on a curvilinear surface in a rat model before and after expansion. (**B**) Images of BioSUM1 on a flat substrate before and after expansion on this curvilinear surface, indicating

isotropic expansion under biological conditions. (**C**) Summary results from (A) and (B) showing the deviation of distances between each pair of Zn disks (Zn disk on the perimeter and Zn disk in the center). $\Delta x/\bar{x}$ (%) denotes the percentage of deviation between the measured distance and the average distance. Dots represent the distance between each pair of Zn disks. Error bars represent ±SD. (**D**) FEA modeling results showing the deviation of distances between each pair of Zn at different swelling ratios. $\Delta L/L_0$ (%) denotes the swelling ratio. Dots represent the distance between each pair of Zn disks. Error bars represent ±SD. (**E**) FEA modeling results demonstrating the deviation of distances between each pair of Zn disks at different circular angles. The swelling ratio of BioSUM is 50%. (**F**) FEA modeling results for a BioSUM on a column with a diameter of 2.5 cm (left) and in a flattened state (right) indicating isotropic expansion. The swelling ratio of the BioSUM is 50%.

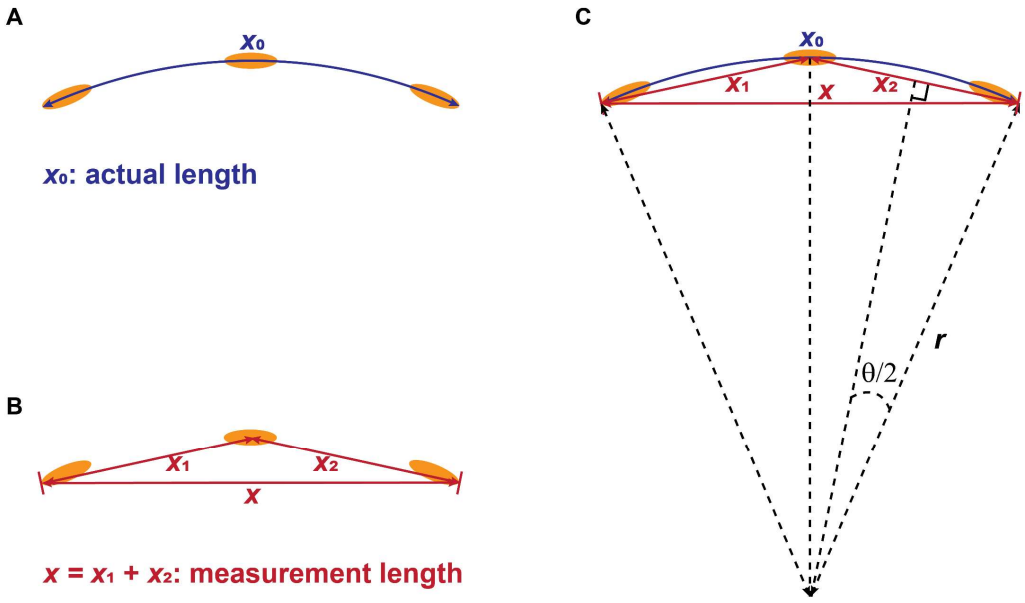

Fig. S29. Schematic illustrations of ultrasonic measurements from a bent device. (**A**) The actual length x_0. (**B**) The ultrasonic measurement length x. (**C**) Schematic illustration with auxiliary lines for calculating the deviation between x_0 and x.

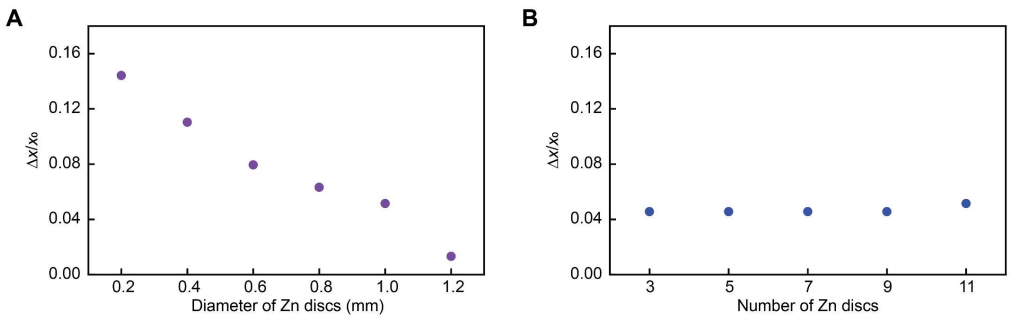

Fig. S30. Numerical simulation results for the effects of different parameters on the measurement accuracy at 10 cm depth and a frequency of 5 MHz. (**A**) Effect of the diameter of Zn disks. (**B**) Effect of the number of Zn disks (including Zn disk at the center). $\Delta x/x_0$ is the deviation of the measured length divided by the actual length.

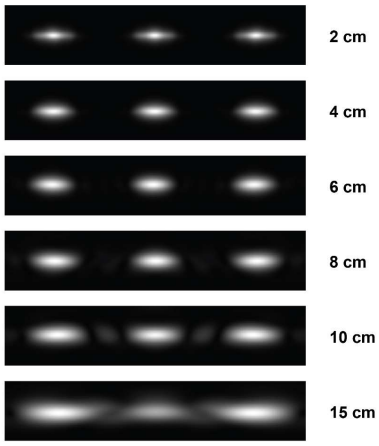

Fig. S31. Numerical simulation results for ultrasound B-mode images at different depths for a frequency of 5 MHz.

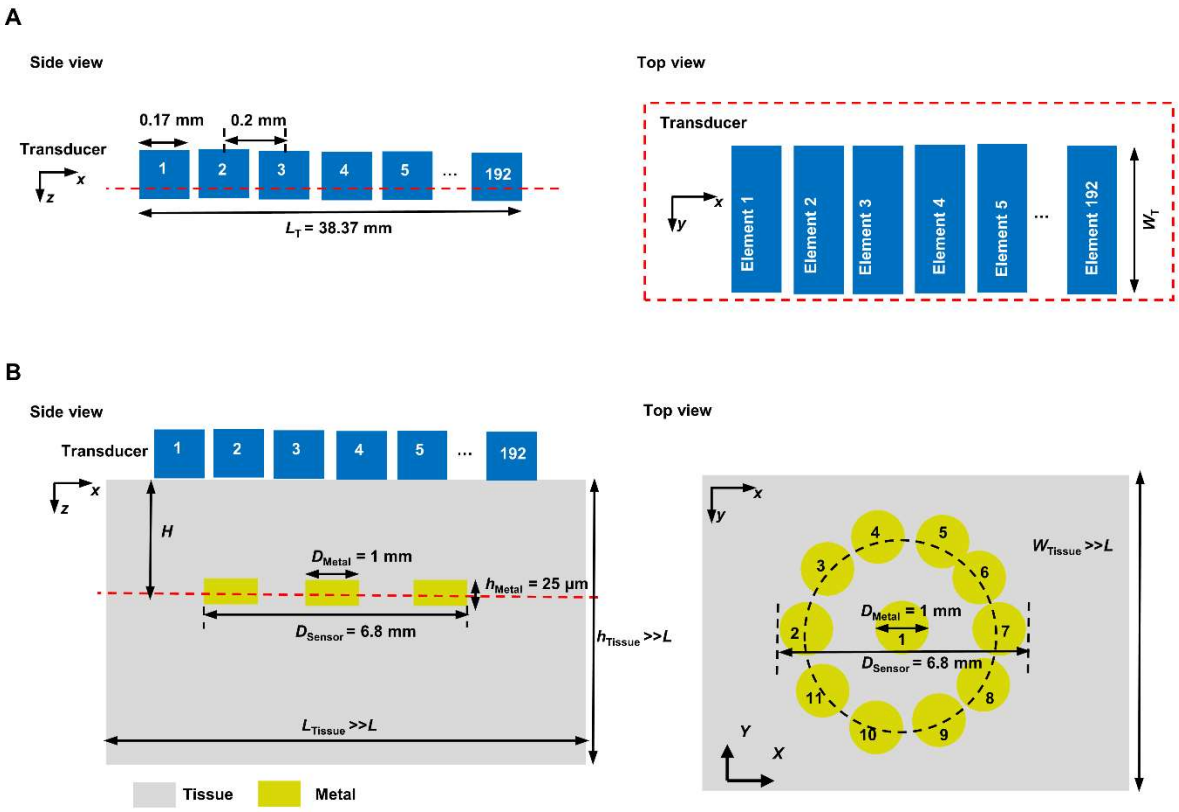

Fig. S32. Schematic illustration of the simulation model for ultrasound. (**A**) The transducer. (**B**) The tissue with an embedded device.

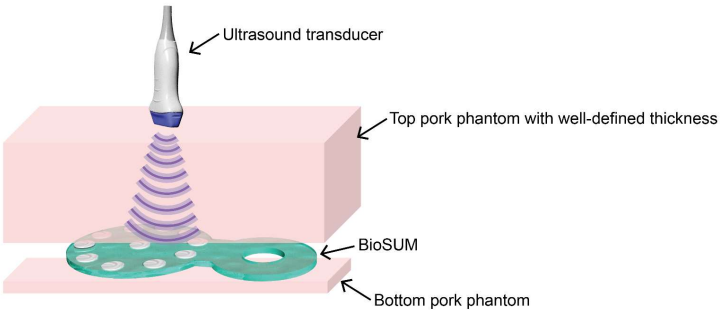

Fig. S33. Schematic illustration of the experimental setup for ultrasonic characterization of measurement accuracy and signal-to-noise ratio (SNR) using pork phantoms.

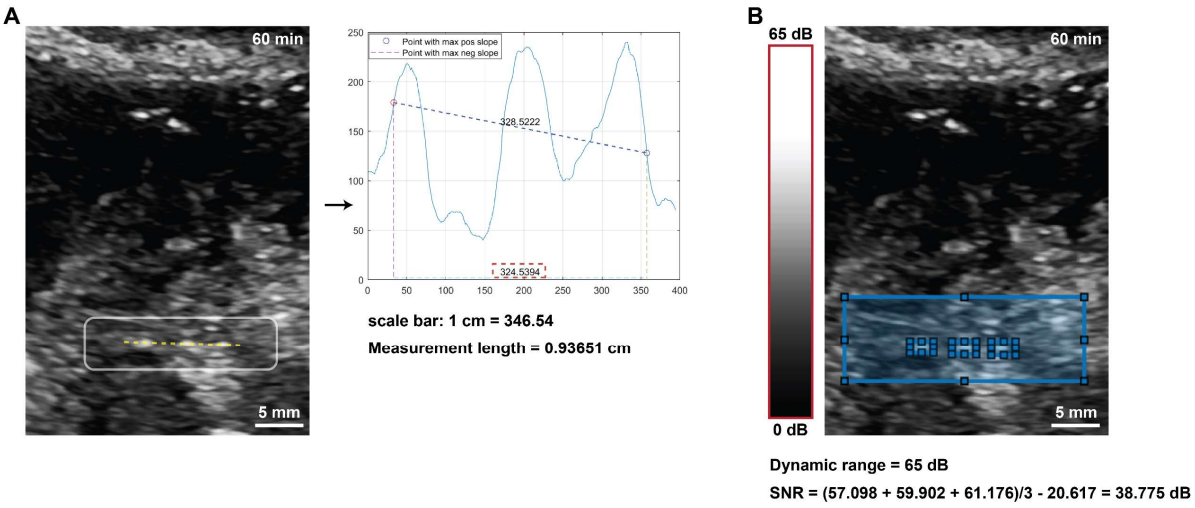

Fig. S34. Examples of length measurements and characterization of SNR values by MATLAB coding using the ultrasound image from pancreatic leakage at 60 min in a porcine model. (**A**) Measurement of length. (**B**) Characterization of SNR.

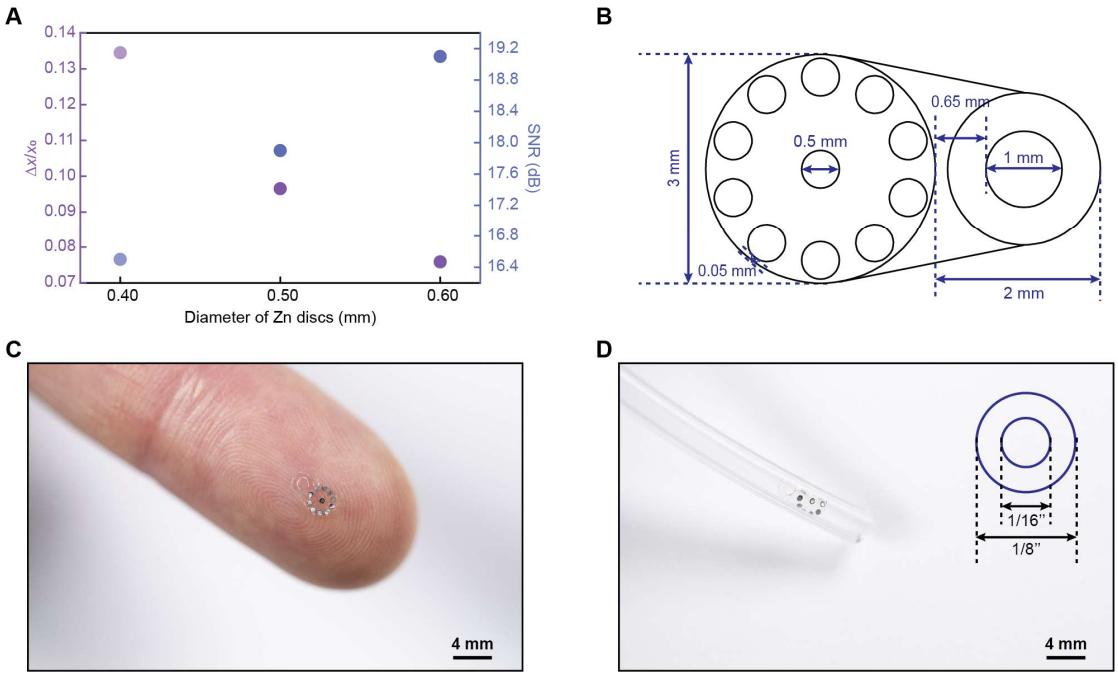

Fig. S35. Ultraminiaturized design guided by numerical simulation for operation at depths of up to 10 cm. (**A**) Numerical simulation results for the measurement accuracy and SNR as a function of the diameter of Zn disks. A hydrogel with a diameter of 3 mm is used. For hydrogels with diameters of less than 3 mm, measurement accuracy and SNR values cannot meet the requirements of $\Delta x/x_0 < 0.1$ and SNR > 18 dB, respectively. The frequency of the ultrasonic waves is 8 MHz. (**B**) Device design. (**C**) Image of a device on the finger. (**D**) Image of a slightly bent device in a plastic tube with I.D. = 1/16 inch, O.D. = 1/8 inch.

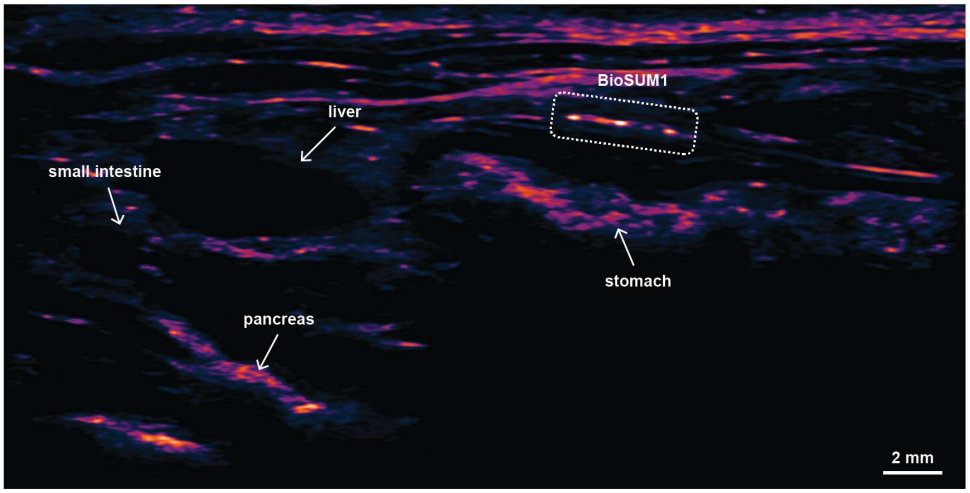

Fig. S36. Ultrasound B-mode image of BioSUM1 on the stomach in a rat model. The labels identify the representative organs in the GI tract.

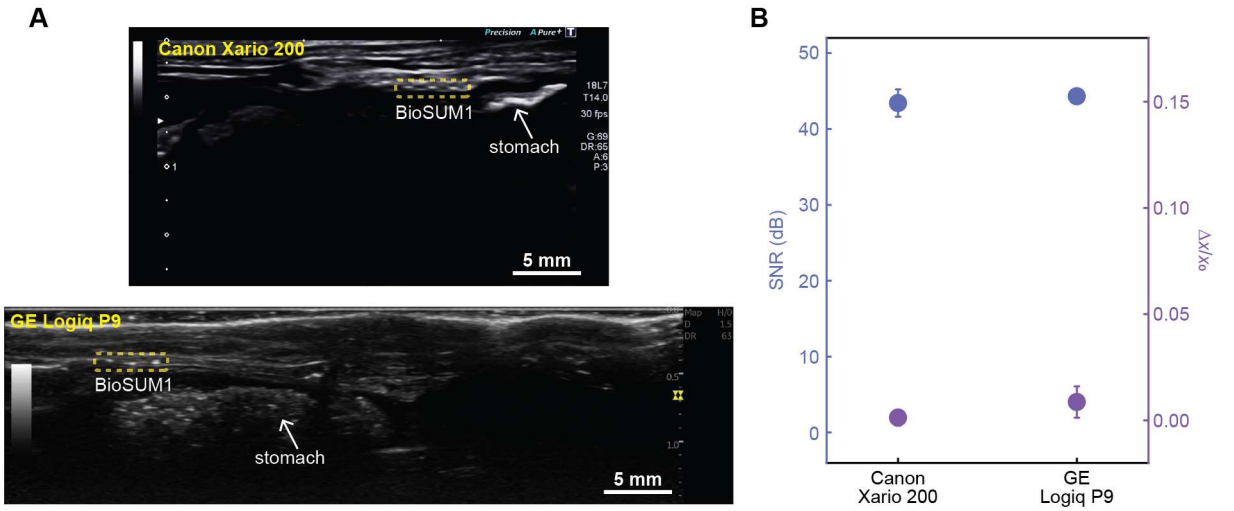

Fig. S37. Detection of BioSUM using two different ultrasound imaging systems. (**A**) Ultrasound B-mode images of BioSUM1 on the stomach in a rat model using a Canon Xario 200 system with 18L7 transducer (top) and a GE Logiq P9 system with ML6-15 transducer (bottom). (**B**) Comparison of the signal quality from the two ultrasound imaging systems. $\Delta x/x_0$ is the deviation of measured length divided by the actual length.

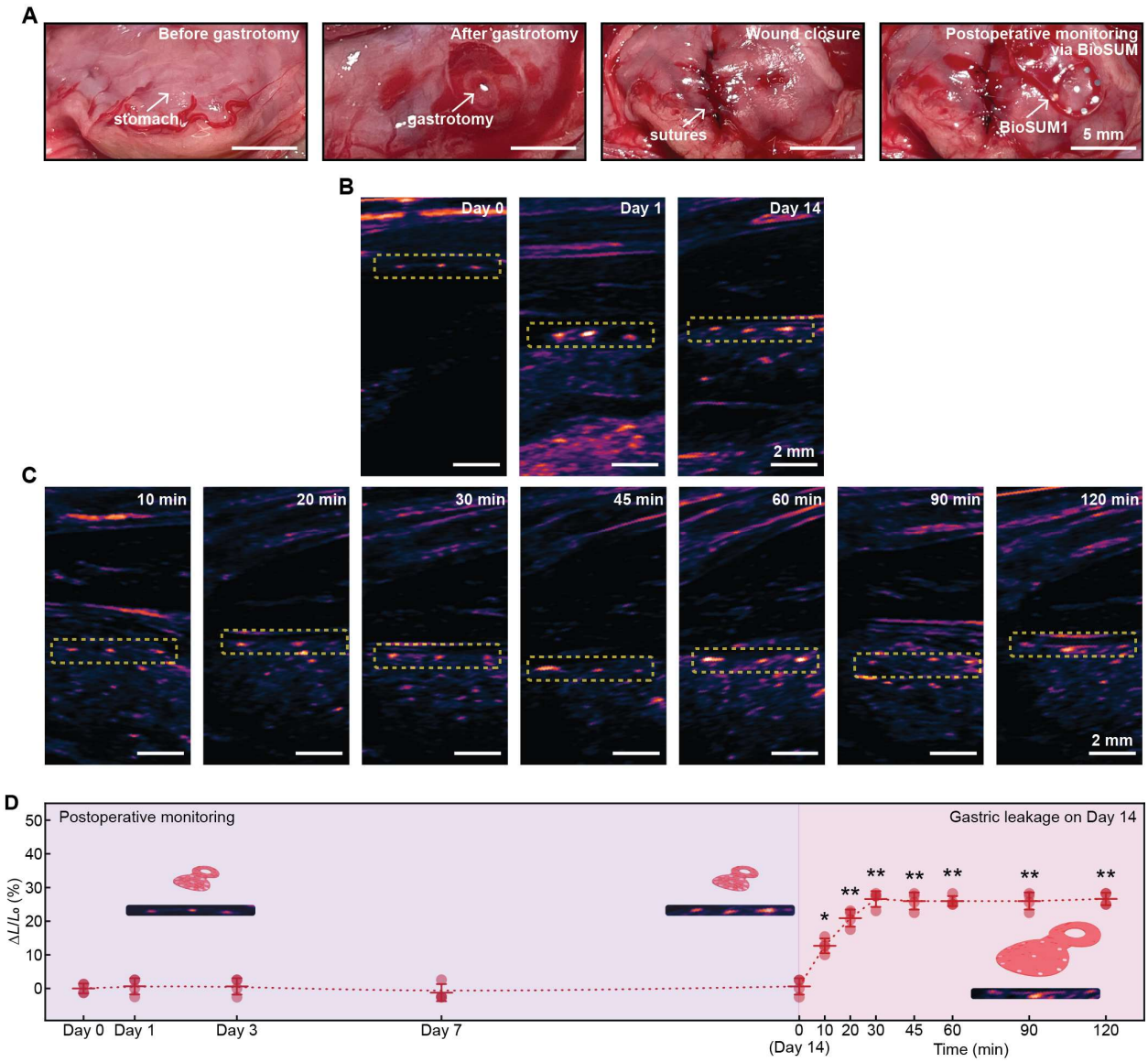

Fig. S38. Longitudinal monitoring of pH homeostasis in a rat model after a properly performed GI surgery. (**A**) Images showing the procedures associated with a properly performed GI surgery (gastrotomy) and postoperative monitoring via a BioSUM1. The wound closure procedure after the gastrotomy involves a simple interrupted suture on the first layer, followed by a continuous lambert pattern on the second layer to invert the tissue. (**B**) Ultrasound images of the BioSUM1 on the stomach over a 14-day period after the GI surgery. The depth of the array of Zn disks changes between day 0 and day 1 due to postoperative relocation of the organs. (**C**) Longitudinal ultrasound images of the BioSUM1 on the stomach following a separate gastrotomy. (**D**) Summary data showing the swelling ratios of the BioSUM1 over the 14-day period after the GI surgery and following a separate gastrotomy on day 14. n = 4 biologically independent animals. RM One-Way ANOVA, $p < 0.0001$, Holm-Sidak's multiple comparison test vs Day 14 (0 min), 10 min, $p = 0.0255$, 20 min, $p = 0.0069$, 30 min, $p = 0.0016$, 45 min, $p = 0.0051$, 60 min, $p = 0.0033$, 90 min, $p = 0.0051$, 120 min, $p = 0.0047$. Inset ultrasound images representing day 1, day 14 and 120 min are extracted from (B) and (C).

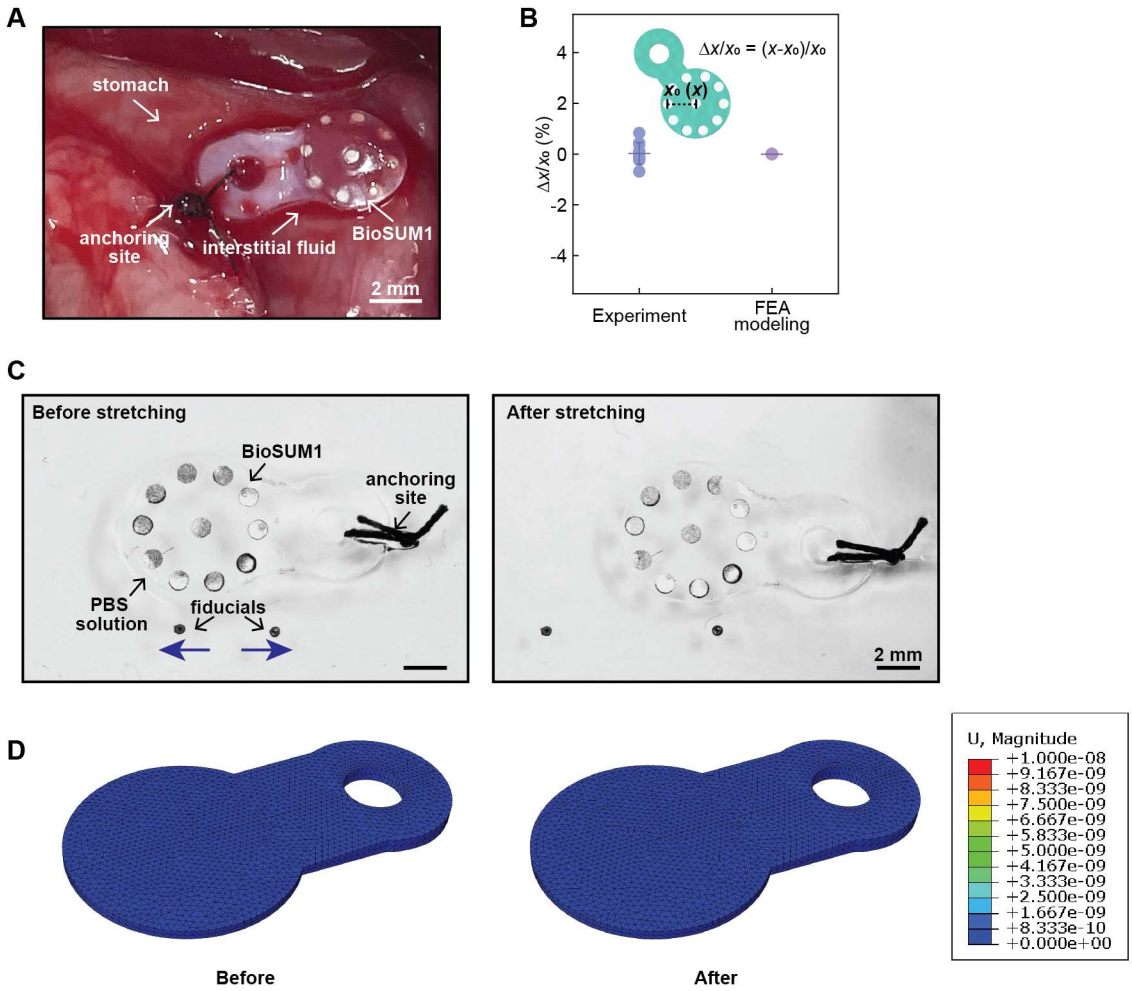

Fig. S39. Experimental and numerical simulations of the effects of mechanical deformation of organs adjacent to the device on the length measurement. (**A**) Image of BioSUM1 on the stomach in a rat showing the interstitial fluid that exists between the devices and the tissue. (**B**) Experimental and FEA modeling results showing the effect of mechanical deformation on the length measurement. x_0 denotes the measured distance between each pair of Zn disks (Zn disk on the perimeter and Zn disk in the center) before mechanical deformation. x denotes the measured distance after mechanical deformation. Dots represent individual measurement. Error bars represent ±SD. (**C**) Images of BioSUM1 on an elastomeric substrate with the presence of PBS solution at the interface. A pair of fiducials on the elastomeric substrate indicates a stretching ratio of ~ 60%. (**D**) Images from FEA modeling before and after the mechanical deformation of the substrate indicating minimal effect on the device. U denotes displacement.

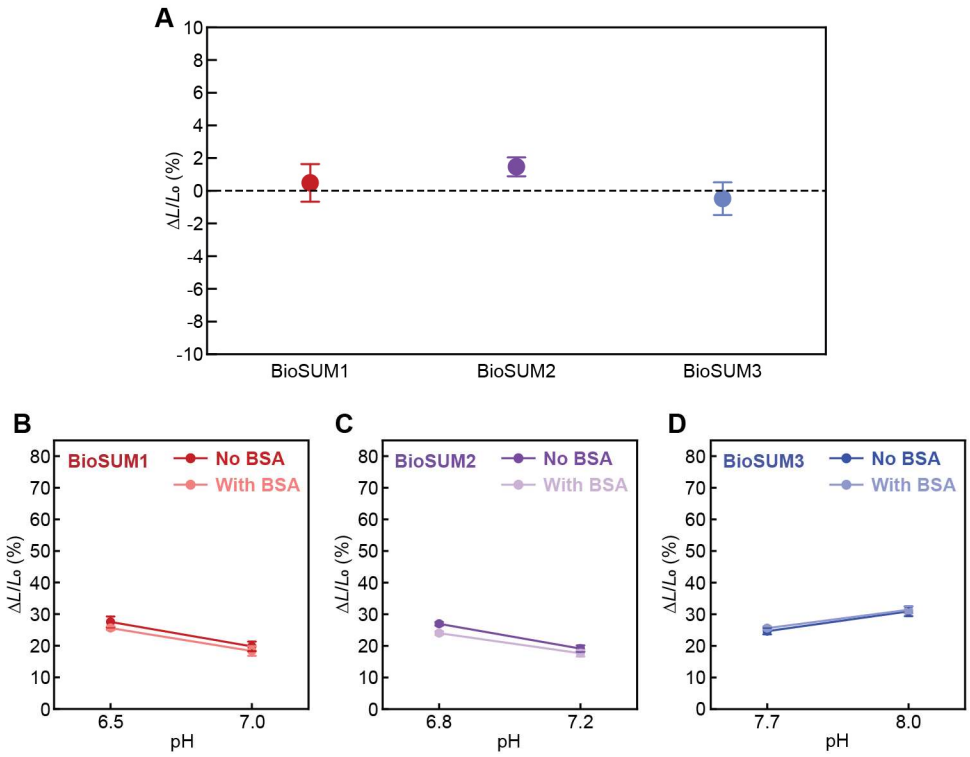

Fig. S40. Effect of protein (bovine serum albumin, BSA) on pH-responsive behaviors of BioSUMs. (**A**) Summary data showing minimal fluctuations in dimensions after immersion in PBS solution with 1 wt% BSA (pH = 7.4) at 37 °C for 2 weeks. BioSUMs were fully swollen in PBS for 24 h before the test. (**B-D**) pH-responses of BioSUMs at the equilibrium state after immersion in PBS solution with 1 wt% BSA at 37 °C for 2 weeks. pH buffer solutions with 1 wt% BSA were used for characterizing pH-responses. (**B**) BioSUM1. (**C**) BioSUM2. (**D**) BioSUM3. $\Delta L/L_0$ (%) denotes the swelling ratio. Measurements only involve narrow pH ranges to avoid the denaturation of the BSA.

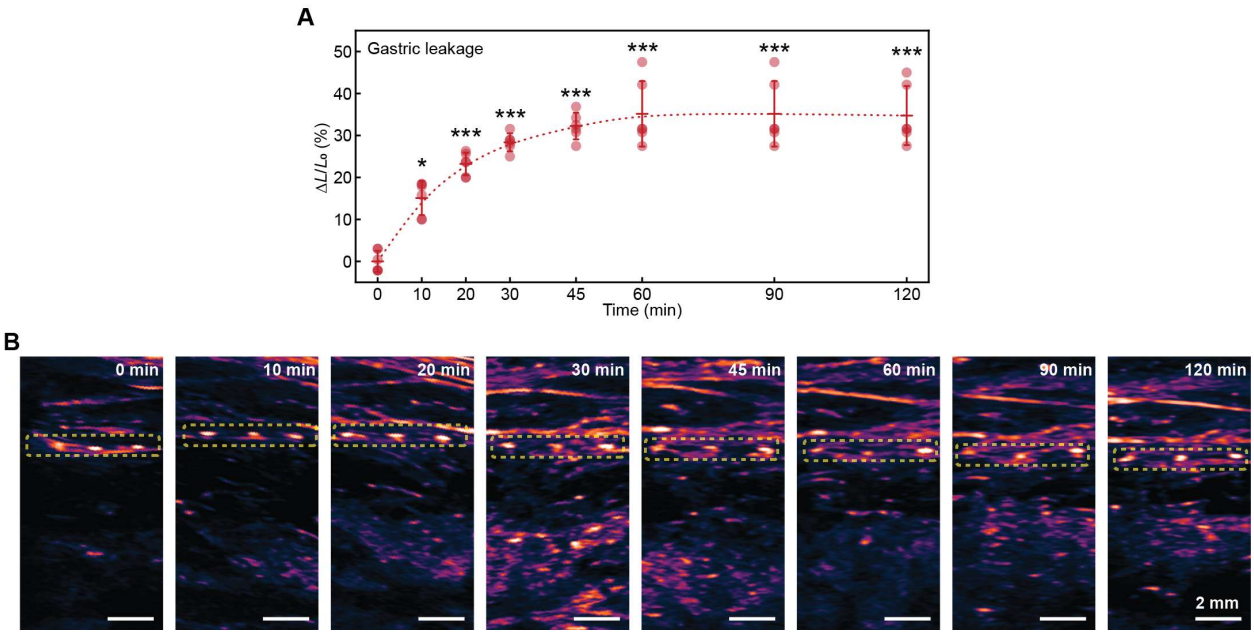

Fig. S41. The performance of BioSUM1 for detection of gastric leakage in a rat model without the 14-day stabilization period. (**A**) Swelling ratios of BioSUM1 following gastrotomy. n = 6 biologically independent animals. RM One-Way ANOVA, $p < 0.0001$, Sidak's multiple comparison test vs 0 min, 10 min, $p = 0.0152$, 20 min, $p = 0.0006$, 30 min, $p = 0.0001$, 45 min, $p = 0.0002$, 60 min, $p = 0.0008$, 90 min, $p = 0.0008$, 120 min, $p = 0.0006$. Dots represent individual animals. Line represents B-spline. Error bars represent ±SD. *$p < 0.05$, **$p < 0.01$, ***$p < 0.001$, ****$p < 0.0001$. (**B**) Images after gastrotomy.

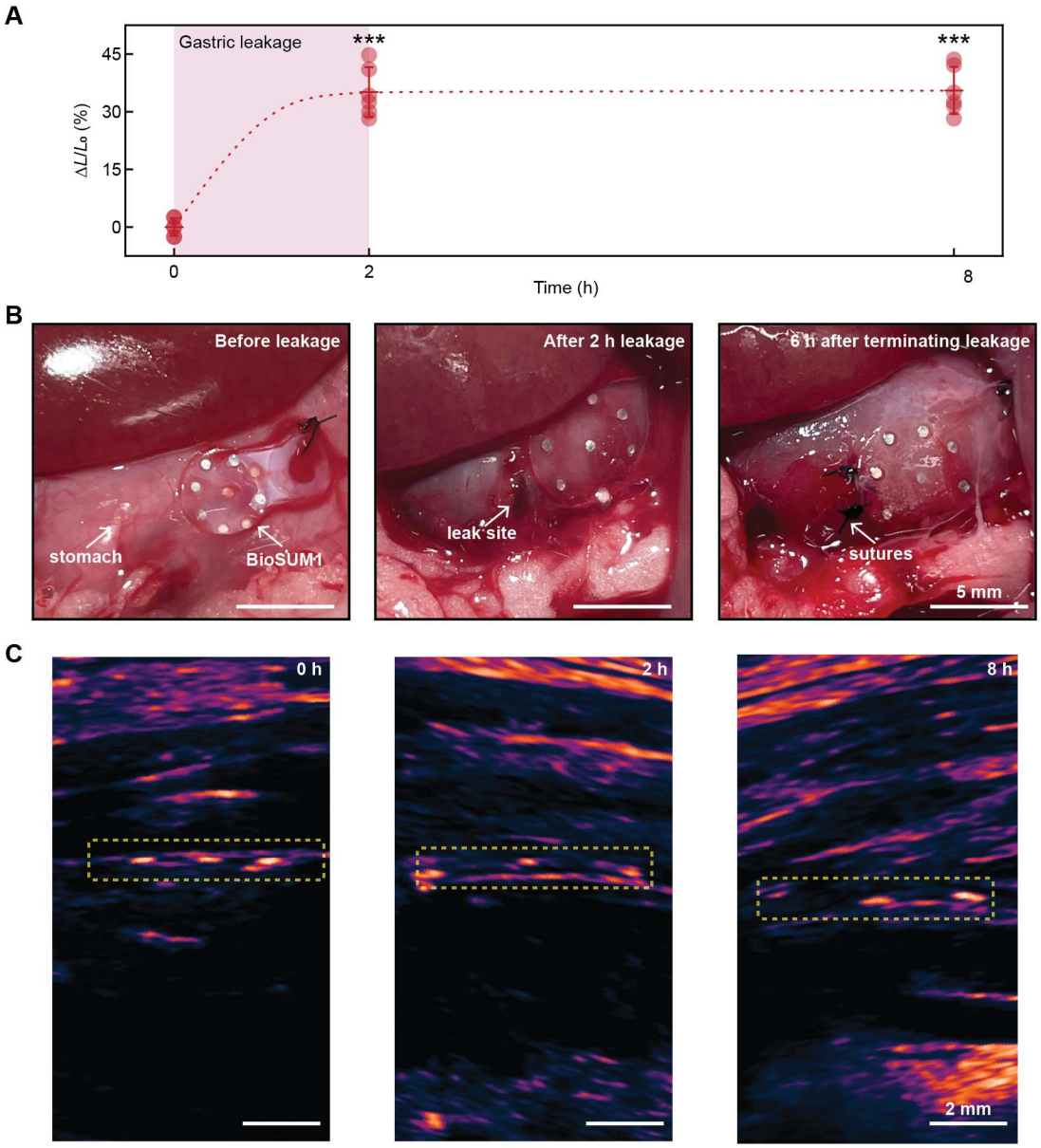

Fig. S42. The performance of BioSUM1 during gastric leakage and after the termination of leakage in a rat model. (**A**) Summary data showing the swelling ratios of BioSUM1 following gastrotomy for 2 h and the stabilized swelling ratios 6 h after termination of leakage. n = 6 biologically independent animals. RM One-Way ANOVA, $p < 0.0001$, Sidak's multiple comparison test vs 0 h, 2 h, $p = 0.0002$, 8 h, $p = 0.0001$. Dots represent individual animals. Line represents B-spline. Error bars represent ±SD. *$p < 0.05$, **$p < 0.01$, ***$p < 0.001$, ****$p < 0.0001$. (**B**) Images of BioSUM1 at the initial stage, 2 h following gastrotomy, and 6 h after termination of leakage. (**C**) Ultrasound images of BioSUM1 at the initial stage, 2 h following gastrotomy, and 6 h after termination of leakage.

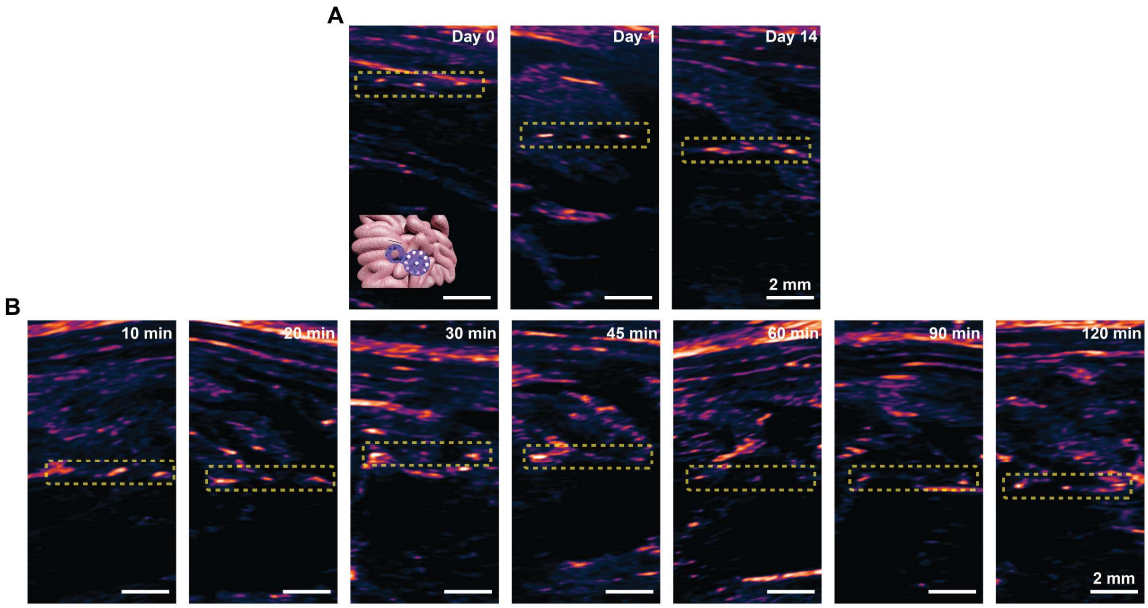

Fig. S43. Ultrasound images of BioSUM2 before and immediately after small intestine leakage in a rat model. (**A**) Ultrasound images of BioSUM2 on the small intestine over a 14-day period prior to small intestinal leakage. The depth of the device changed between day 0 and day 1 due to postoperative relocation of organs. (**B**) Images following enterotomy.

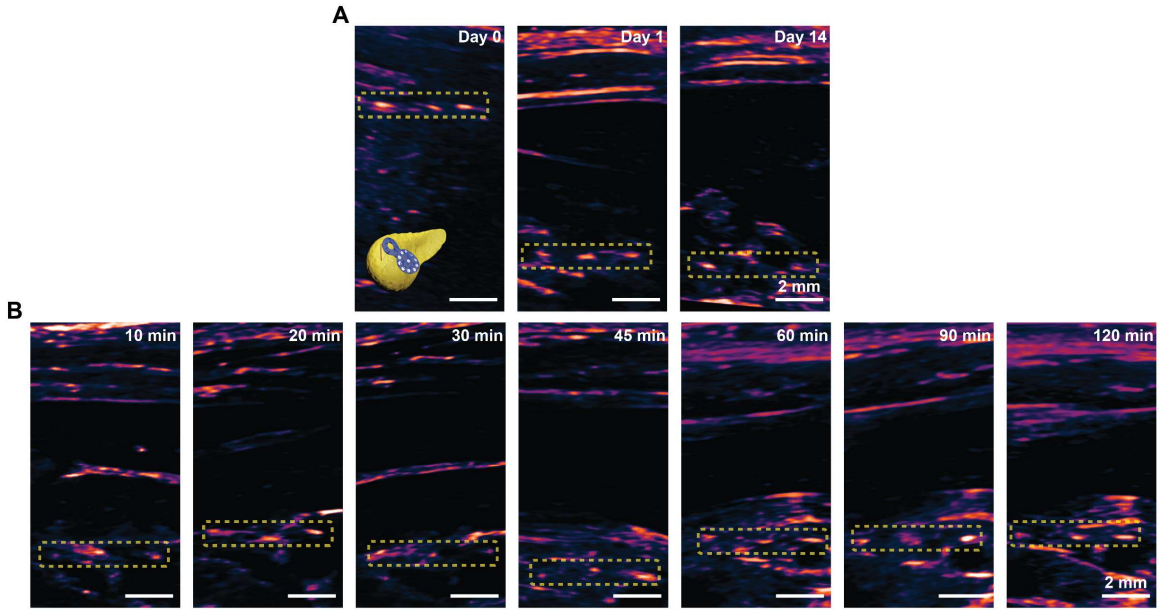

Fig. S44. Ultrasound images of BioSUM3 before and immediately after pancreatic leakage in a rat model. (**A**) Ultrasound images of BioSUM3 on the pancreas over a 14-day period prior to pancreatic leakage. The depth of the device changed between day 0 and day 1 due to postoperative relocation of organs. (**B**) Images following pancreatic leakage.

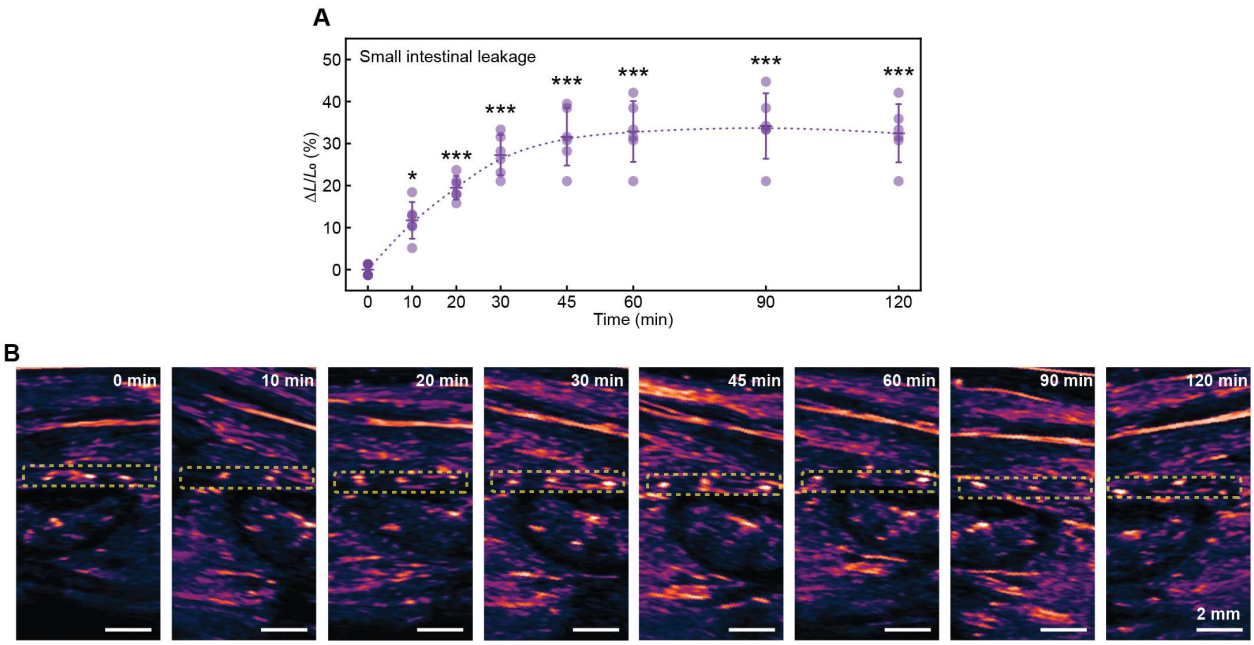

Fig. S45. The performance of BioSUM2 for detection of small intestinal leakage in a rat model without the 14-day stabilization period. (**A**) Swelling ratios of BioSUM2 following enterotomy. n = 6 biologically independent animals. RM One-Way ANOVA, $p < 0.0001$, Sidak's multiple comparison test vs 0 min, 10 min, $p = 0.0205$, 20 min, $p = 0.0003$, 30 min, $p = 0.0002$, 45 min, $p = 0.0006$, 60 min, $p = 0.0007$, 90 min, $p = 0.0008$, 120 min, $p = 0.0006$. Dots represent individual animals. Line represents B-spline. Error bars represent ±SD. *$p < 0.05$, **$p < 0.01$, ***$p < 0.001$, ****$p < 0.0001$. (**B**) Images after enterotomy.

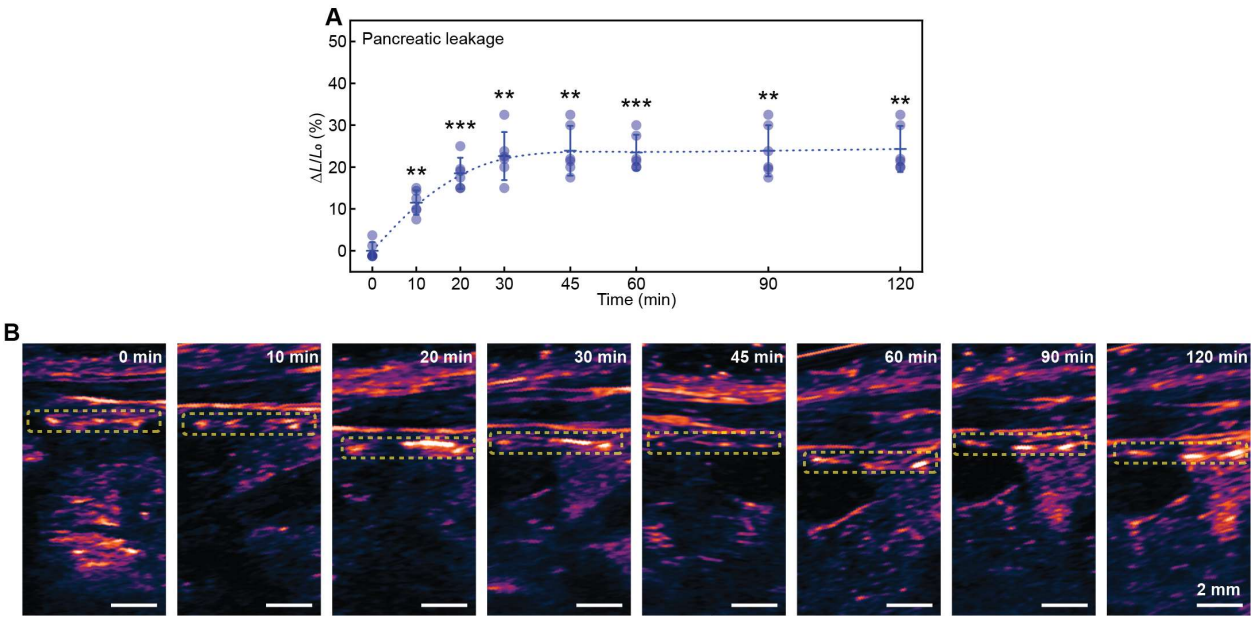

Fig. S46. The performance of BioSUM3 for detection of pancreatic leakage in a rat model without the 14-day stabilization period. (**A**) Swelling ratios of BioSUM3 following pancreatic leakage. n = 6 biologically independent animals. RM One-Way ANOVA, $p < 0.0001$, Sidak's multiple comparison test vs 0 min, 10 min, $p = 0.0016$, 20 min, $p = 0.0007$, 30 min, $p = 0.0017$, 45 min, $p = 0.0025$, 60 min, $p = 0.0008$, 90 min, $p = 0.0024$, 120 min, $p = 0.0018$. Dots represent individual animals. Line represents B-spline. Error bars represent ±SD. *$p < 0.05$, **$p < 0.01$, ***$p < 0.001$, ****$p < 0.0001$. (**B**) Images after leakage.

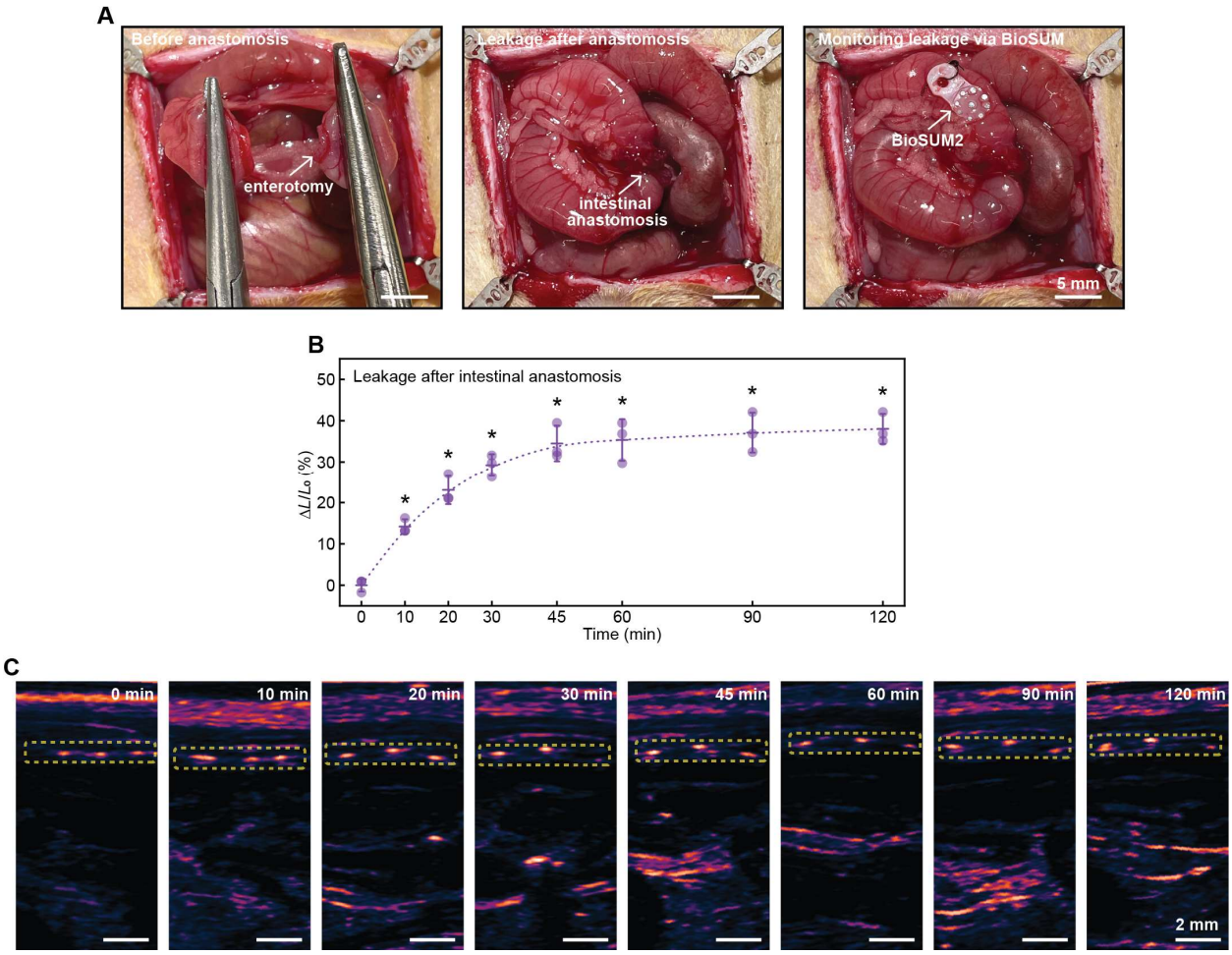

Fig. S47. Monitoring small intestinal leakage via a BioSUM2 following a poorly performed intestinal anastomosis. (**A**) Images showing the procedures of a poorly performed intestinal anastomosis that introduces leakage. The surgical procedure starts with an enterotomy by disconnecting the intestine in the middle, followed by holding the two halves of the intestine with a flat hemostat. A poorly performed simple continuous suture of the joint induces small intestinal leakage. (**B**) Swelling ratios of the BioSUM2 following the poorly performed intestinal anastomosis. n = 3 biologically independent animals. RM One-Way ANOVA, p = 0.0072, Holm-Sidak's multiple comparison test vs 0 min, 10 min, p = 0.0302, 20 min, p = 0.0302, 30 min, p = 0.0191, 45 min, p = 0.0191, 60 min, p = 0.0191, 90 min, p = 0.0191, 120 min, p = 0.0126. Dots represent individual animals. Line represents B-spline. Error bars represent ±SD. *p < 0.05, **p < 0.01, ***p < 0.001, ****p < 0.0001. (**C**) Ultrasound images of the BioSUM2 on the small intestine after intestinal anastomosis.

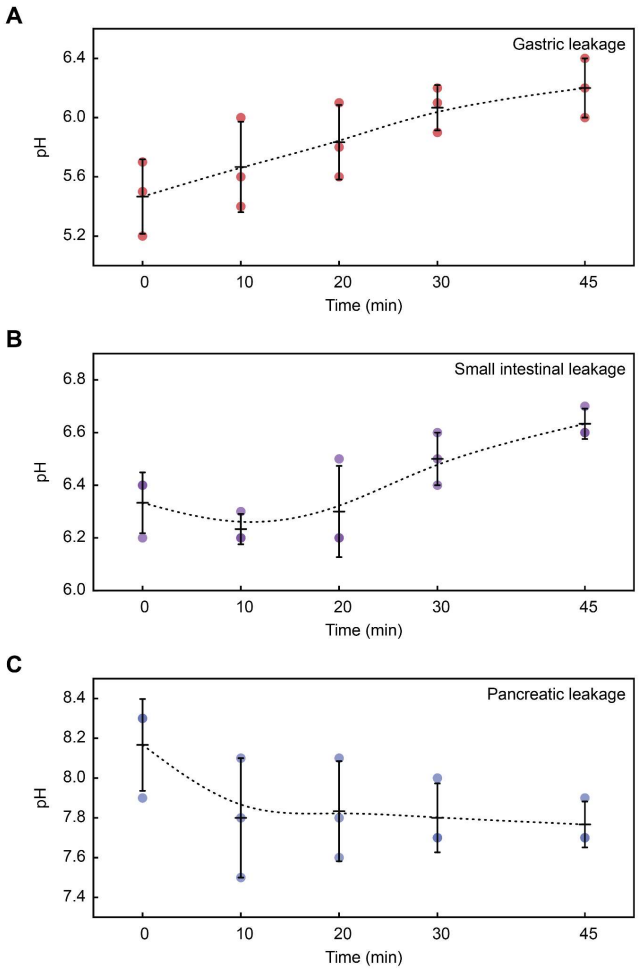

Fig. S48. Real-time pH dynamics of the local environment associated with leaks in a rat model after a 14-day stabilization period. (**A**) Gastric leakage. (**B**) Small intestinal leakage. (**C**) Pancreatic leakage.

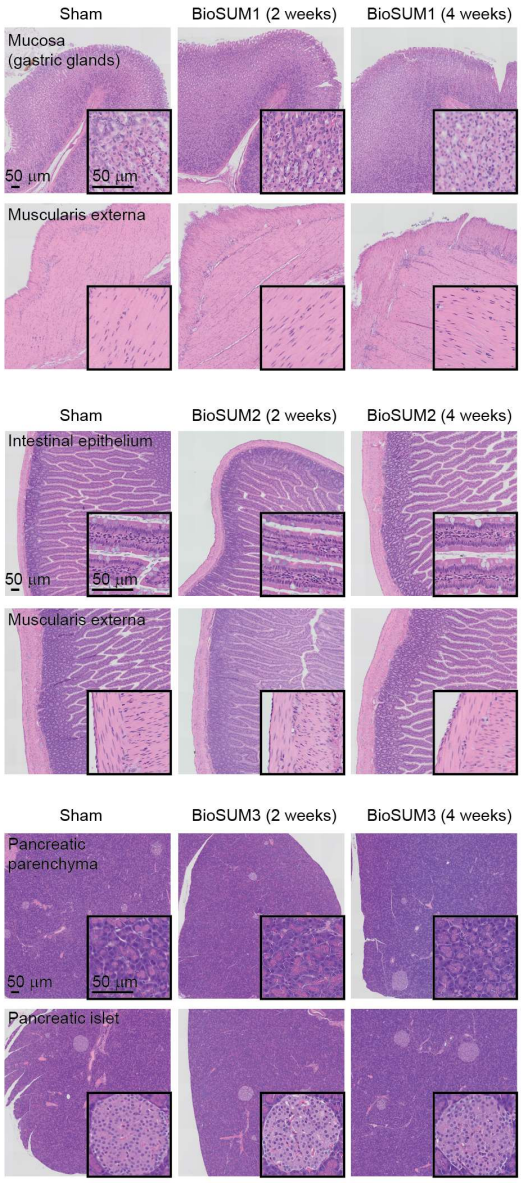

Fig. S49. Histology images of GI organs of sham controls and rats with BioSUMs implanted for 2 and 4 weeks.

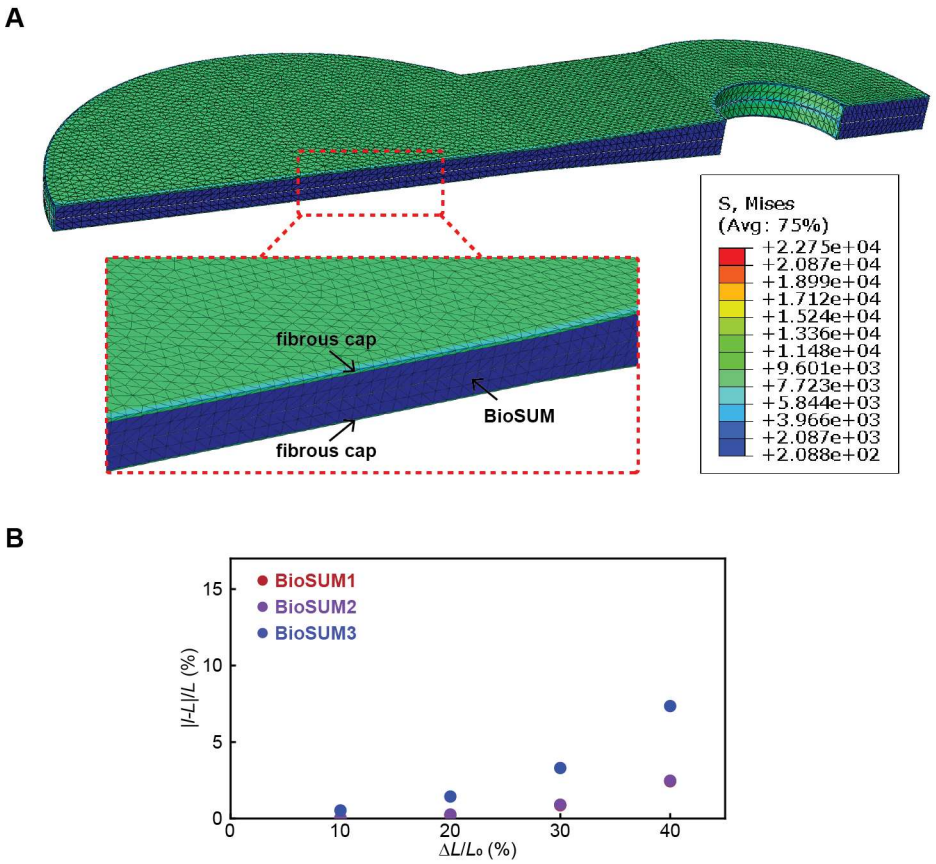

Fig. S50. FEA modeling results for the swelling performance of a BioSUM in a fibrous cap. (**A**) Image of a BioSUM3 in a fibrous cap. The fibrous cap has a Young's modulus of 20 kPa and a thickness of 25 μm. *S* denotes von Mises stress. (**B**) Summary results showing minimal effect of the fibrous cap on the swelling ratio. $\Delta L/L_0$ (%) denotes the swelling ratio without the fibrous cap. *L* denotes the measured distance between Zn disks under the free swelling condition. *l* denotes the measured distance during the swelling procedure with the presence of a fibrous cap.

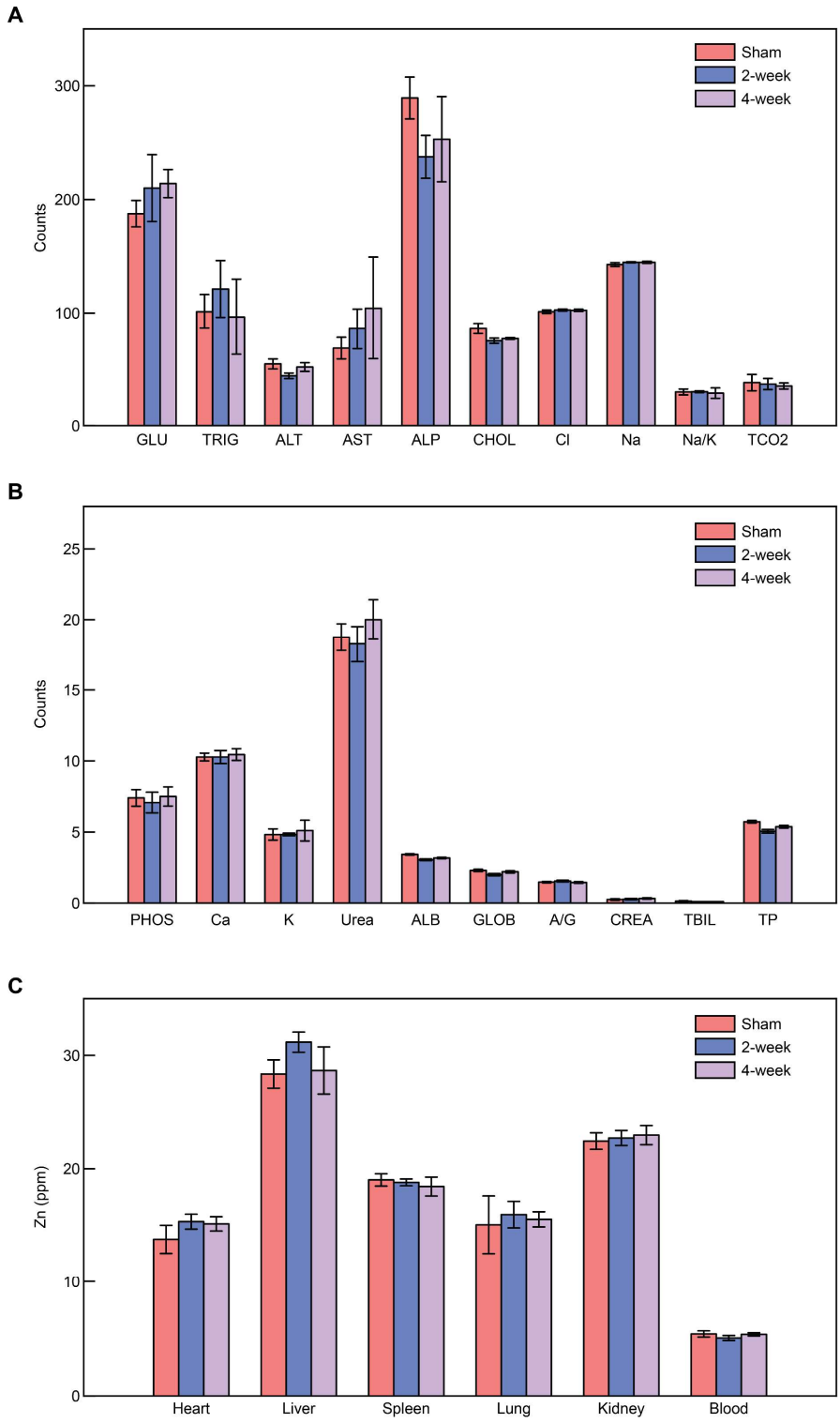

Fig. S51. In vivo biocompatibility and toxicity studies. (**A**) Analysis of blood chemistry. n = 4 biologically independent animals. GLU, glucose (mg/dL); TRIG, triglycerides (mg/dL); ALT alanine aminotransferase (U/L); AST, aspartate transaminase (U/L); ALP, alkaline phosphatase (U/L); CHOL, cholesterol (mg/dL); Cl, chloride (mmol/L); Na, sodium (mmol/L); Na/K,

sodium/potassium ratio; TCO2, bicarbonate (mmol/L). Two-way ANOVA, Holm-Sidak's multiple comparison test with Sham group, $p > 0.05$ for all experimental groups except for GLU 4-week, AST 4-week and ALP. (**B**) Analysis of blood chemistry. n = 4 biologically independent animals. PHOS, phosphorus (mg/dL); Cal, calcium (mg/dL); K, potassium (mmol/L); Urea, blood urea nitrogen (mg/dL); ALB, albumin (g/dL); GLOB, globulin (g/dL); A/G, albumin/globulin ratio; CREA, creatinine (mg/dL); TBIL, total bilirubin (mg/dL); TP, total protein (g/dL). Two-way ANOVA, Holm-Sidak's multiple comparison test with sham group, $p > 0.05$ for all experimental groups. (**C**) Element analysis of the biodistribution of Zn. n = 4 biologically independent animals. Two-way ANOVA, Holm-Sidak's multiple comparison test with the sham group, $p > 0.05$ for all experimental groups.

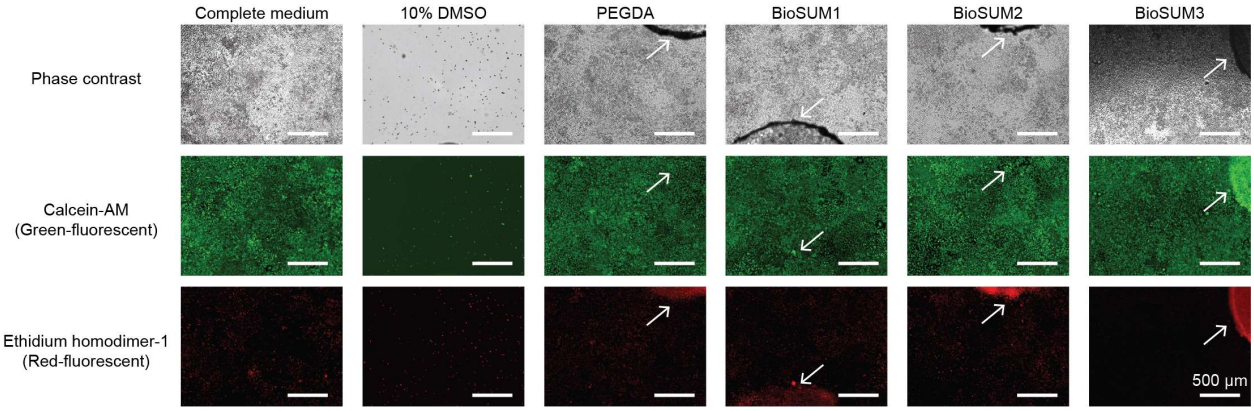

Fig. S52. Images of L929 live/dead cells after 7 days of culture. Arrows indicate the positions of devices.

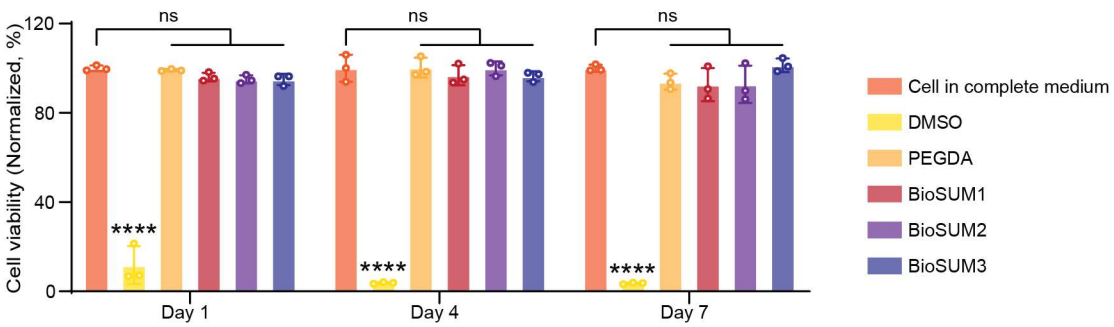

Fig. S53. In vitro cytocompatibility of BioSUMs using L929 cells (mouse fibroblast cell line) after 1 day, 4 days, and 7 days of culture. Cytotoxic concentration of DMSO served as a positive control, while PEGDA was used as a negative control. n = 3 individual samples. Two-way ANOVA, Holm-Sidak's multiple comparison with cell in complete medium. *p < 0.05, **p < 0.01, ***p < 0.001, ****p < 0.0001. ns represents not statistically significant.

Table S1. All diffusivity constants

	D_l	D_h	J_{mid}	J_{range}
BioSUM1	$2.65 \times 10^{-10}\ m^2/s$	$0.02D_l$	2	1.5
BioSUM2	$2.65 \times 10^{-10}\ m^2/s$	$0.02D_l$	2.5	2
BioSUM3	$1.93 \times 10^{-9}\ m^2/s$	$0.02D_l$	3	2

Table S2. Mechanical characteristics of pH-responsive BioSUM materials after fully swollen in PBS solution.

	Young's modulus (MPa)	**Elongation at break (%)**
BioSUM1	0.92±0.06	112±9
BioSUM2	0.11±0.01	66±7
BioSUM3	0.67±0.04	220±11

Table S3. Mechanical characteristics of pH-responsive BioSUM materials after fully swollen in simulated fluids.

	Young's modulus (MPa)	**Elongation at break (%)**
BioSUM1 after swollen in SGF	0.25±0.03	23±2
BioSUM2 after swollen in SIF	0.10±0.01	60±2
BioSUM3 after swollen in SPJ	0.36±0.03	156±8

Table S4. Mechanical characteristics of pH-responsive hydrogels with different DMAEMA and DPAEMA ratios after fully swollen in the PBS solution.

	Young's modulus (MPa)	**Elongation at break (%)**
6:4	2.06±0.09	147±7
7:3 (BioSUM1)	0.92±0.06	112±9
8:2	0.45±0.01	95±1
9:1 (BioSUM2)	0.11±0.01	66±7
10	0.040±0.001	35±8

Table S5. Mechanical characteristics of pH-responsive hydrogels with different AAc and PEGDA ratios after fully swollen in the PBS solution.

	Young's modulus (MPa)	**Elongation at break (%)**
2× AAc	1.04±0.02	144±11
0.5× AAc	0.31±0.02	260±8
1× AAc, 1× PEGDA (BioSUM3)	0.67±0.04	220±11
2× PEGDA	0.84±0.04	172±7
0.5× PEGDA	0.53±0.01	255±9

Movie S1. Demonstration of the injection of BioSUM through a plastic tube (I.D. = 3 mm, O.D. = 5 mm) onto a pork phantom. BioSUM has a thickness of 300 μm and diameter of 7 mm with circular disks of Zn (1 mm diameter and 25 μm thickness).

Movie S2. Placement of a BioSUM under laparoscopic view. The placement of a BioSUM onto the stomach in a porcine model involves a 5 mm laparoscopic grasper with 45 cm length. The video demonstrates the procedure both with and without the assistance from a plastic tube (I.D. = 9 mm, O.D. = 10 mm).

References and Notes

1. K. Kwon, J. U. Kim, S. M. Won, J. Zhao, R. Avila, H. Wang, K. S. Chun, H. Jang, K. H. Lee, J.-H. Kim, S. Yoo, Y. J. Kang, J. Kim, J. Lim, Y. Park, W. Lu, T. I. Kim, A. Banks, Y. Huang, J. A. Rogers, A battery-less wireless implant for the continuous monitoring of vascular pressure, flow rate and temperature. *Nat. Biomed. Eng.* **7**, 1215–1228 (2023). doi:10.1038/s41551-023-01022-4 Medline

2. C. M. Boutry, L. Beker, Y. Kaizawa, C. Vassos, H. Tran, A. C. Hinckley, R. Pfattner, S. Niu, J. Li, J. Claverie, Z. Wang, J. Chang, P. M. Fox, Z. Bao, Biodegradable and flexible arterial-pulse sensor for the wireless monitoring of blood flow. *Nat. Biomed. Eng.* **3**, 47–57 (2019). doi:10.1038/s41551-018-0336-5 Medline

3. M. Corsi, A. Paghi, S. Mariani, G. Golinelli, A. Debrassi, G. Egri, G. Leo, E. Vandini, A. Vilella, L. Dähne, D. Giuliani, G. Barillaro, Bioresorbable nanostructured chemical sensor for monitoring of pH level in vivo. *Adv. Sci.* **9**, e2202062 (2022). doi:10.1002/advs.202202062 Medline

4. L. Lipani, B. G. R. Dupont, F. Doungmene, F. Marken, R. M. Tyrrell, R. H. Guy, A. Ilie, Non-invasive, transdermal, path-selective and specific glucose monitoring via a graphene-based platform. *Nat. Nanotechnol.* **13**, 504–511 (2018). doi:10.1038/s41565-018-0112-4 Medline

5. Y. Chen, S. Lu, S. Zhang, Y. Li, Z. Qu, Y. Chen, B. Lu, X. Wang, X. Feng, Skin-like biosensor system via electrochemical channels for noninvasive blood glucose monitoring. *Sci. Adv.* **3**, e1701629 (2017). doi:10.1126/sciadv.1701629 Medline

6. H. Zhang, P. Gutruf, K. Meacham, M. C. Montana, X. Zhao, A. M. Chiarelli, A. Vázquez-Guardado, A. Norris, L. Lu, Q. Guo, C. Xu, Y. Wu, H. Zhao, X. Ning, W. Bai, I. Kandela, C. R. Haney, D. Chanda, R. W. Gereau 4th, J. A. Rogers, Wireless, battery-free optoelectronic systems as subdermal implants for local tissue oximetry. *Sci. Adv.* **5**, eaaw0873 (2019). doi:10.1126/sciadv.aaw0873 Medline

7. J. Shin, Z. Liu, W. Bai, Y. Liu, Y. Yan, Y. Xue, I. Kandela, M. Pezhouh, M. R. MacEwan, Y. Huang, W. Z. Ray, W. Zhou, J. A. Rogers, Bioresorbable optical sensor systems for monitoring of intracranial pressure and temperature. *Sci. Adv.* **5**, eaaw1899 (2019). doi:10.1126/sciadv.aaw1899 Medline

8. L. Lu, P. Gutruf, L. Xia, D. L. Bhatti, X. Wang, A. Vazquez-Guardado, X. Ning, X. Shen, T. Sang, R. Ma, G. Pakeltis, G. Sobczak, H. Zhang, D. O. Seo, M. Xue, L. Yin, D. Chanda, X. Sheng, M. R. Bruchas, J. A. Rogers, Wireless optoelectronic photometers for monitoring neuronal dynamics in the deep brain. *Proc. Natl. Acad. Sci. U.S.A.* **115**, E1374–E1383 (2018). doi:10.1073/pnas.1718721115 Medline

9. W. Bai, J. Shin, R. Fu, I. Kandela, D. Lu, X. Ni, Y. Park, Z. Liu, T. Hang, D. Wu, Y. Liu, C. R. Haney, I. Stepien, Q. Yang, J. Zhao, K. R. Nandoliya, H. Zhang, X. Sheng, L. Yin, K. MacRenaris, A. Brikha, F. Aird, M. Pezhouh, J. Hornick, W. Zhou, J. A. Rogers, Bioresorbable photonic devices for the spectroscopic characterization of physiological status and neural activity. *Nat. Biomed. Eng.* **3**, 644–654 (2019). doi:10.1038/s41551-019-0435-y Medline

10. J. Kim, G. A. Salvatore, H. Araki, A. M. Chiarelli, Z. Xie, A. Banks, X. Sheng, Y. Liu, J. W. Lee, K.-I. Jang, S. Y. Heo, K. Cho, H. Luo, B. Zimmerman, J. Kim, L. Yan, X. Feng, S. Xu, M. Fabiani, G. Gratton, Y. Huang, U. Paik, J. A. Rogers, Battery-free, stretchable optoelectronic systems for wireless optical characterization of the skin. *Sci. Adv.* **2**, e1600418 (2016). doi:10.1126/sciadv.1600418 Medline

11. K. Kwon, J. U. Kim, Y. Deng, S. R. Krishnan, J. Choi, H. Jang, K. Lee, C.-J. Su, I. Yoo, Y. Wu, L. Lipschultz, J.-H. Kim, T. S. Chung, D. Wu, Y. Park, T. Kim, R. Ghaffari, S. Lee, Y. Huang, J. A. Rogers, An on-skin platform for wireless monitoring of flow rate, cumulative loss and temperature of sweat in real time. *Nat. Electron.* **4**, 302–312 (2021). doi:10.1038/s41928-021-00556-2

12. R. C. Webb, Y. Ma, S. Krishnan, Y. Li, S. Yoon, X. Guo, X. Feng, Y. Shi, M. Seidel, N. H. Cho, J. Kurniawan, J. Ahad, N. Sheth, J. Kim, J. G. Taylor 6th, T. Darlington, K. Chang, W. Huang, J. Ayers, A. Gruebele, R. M. Pielak, M. J. Slepian, Y. Huang, A. M. Gorbach, J. A. Rogers, Epidermal devices for noninvasive, precise, and continuous mapping of macrovascular and microvascular blood flow. *Sci. Adv.* **1**, e1500701 (2015). doi:10.1126/sciadv.1500701 Medline

13. K. Kwon, H. Wang, J. Lim, K. S. Chun, H. Jang, I. Yoo, D. Wu, A. J. Chen, C. G. Gu, L. Lipschultz, J. U. Kim, J. Kim, H. Jeong, H. Luan, Y. Park, C.-J. Su, Y. Ishida, S. R. Madhvapathy, A. Ikoma, J. W. Kwak, D. S. Yang, A. Banks, S. Xu, Y. Huang, J.-K. Chang, J. A. Rogers, Wireless, soft electronics for rapid, multisensor measurements of hydration levels in healthy and diseased skin. *Proc. Natl. Acad. Sci. U.S.A.* **118**, e2020398118 (2021). doi:10.1073/pnas.2020398118 Medline

14. S.-W. Hwang, H. Tao, D.-H. Kim, H. Cheng, J.-K. Song, E. Rill, M. A. Brenckle, B. Panilaitis, S. M. Won, Y.-S. Kim, Y. M. Song, K. J. Yu, A. Ameen, R. Li, Y. Su, M. Yang, D. L. Kaplan, M. R. Zakin, M. J. Slepian, Y. Huang, F. G. Omenetto, J. A. Rogers, A physically transient form of silicon electronics. *Science* **337**, 1640–1644 (2012). doi:10.1126/science.1226325 Medline

15. Y. S. Oh, J.-H. Kim, Z. Xie, S. Cho, H. Han, S. W. Jeon, M. Park, M. Namkoong, R. Avila, Z. Song, S.-U. Lee, K. Ko, J. Lee, J.-S. Lee, W. G. Min, B.-J. Lee, M. Choi, H. U. Chung, J. Kim, M. Han, J. Koo, Y. S. Choi, S. S. Kwak, S. B. Kim, J. Kim, J. Choi, C.-M. Kang, J. U. Kim, K. Kwon, S. M. Won, J. M. Baek, Y. Lee, S. Y. Kim, W. Lu, A. Vazquez-Guardado, H. Jeong, H. Ryu, G. Lee, K. Kim, S. Kim, M. S. Kim, J. Choi, D. Y. Choi, Q. Yang, H. Zhao, W. Bai, H. Jang, Y. Yu, J. Lim, X. Guo, B. H. Kim, S. Jeon, C. Davies, A. Banks, H. J. Sung, Y. Huang, I. Park, J. A. Rogers, Battery-free, wireless soft sensors for continuous multi-site measurements of pressure and temperature from patients at risk for pressure injuries. *Nat. Commun.* **12**, 5008 (2021). doi:10.1038/s41467-021-25324-w Medline

16. D. R. Agrawal, Y. Tanabe, D. Weng, A. Ma, S. Hsu, S.-Y. Liao, Z. Zhen, Z.-Y. Zhu, C. Sun, Z. Dong, F. Yang, H. F. Tse, A. S. Y. Poon, J. S. Ho, Conformal phased surfaces for wireless powering of bioelectronic microdevices. *Nat. Biomed. Eng.* **1**, 0043 (2017). doi:10.1038/s41551-017-0043 Medline

17. V. B. Koman, N. A. Bakh, X. Jin, F. T. Nguyen, M. Son, D. Kozawa, M. A. Lee, G. Bisker, J. Dong, M. S. Strano, A wavelength-induced frequency filtering method for fluorescent

nanosensors in vivo. *Nat. Nanotechnol.* **17**, 643–652 (2022). doi:10.1038/s41565-022-01136-x Medline

18. S. Iwano, M. Sugiyama, H. Hama, A. Watakabe, N. Hasegawa, T. Kuchimaru, K. Z. Tanaka, M. Takahashi, Y. Ishida, J. Hata, S. Shimozono, K. Namiki, T. Fukano, M. Kiyama, H. Okano, S. Kizaka-Kondoh, T. J. McHugh, T. Yamamori, H. Hioki, S. Maki, A. Miyawaki, Single-cell bioluminescence imaging of deep tissue in freely moving animals. *Science* **359**, 935–939 (2018). doi:10.1126/science.aaq1067 Medline

19. S. Sonmezoglu, J. R. Fineman, E. Maltepe, M. M. Maharbiz, Monitoring deep-tissue oxygenation with a millimeter-scale ultrasonic implant. *Nat. Biotechnol.* **39**, 855–864 (2021). doi:10.1038/s41587-021-00866-y Medline

20. S. Sharma, K. B. Ramadi, N. H. Poole, S. S. Srinivasan, K. Ishida, J. Kuosmanen, J. Jenkins, F. Aghlmand, M. B. Swift, M. G. Shapiro, G. Traverso, A. Emami, Location-aware ingestible microdevices for wireless monitoring of gastrointestinal dynamics. *Nat. Electron.* **6**, 242–256 (2023). doi:10.1038/s41928-023-00916-0 Medline

21. A. Hai, V. C. Spanoudaki, B. B. Bartelle, A. Jasanoff, Wireless resonant circuits for the minimally invasive sensing of biophysical processes in magnetic resonance imaging. *Nat. Biomed. Eng.* **3**, 69–78 (2019). doi:10.1038/s41551-018-0309-8 Medline

22. V. Kalidasan, X. Yang, Z. Xiong, R. R. Li, H. Yao, H. Godaba, S. Obuobi, P. Singh, X. Guan, X. Tian, S. A. Kurt, Z. Li, D. Mukherjee, R. Rajarethinam, C. S. Chong, J.-W. Wang, P. L. R. Ee, W. Loke, B. C. K. Tee, J. Ouyang, C. J. Charles, J. S. Ho, Wirelessly operated bioelectronic sutures for the monitoring of deep surgical wounds. *Nat. Biomed. Eng.* **5**, 1217–1227 (2021). doi:10.1038/s41551-021-00802-0 Medline

23. C. Wang, B. Qi, M. Lin, Z. Zhang, M. Makihata, B. Liu, S. Zhou, Y. H. Huang, H. Hu, Y. Gu, Y. Chen, Y. Lei, T. Lee, S. Chien, K.-I. Jang, E. B. Kistler, S. Xu, Continuous monitoring of deep-tissue haemodynamics with stretchable ultrasonic phased arrays. *Nat. Biomed. Eng.* **5**, 749–758 (2021). doi:10.1038/s41551-021-00763-4 Medline

24. D. Maresca, A. Lakshmanan, M. Abedi, A. Bar-Zion, A. Farhadi, G. J. Lu, J. O. Szablowski, D. Wu, S. Yoo, M. G. Shapiro, Biomolecular ultrasound and sonogenetics. *Annu. Rev. Chem. Biomol. Eng.* **9**, 229–252 (2018). doi:10.1146/annurev-chembioeng-060817-084034 Medline

25. E. Macé, G. Montaldo, I. Cohen, M. Baulac, M. Fink, M. Tanter, Functional ultrasound imaging of the brain. *Nat. Methods* **8**, 662–664 (2011). doi:10.1038/nmeth.1641 Medline

26. A. Dizeux, M. Gesnik, H. Ahnine, K. Blaize, F. Arcizet, S. Picaud, J.-A. Sahel, T. Deffieux, P. Pouget, M. Tanter, Functional ultrasound imaging of the brain reveals propagation of task-related brain activity in behaving primates. *Nat. Commun.* **10**, 1400 (2019). doi:10.1038/s41467-019-09349-w Medline

27. R. W. Bourdeau, A. Lee-Gosselin, A. Lakshmanan, A. Farhadi, S. R. Kumar, S. P. Nety, M. G. Shapiro, Acoustic reporter genes for noninvasive imaging of microorganisms in mammalian hosts. *Nature* **553**, 86–90 (2018). doi:10.1038/nature25021 Medline

28. A. Farhadi, G. H. Ho, D. P. Sawyer, R. W. Bourdeau, M. G. Shapiro, Ultrasound imaging of gene expression in mammalian cells. *Science* **365**, 1469–1475 (2019). doi:10.1126/science.aax4804 Medline

29. E. Girard, M. Messager, A. Sauvanet, S. Benoist, G. Piessen, J.-Y. Mabrut, C. Mariette, Anastomotic leakage after gastrointestinal surgery: Diagnosis and management. *J. Visc. Surg.* **151**, 441–450 (2014). doi:10.1016/j.jviscsurg.2014.10.004 Medline

30. L. Yin, H. Cheng, S. Mao, R. Haasch, Y. Liu, X. Xie, S.-W. Hwang, H. Jain, S.-K. Kang, Y. Su, R. Li, Y. Huang, J. A. Rogers, Dissolvable metals for transient electronics. *Adv. Funct. Mater.* **24**, 645–658 (2014). doi:10.1002/adfm.201301847

31. A. Lendlein, A. M. Schmidt, R. Langer, AB-polymer networks based on oligo(ε-caprolactone) segments showing shape-memory properties. *Proc. Natl. Acad. Sci. U.S.A.* **98**, 842–847 (2001). Medline

32. S. S. Halacheva, D. J. Adlam, E. K. Hendow, T. J. Freemont, J. Hoyland, B. R. Saunders, Injectable biocompatible and biodegradable pH-responsive hollow particle gels containing poly(acrylic acid): The effect of copolymer composition on gel properties. *Biomacromolecules* **15**, 1814–1827 (2014). doi:10.1021/bm5002069 Medline

33. M. Changez, V. Koul, B. Krishna, A. K. Dinda, V. Choudhary, Studies on biodegradation and release of gentamicin sulphate from interpenetrating network hydrogels based on poly(acrylic acid) and gelatin: In vitro and in vivo. *Biomaterials* **25**, 139–146 (2004). doi:10.1016/S0142-9612(03)00466-6 Medline

34. M. J. Bruining, H. G. T. Blaauwgeers, R. Kuijer, E. Pels, R. M. M. A. Nuijts, L. H. Koole, Biodegradable three-dimensional networks of poly(dimethylamino ethyl methacrylate). Synthesis, characterization and in vitro studies of structural degradation and cytotoxicity. *Biomaterials* **21**, 595–604 (2000). doi:10.1016/S0142-9612(99)00223-9 Medline

35. N. Deirram, C. Zhang, S. S. Kermaniyan, A. P. R. Johnston, G. K. Such, pH-responsive polymer nanoparticles for drug delivery. *Macromol. Rapid Commun.* **40**, e1800917 (2019). doi:10.1002/marc.201800917 Medline

36. O. E. Philippova, D. Hourdet, R. Audebert, A. R. Khokhlov, pH-responsive gels of hydrophobically modified poly(acrylic acid). *Macromolecules* **30**, 8278–8285 (1997). doi:10.1021/ma970957v

37. H. Zhang, M. Dehghany, Y. Hu, Kinetics of polyelectrolyte gels. *J. Appl. Mech.* **87**, 061010 (2020). doi:10.1115/1.4046737

38. W. Hong, X. Zhao, J. Zhou, Z. Suo, A theory of coupled diffusion and large deformation in polymeric gels. *J. Mech. Phys. Solids* **56**, 1779–1793 (2008). doi:10.1016/j.jmps.2007.11.010

39. N. M. Tole, *Basic Physics of Ultrasonographic Imaging* (World Health Organization, 2005).

40. J. T. Ylitalo, H. Ermert, Ultrasound synthetic aperture imaging: Monostatic approach. *IEEE Trans. Ultrason. Ferroelectr. Freq. Control* **41**, 333–339 (1994). doi:10.1109/58.285467

41. E. L. McConnell, A. W. Basit, S. Murdan, Measurements of rat and mouse gastrointestinal pH, fluid and lymphoid tissue, and implications for in-vivo experiments. *J. Pharm. Pharmacol.* **60**, 63–70 (2008). doi:10.1211/jpp.60.1.0008 Medline

42. A. E. Hanbidge, D. Lynch, S. R. Wilson, US of the peritoneum. *Radiographics* **23**, 663–685 (2003). doi:10.1148/rg.233025712 Medline

43. D. Garcia, “Make the most of MUST, an open-source Matlab UltraSound Toolbox,” 2021 IEEE International Ultrasonics Symposium (IUS), Xi’an, China (2021), pp. 1–4.

44. D. Garcia, SIMUS: An open-source simulator for medical ultrasound imaging. Part I: Theory & examples. *Comput. Methods Programs Biomed.* **218**, 106726 (2022). doi:10.1016/j.cmpb.2022.106726 Medline

45. A. Cigier, F. Varray, D. Garcia, SIMUS: An open-source simulator for medical ultrasound imaging. Part II: Comparison with four simulators. *Comput. Methods Programs Biomed.* **220**, 106774 (2022). doi:10.1016/j.cmpb.2022.106774 Medline

46. V. B. Morris, S. Nimbalkar, M. Younesi, P. McClellan, O. Akkus, Mechanical properties, cytocompatibility and manufacturability of chitosan:PEGDA hybrid-gel scaffolds by stereolithography. *Ann. Biomed. Eng.* **45**, 286–296 (2017). doi:10.1007/s10439-016-1643-1 Medline

47. C. G. Williams, A. N. Malik, T. K. Kim, P. N. Manson, J. H. Elisseeff, Variable cytocompatibility of six cell lines with photoinitiators used for polymerizing hydrogels and cell encapsulation. *Biomaterials* **26**, 1211–1218 (2005). doi:10.1016/j.biomaterials.2004.04.024 Medline

48. N. M. Rahman, E. K. Mishra, H. E. Davies, R. J. O. Davies, Y. C. G. Lee, Clinically important factors influencing the diagnostic measurement of pleural fluid pH and glucose. *Am. J. Respir. Crit. Care Med.* **178**, 483–490 (2008). doi:10.1164/rccm.200801-062OC Medline

49. N. Gitlin, J. L. Stauffer, R. C. Silvestri, The pH of ascitic fluid in the diagnosis of spontaneous bacterial peritonitis in alcoholic cirrhosis. *Hepatology* **2**, 408–411 (1982). doi:10.1002/hep.1840020403 Medline

50. D. A. Hickman, C. L. Pawlowski, U. D. S. Sekhon, J. Marks, A. S. Gupta, Biomaterials and advanced technologies for hemostatic management of bleeding. *Adv. Mater.* **30**, 1700859 (2018). doi:10.1002/adma.201700859 Medline

51. N. Bhattarai, H. R. Ramay, J. Gunn, F. A. Matsen, M. Zhang, PEG-grafted chitosan as an injectable thermosensitive hydrogel for sustained protein release. *J. Control. Release* **103**, 609–624 (2005). doi:10.1016/j.jconrel.2004.12.019 Medline

52. Q. Yang, T. Wei, R. T. Yin, M. Wu, Y. Xu, J. Koo, Y. S. Choi, Z. Xie, S. W. Chen, I. Kandela, S. Yao, Y. Deng, R. Avila, T.-L. Liu, W. Bai, Y. Yang, M. Han, Q. Zhang, C. R. Haney, K. Benjamin Lee, K. Aras, T. Wang, M.-H. Seo, H. Luan, S. M. Lee, A. Brikha, N. Ghoreishi-Haack, L. Tran, I. Stepien, F. Aird, E. A. Waters, X. Yu, A. Banks, G. D. Trachiotis, J. M. Torkelson, Y. Huang, Y. Kozorovitskiy, I. R. Efimov, J. A. Rogers, Photocurable bioresorbable adhesives as functional interfaces between flexible bioelectronic devices and soft biological tissues. *Nat. Mater.* **20**, 1559–1570 (2021). doi:10.1038/s41563-021-01051-x Medline

53. J. Bruce, Z. H. Krukowski, G. Al-Khairy, E. M. Russell, K. G. M. Park, Systematic review of the definition and measurement of anastomotic leak after gastrointestinal surgery. *Br. J. Surg.* **88**, 1157–1168 (2001). doi:10.1046/j.0007-1323.2001.01829.x Medline

54. B. U. Su'a, H. L. Mikaere, J. L. Rahiri, I. B. Bissett, A. G. Hill, Systematic review of the role of biomarkers in diagnosing anastomotic leakage following colorectal surgery. *Br. J. Surg.* **104**, 503–512 (2017). doi:10.1002/bjs.10487 Medline

55. H. Zhang, X. Lin, S. Chin, M. W. Grinstaff, Synthesis and characterization of poly(glyceric acid carbonate): A degradable analogue of poly(acrylic acid). *J. Am. Chem. Soc.* **137**, 12660–12666 (2015). doi:10.1021/jacs.5b07911 Medline

56. B. Reid, M. Gibson, A. Singh, J. Taube, C. Furlong, M. Murcia, J. Elisseeff, PEG hydrogel degradation and the role of the surrounding tissue environment. *J. Tissue Eng. Regen. Med.* **9**, 315–318 (2015). doi:10.1002/term.1688 Medline

57. M. B. Browning, S. N. Cereceres, P. T. Luong, E. M. Cosgriff-Hernandez, Determination of the in vivo degradation mechanism of PEGDA hydrogels. *J. Biomed. Mater. Res. A* **102**, 4244–4251 (2014). Medline

58. Y. Zhang, M. Zheng, T. Kissel, S. Agarwal, Design and biophysical characterization of bioresponsive degradable poly(dimethylaminoethyl methacrylate) based polymers for in vitro DNA transfection. *Biomacromolecules* **13**, 313–322 (2012). doi:10.1021/bm2015174 Medline

59. V. San Miguel, A. J. Limer, D. M. Haddleton, F. Catalina, C. Peinado, Biodegradable and thermoresponsive micelles of triblock copolymers based on 2-(*N*,*N*-dimethylamino)ethyl methacrylate and ε-caprolactone for controlled drug delivery. *Eur. Polym. J.* **44**, 3853–3863 (2008). doi:10.1016/j.eurpolymj.2008.07.056

60. A. W. Jackson, S. R. Mothe, P. Ang, L. R. Chennamaneni, A. M. V. Herk, P. Thoniyot, Backbone degradable poly(acrylic acid) analogue via radical ring-opening copolymerization and enhanced biodegradability. *Chemosphere* **293**, 133487 (2022). doi:10.1016/j.chemosphere.2021.133487 Medline

61. D. Das, P. Ghosh, S. Dhara, A. B. Panda, S. Pal, Dextrin and poly(acrylic acid)-based biodegradable, non-cytotoxic, chemically cross-linked hydrogel for sustained release of ornidazole and ciprofloxacin. *ACS Appl. Mater. Interfaces* **7**, 4791–4803 (2015). doi:10.1021/am508712e Medline

62. I. Gaytán, M. Burelo, H. Loza-Tavera, Current status on the biodegradability of acrylic polymers: Microorganisms, enzymes and metabolic pathways involved. *Appl. Microbiol. Biotechnol.* **105**, 991–1006 (2021). doi:10.1007/s00253-020-11073-1 Medline

63. Z. S. Stillman, B. M. Jarai, N. Raman, P. Patel, C. A. Fromen, Degradation profiles of poly(ethylene glycol) diacrylate (PEGDA)-based hydrogel nanoparticles. *Polym. Chem.* **11**, 568–580 (2020). doi:10.1039/C9PY01206K Medline

64. J. L. Grace, J. X. Huang, S.-E. Cheah, N. P. Truong, M. A. Cooper, J. Li, T. P. Davis, J. F. Quinn, T. Velkov, M. R. Whittaker, Antibacterial low molecular weight cationic polymers: Dissecting the contribution of hydrophobicity, chain length and charge to activity. *RSC Adv.* **6**, 15469–15477 (2016). doi:10.1039/C5RA24361K Medline

65. J. Zhang, R. Xie, S.-B. Zhang, C.-J. Cheng, X.-J. Ju, L.-Y. Chu, Rapid pH/temperature-responsive cationic hydrogels with dual stimuli-sensitive grafted side chains. *Polymer* **50**, 2516–2525 (2009). doi:10.1016/j.polymer.2009.03.044

66. R. Yoshida, K. Uchida, Y. Kaneko, K. Sakai, A. Kikuchi, Y. Sakurai, T. Okano, Comb-type grafted hydrogels with rapid deswelling response to temperature changes. *Nature* **374**, 240–242 (1995). doi:10.1038/374240a0

67. M. Dehghany, H. Zhang, R. Naghdabadi, Y. Hu, A thermodynamically-consistent large deformation theory coupling photochemical reaction and electrochemistry for light-responsive gels. *J. Mech. Phys. Solids* **116**, 239–266 (2018). doi:10.1016/j.jmps.2018.03.018

68. M. Rubinstein, R. H. Colby, *Polymer Physics* (Oxford Univ. Press, 2003).

69. A. P. Safronov, L. V. Adamova, A. S. Blokhina, I. A. Kamalov, P. A. Shabadrov, Flory-Huggins parameters for weakly crosslinked hydrogels of poly(acrylic acid) and poly(methacrylic acid) with various degrees of ionization. *Polym. Sci. Ser. A* **57**, 33–42 (2015). doi:10.1134/S0965545X15010095

70. Y. Lai, Y. Hu, Probing the swelling-dependent mechanical and transport properties of polyacrylamide hydrogels through AFM-based dynamic nanoindentation. *Soft Matter* **14**, 2619–2627 (2018). doi:10.1039/C7SM02351K Medline

71. H. F. Helander, L. Fändriks, Surface area of the digestive tract – revisited. *Scand. J. Gastroenterol.* **49**, 681–689 (2014). doi:10.3109/00365521.2014.898326 Medline

72. V. Mahadevan, Anatomy of the stomach. *Surgery* **32**, 571–574 (2014). doi:10.1016/j.mpsur.2014.09.009

73. H. A. Messal, S. Alt, R. M. M. Ferreira, C. Gribben, V. M.-Y. Wang, C. G. Cotoi, G. Salbreux, A. Behrens, Tissue curvature and apicobasal mechanical tension imbalance instruct cancer morphogenesis. *Nature* **566**, 126–130 (2019). doi:10.1038/s41586-019-0891-2 Medline

74. R. K. Goyal, Y. Guo, H. Mashimo, Advances in the physiology of gastric emptying. *Neurogastroenterol. Motil.* **31**, e13546 (2019). doi:10.1111/nmo.13546 Medline

75. A. Geliebter, S. A. Hashim, Gastric capacity in normal, obese, and bulimic women. *Physiol. Behav.* **74**, 743–746 (2001). doi:10.1016/S0031-9384(01)00619-9 Medline

76. S. Delgado-Aros, F. Cremonini, J. E. Castillo, H. J. Chial, D. D. Burton, I. Ferber, M. Camilleri, Independent influences of body mass and gastric volumes on satiation in humans. *Gastroenterology* **126**, 432–440 (2004). doi:10.1053/j.gastro.2003.11.007 Medline